STUDY OF CARBON BASED ELECTRODES IN CAPACITIVE DEIONIZATION FOR DESALINATION

A Thesis

Presented in Partial Fulfilment of the Requirements for the

Degree of Master of Science

with a

Major in Mechanical Engineering

in the

College of Graduate Studies

University of Idaho

by

Austin Glen Doutre

Major Professor: Tao Xing, Ph.D.

Committee Members: I. Francis Cheng, Ph.D.; Herbert Hess, Ph.D.; David McIlroy, Ph.D.

Department Administrator: Steven Beyerlein, Ph.D.

August 2017

AUTHORIZATION TO SUBMIT

This thesis of AUSTIN DOUTRE, submitted for the degree of Master of Science with a major in Mechanical Engineering and titled “STUDY OF CARBON BASED ELECTRODES IN CAPACITIVE DEIONIZATION FOR DESALINATION," has been reviewed in final form. Permission, as indicated by the signatures and dates given below, is now granted to submit final copies to the College of Graduate Studies for approval.

Major Professor: _____ Date: _____

Tao Xing Ph.D.

Committee Members: _____ Date: _____

I. Francis Cheng Ph.D.

_____ Date: _____

Herbert Hess Ph.D.

_____ Date: _____

David McIlroy Ph.D.

Department Administrator: _____ Date: _____

Steven Beyerlein Ph.D.

ABSTRACT

The world's increasing concern for fresh water availability drives research in desalination. Capacitive deionization (CDI) is a method of water desalination where a voltage is applied to carbon electrodes resulting in salt ion adsorption. The desalination performance of three different carbon based electrodes, utilizing graphite felt, silica nanosprings, and a conductive thin film GUITAR are studied. Surface area of the bare graphite felt is improved from 0.8 m^2/g to 2.6 m^2/g when coated with GUITAR, and estimated near 22 m^2/g when incorporating silica nanosprings. A modified Hummers' method is used to enhance capacitance of GUITAR by over 15 times. Leakage current is eliminated from CDI cell charging step by operating at reduced voltages. Maximum salt adsorption is achieved using bare graphite felt, suggesting the non-porous nature of GUITAR. Also presented is a new CDI cell design and mathematical model of ion motion in electric and magnetic fields.

ACKNOWLEDGEMENTS

I'd like to acknowledge Professors Tao Xing, Frank Cheng, Dave McIlroy, and Herb Hess for their continued mentorship and patience with experimental discovery throughout this project. They shaped my experience in scientific experimentation, data validation, and offered valuable expertise in Mechanical Engineering, Electrochemistry, Physics, and Electrical Engineering.

I acknowledge the ongoing work of Haoyu Zhu, Jeremy Foutch, Humayun Kabir, Charles Nwamba, and Kailash Hamal with GUITAR in Frank's Chemistry lab. Their influence as responsible scientists, enthusiasm for new discovery, and expertise in all things GUITAR were vital in forming my experience as a graduate student. They were patient with my questions and took time to teach experimental procedures and what to look for in the data.

I would also like to acknowledge the work of the University of Idaho Engineering Capstone Design team, Saline Solution, consisting of Jessica Drouin, Essa Essa, Cody Moldenhauer, Ryan Ready, and Kevin Woodruff. They contributed much time and effort in developing the experimental channel setup and performing supportive desalination tests.

Funding for this research was provided in part by Vorsana Inc. during the 1st year of my graduate studies. Their initial concept designs provided the impetus for desalination research in the Mechanical Engineering department, and provided motivation for my research.

Additional support was provided by the Mechanical Engineering Department and Dr. Michael Maughan through a teaching assistantship, as well as the University of Idaho Industrial Assessment Center. Both provided exciting learning opportunities from mentoring student design projects to conducting industrial energy audits. These activities contributed to my appreciation of prototyping and a broadened perspective of engineering in industry.

DEDICATION

I dedicate this work to my dear wife Julia, who shares a love of learning and is patient through long days in the lab. And to my parents, who always encourage me to put forth my best in all I do.

TABLE OF CONTENTS

AUTHORIZATION TO SUBMIT ii
ABSTRACT iii
ACKNOWLEDGEMENTS iv
DEDICATION v
TABLE OF CONTENTS vi
LIST OF TABLES viii
LIST OF FIGURES ix
NOMENCLATURE xiii
CHAPTER 1 - LITERATURE REVIEW 1
1.1 Introduction 1
1.2 Objective and Approach 12
CHAPTER 2 - SMALL SCALE DESALINATION TESTING 14
2.1 Introduction 14
2.2 Methods 16
2.3 Results and Discussion 23
2.4 Conclusions 41
CHAPTER 3 - DYNAMIC FLOW CELL DESIGN 42
3.1 Introduction 42
3.2 Cell Design 44
CHAPTER 4 - ION MOTION MATHEMATICAL MODEL IN ELECTRIC AND MAGNETIC FIELDS 46
4.1 Introduction 46
4.2 Electric Field Only (Vacuum) 47
4.3 Magnetic Field Only (Vacuum) 49
4.4 Orthogonal Electric and Magnetic Fields (Vacuum) 53

4.5 Electric Field Only (Salt Water) 57
4.6 Magnetic Field Only (Salt Water) 61
4.7 Orthogonal Electric and Magnetic Fields (Salt Water) 65
4.8 Conclusions 69
CHAPTER 5 – CONCLUSIONS AND FUTURE WORK 70
5.1 Small Scale Desalination Testing 70
5.2 Dynamic Flow Cell Design 71
5.3 Theoretical Modeling 71
REFERENCES 72
APPENDIX – SENIOR DESIGN PROJECT 77
Introduction 77
Methods 77
Channel Desalination Results 79
Conductivity Meter Flow Verification 79
Conclusions 80

LIST OF TABLES

Table 1.1 Results from various experiments with brackish water (≈300-1,000 mg/L NaCl) and 1.2V using batch mode desalination. 6

Table 2.1 Comparison of mSAC and charge efficiency values for optimized voltage tests. 39

Table 2.2 Comparison of charge efficiency and mSAC values for 1.1V tests. 39

Table 4.1 Parametric study of scenarios 4.2.1 and 4.2.2; electric field only in a vacuum. 49

Table 4.2 Parametric study of scenarios 4.3.2; magnetic field only in a vacuum. 52

Table 4.3 Parametric study of scenarios 4.4.1 and 4.4.2; mixed orthogonal magnetic and electric fields in a vacuum. 57

Table 4.4 Parametric study of scenarios 4.5.1 and 4.5.2; electric field only in salt water. 60

Table 4.5 Parametric study of scenarios 4.6.2; magnetic field only in salt water. 64

Table 4.6 Required magnetic field strength values for the given angles of deflection. 65

Table 4.7 Parametric study of scenarios 4.7.1 and 4.7.2; mixed orthogonal magnetic and electric fields in salt water. 68

Table 4.8 Summary of projected ion velocities at the wall in a vacuum. 69

Table 4.9 Summary of projected ion velocities at the wall in salt water. 69

Table A.1 Effluent salt reduction from square channel, maximum of near 5% decrease. 79

Table A.2 Effluent salt reduction from High Aspect Ratio Channel (HARC), maximum of near 14% decrease. 79

LIST OF FIGURES

Figure 1.1 Schematic of Flow-by CDI: a) charge step, applied voltage invites Na and Cl ion adsorption to the electrodes, creating deionized effluent. b) discharge step, CDI cell is grounded and ions are released in a highly concentrated waste stream. 3

Figure 1.2 Example of typical current profile during the adsorption and desorption steps with zero potential desorption. 3

Figure 1.3 Image reproduced from [7] "Schematic of two designs for CDI experiments" by S. Porada et. al. and is licensed under CC BY-NC-ND 4.0. a) Single-pass experiment (SP-method): Water conductivity is measured at the exit of the cell, and the outflow is discarded afterwards. b) Batch-mode experiment (BM-method): Conductivity is measured in a (small) recycle beaker. 4

Figure 1.4 Conductivity of graphene with and without modified Hummers' method applied, showing increase of conductivity and surface wetting, reproduced from [33] with permission. ... 7

Figure 1.5 Image reproduced from [34] "Selected data for charge efficiency Λ and current efficiency λ as function the salt concentration (A)" by M. E. Suss et. al. and is licensed under CC BY 3.0. Data for charge efficiency are obtained for solid film electrodes at V_{ch} = 1.2 V in a cycle where V_{disch} = 0 V. Solid line denotes calculation results based on the improved mD model. 9

Figure 1.6 Image reproduced from [7] "Energy consumption of water desalination by MCDI and reverse osmosis (RO)" by S. Porada et. al. and is licensed under CC BY-NC-ND 4.0. 9

Figure 1.7 Depiction of Gouy-Chapman-Stern model for non-overlapping electrical double layers, A, and the Modified Donnan model for overlapping electrical double layers, B. Reproduced with permission from [49]. 11

Figure 1.8 SEM images of silica nanosprings, courtesy University of Idaho Physics department, a) grown on SGL graphite felt and b) nanosprings coated with GUITAR. 12

Figure 1.9 Experimental flow chart for Desalination research. 13

Figure 2.1 a) Graphite foil used for electrodes in capstone design prototypes. b) Exfoliated GUITAR-coated graphite foil electrodes after applying modified Hummers' method. 15

Figure 2.2 Anodic limit tests with CV results sweeping between 0V-2.2V in 1M H_2SO_4 for a) graphite foil and b) bare graphite felt (KFD 2.5). Intercalation peak with graphite foil. 15

Figure 2.3 Electrodes used in experiments: a) SGL bare graphite felt, b) GUITAR-coated SGL graphite felt, and c) GUITAR-coated SGL graphite felt with nanosprings. 16
Figure 2.4 Left: 3 electrode CV test cell with a) carbon basket counter electrode, b) working electrode, and c) Ag/AgCl reference electrode. Right: example CV results, where ΔI is the total difference between current at 350 mV. 17
Figure 2.5 Graphite felt samples in quartz boat after GUITAR coating. 18
Figure 2.6 Average graphite felt mass loss percent from the 20 minutes of high heat exposure before GUITAR coating, as a function of position along the quartz carrier boat. 18
Figure 2.7 Schematic of electrode preparation stages: a) graphite felt electrode is cut to size, b) coated with GUITAR, then either e) treated with modified Hummers' method, or c) prepared for nanospring growth, d) entire substrate coated with GUITAR, and then e). 19
Figure 2.8 Small scale CDI test setup: a) applied potential via Arbin Battery Tester, b) Pt wire current collectors, c) graphite felt electrodes, d) 25 μm separator, and e) stirred NaCl solution. . 20
Figure 2.9 Example of Cl ISE calibration points averaged from three different sets, taken before and after sample measurement. 22
Figure 2.10 Capacitance from single electrode CV for various thicknesses of GUITAR, represented by 20, 60 and 120 minutes of coating, and applied treatment times of 5, 20, 60, 120, and 180 minutes (conc. H_2SO_4 + 0.7M $NaNO_3$ + 1.28M H_2O_2). 24
Figure 2.11 Capacitance from single electrode CV in 5mM NaCl, 50mV/sec sweep rate between 0.2-0.5V for GUITAR Felt with 0, 20, 60, and 120 minutes of coating, using different wetting mechanisms; isopropanol alcohol, Plasma Prep, and modified Hummers' method at 20 minutes. 25
Figure 2.12 Initial salt adsorption results of GUITAR Felt with 0, 20, 60, and 120 minutes coating and GUITAR-NS Felt all with 20 minutes modified Hummers' method applied (except *Bare Felt). Adsorption based on conductivity change from initial sample to sample after 9 minutes of charging at 1.2V in 5mM NaCl. 26
Figure 2.13 Study of leakage current from Bare Felt as a function of applied voltage, ranging from 0.6V-1.2V, a-g respectively. Discharge current is fitted with 1) an exponential and 2) a double exponential. 28

Figure 2.14 Study of leakage current from GUITAR Felt as a function of applied voltage, ranging from 0.6V-1.2V, a-g respectively. Discharge current is fitted with 1) an exponential and 2) a double exponential. 29

Figure 2.15 Study of leakage current from GUITAR-NS Felt as a function of applied voltage, ranging from 0.6V-1.2V, a-g respectively. Discharge current is fitted with 1) an exponential and 2) a double exponential. 30

Figure 2.16 Ratios of charge current to discharge current values after 60 seconds at voltages between 0.6-1.2V. Values above 0.8 were determined as acceptable for symmetry of charge and discharge profiles. 31

Figure 2.17 Evaporated remains after CDI tests for a) GUITAR Felt and b) GUITAR-NS Felt. White and black backdrops reveal the presence of both salt and carbon particles. 32

Figure 2.18 CDI Current profiles from third cycle at optimized voltages in 20 mM NaCl. 34

Figure 2.19 Normalized CDI salt adsorption detected at optimized voltages using Cl ISE. Charge step occurs between 210-230 minutes, and discharge step between 230-250 minutes. 34

Figure 2.20 CDI Current profiles from third cycle at 1.1V in 20 mM NaCl. 35

Figure 2.21 Normalized CDI salt adsorption detected at 1.1V using Cl ISE. Charge step occurs between 210-230 minutes, and discharge step between 230-250 minutes. 35

Figure 2.22 Comparison of Cl ISE results at 0.7V applied and no applied voltage over the same length of time. 36

Figure 2.23 CDI Current profiles from third cycle at optimized voltages in 20 mM NaCl. 37

Figure 2.24 CDI salt adsorption detected at optimized voltages using conductivity. Charge step occurs between 200-220 minutes, and discharge step between 220-240 minutes. 37

Figure 2.25 CDI Current profiles from third cycle at 1.1V in 20 mM NaCl. 38

Figure 2.26 CDI Salt adsorption detected at 1.1V using conductivity. Charge step occurs between 200-220 minutes, and discharge step between 220-240 minutes. 38

Figure 2.27 CDI Current profiles from third cycle at 1.1V in 20 mM NaCl. 40

Figure 2.28 CDI Salt adsorption detected at 1.1V using conductivity, including 6x2 cm^2 Bare Felt. Charge step occurs between 200-220 minutes, and discharge step between 220-240 minutes. 40

Figure 3.1 Schematic of dynamic flow system for CDI testing. 42

Figure 3.2 Two configurations for conductivity measurement: a) conductivity probe in direct vicinity of active cell, and b) conductivity probe in a remote location connected by a tube with NaCl solution. 43

Figure 3.3 Conductivity probe readings for direct and remote probe placement in NaCl solution. Voltage is applied to the CDI cell only between 60-150 seconds..... 43

Figure 3.4 3D model of flow cell housing design: a) and b) slots for graphite current collectors, c) and d) slots for test electrodes, and e) slot for rubber O-ring. Arrows indicate flow direction. ... 45

Figure 3.5 a) 3D printed prototype of flow cell housing with graphite current collector and rubber O-ring. b) Flow cell housing machined in the University of Idaho machine shop..... 45

Figure 4.1 Reference coordinate system relating to electric and magnetic field analysis. 46

Figure 4.2 Representation of parabolic trajectory as x increases. 48

Figure 4.3 Schematic representation of ion trajectory due to electric field only (expanded y axis for better resolution). 49

Figure 4.4 Schematic of ion trajectory due to magnetic field normal to the page..... 51

Figure 4.5 Schematic of forces acting on ions from orthogonal electric and magnetic fields..... 53

Figure A.1 Two tanks used for Desalintaion experiment: Left, 0.5M NaCl solution reservoir, and Right, Deionized Water reservoir for rinsing..... 78

Figure A.2 Flow control valve setup and experimental channel. Ball valves used at outlet to control the flow rate. 78

Figure A.3 Cross sections of capstone channel prototypes: a) 1"x1" PVC tubing used for the square channel and b) 1/4"x4" channel used for High Aspect Ratio Channel (HARC). 78

Figure A.4 Comparison plot of continuous conductivity readings and simultaneous sample extraction. 80

NOMENCLATURE

ASAR – Average Salt Adsorption Rate

A – Electrode area

a – Acceleration (m/s^2)

Bare Felt – Un-modified SGL KFD graphite felt

$\boldsymbol{B}$ – Uniform magnetic field (T)

C – Capacitance

CDI – Capacitive Deionization

Cl – Chloride

CV – Cyclic Voltammetry

d – Distance between electrodes

ε – Permittivity of dielectric material

$\boldsymbol{E}$ – Uniform electric field (V/m)

E – Voltage potential

E_0 – Voltage intercept

EDL – Electric Double Layer

F – Faraday's constant (96,485 C/mole)

GCS – Gouy-Chapman-Stern model

GUITAR – Graphite from University of Idaho Thermalized Asphalt Reaction

GUITAR Felt – GUITAR-coated graphite felt

GUITAR-NS Felt – GUITAR-coated nanosprings on GUITAR-coated graphite felt

HARC – High Aspect Ratio Channel

H_0 – Channel Height (m)

I – Current (A)

ISAB – Ion Strength Adjustment Buffer

ISE – Ion Selective Electrode

L_0 – Channel Length (m)

L_R – Wall reattachment length (m)

Λ – Charge efficiency

λ – Current efficiency

m – Ion mass (kg)

mD – Modified Donnan model

mSAC – maximum Salt Adsorption Capacity (mg/g)

Na – Sodium

n – Number of moles transferred

$Q_{Electrode}$ – Electrode charge (moles)

q – Ion charge (C)

RO – Reverse Osmosis

r_0 – Ion radius (m)

t – Time (s)

TDS – Total Dissolved Solids

t_R – Time to Reattachment (s)

u, v, w – Velocity components in the x, y, and z directions

u_0 – Initial velocity, x direction (m/s)

vol – Volume of extracted sample

W_0 – Channel Width (m)

x, y, z – Principle coordinate system

CHAPTER 1 - LITERATURE REVIEW

1.1 Introduction

This chapter presents an introductory summary of various aspects of Capacitive Deionization for desalination. Discussion on the effectiveness of various carbon-based electrodes materials is presented along with methods used to enhance electrode capacity, theoretical models to predict ion adsorption, and the motivation and approach of the present study.

1.1.1 Background

A study of Desalination at the University of Idaho began in the middle of 2014 amidst the astounding California drought in the United States [1]. Although the drought is over in California, fresh water shortage continues to be a growing concern in the world as both human population and industrial processes require more and more water. Fresh drinking water is considered acceptable when it contains less than 600 mg/L of total dissolved solids (TDS) and unacceptable when above 1000 mg/L TDS [2]. Seawater contains on average 35,000 mg/L TDS in salts, and brackish water is between 500-30,000 mg/L TDS in salts. The Earth is covered by about 70% water, however less than 3% of that water is considered fresh, and only about 1% of that is surface water and easily accessible [3]. It is therefore pertinent to establish reliable means of desalinating sea and brackish water to combat the ever-increasing demand of fresh water.

Creating drinkable water requires energy, which takes many forms, to separate the water from the salt and other contaminants. Thermal energy is used in processes like distillation which evaporate and collect the purified condensate water, leaving the salts and solids behind [4]. This process generally requires a large area as the sun is an economical source of thermal energy. Mechanical energy is used in a process called Reverse Osmosis, or RO, to create a high-pressure difference to drive water through a semi-permeable membrane, trapping the salt. Because the high pressure is required regardless of the salt content, this method is particularly effective in applications of high salt concentration [4]. Another means of desalination with increased attention in recent decades is Capacitive Deionization, or CDI. It involves applying a voltage potential across a pair of electrodes, like a capacitor, to separate the salt ions by electrosorption, represented in Figure 1.1. As energy is only invested to attract the salt ions and not the water, this method provides more

efficient operation in lower concentrations such as brackish water [5, 6] and is the chosen desalination method for this study.

1.1.2 What is CDI?

The most basic configuration for capacitive deionization is called flow-by CDI and is represented schematically in Figure 1.1. It involves two porous electrodes placed opposite each other with an electrolyte passing between them. Ion adsorption occurs when a voltage potential is applied across the electrodes, causing a buildup of positive charge on the cathode and negative charge on the anode. Typical operating voltages for CDI processes are near 1.2V as electrolysis and the breakdown of water occurs at 1.23V. Consequently this induced electric field supplies attractive forces on the positive Na and negative Cl ions toward the anode and cathode respectively, resulting in a deionized effluent. Just as a capacitor reaches a point of maximum charge accumulation, CDI electrodes continually adsorb ions until they are fully saturated. Measuring the electric current during this process provides an indicator of this saturation point, as represented in Figure 1.2.

The desorption step occurs as the cell is grounded to 0V or a low negative voltage is applied causing ions to be released or driven back into the main stream of water. This results in a highly-concentrated waste stream that is collected and disposed of. In this way the electrode is regenerated and the desalination cycle is repeated continually for the lifespan of the electrodes.

When performing CDI tests to evaluate electrode adsorption capacity, there are two different experimental methods, single pass and batch mode [7]. In a single pass configuration, the influent salt water comes from a reservoir of a set concentration, and passes through the cell once and is then discarded. Salt adsorption in this case is determined by measuring conductivity and integrating the area under the curve from the beginning of a charge step to the point when the conductivity returns to the influent concentration, represented in Figure 1.3a. In a batch mode configuration the solution is recycled, allowing the salt concentration to reach a minimum or equilibrium point. Salt adsorption is calculated by the difference between the start and equilibrium salt concentration from the charge step. The batch mode configuration is used for studies in this thesis.

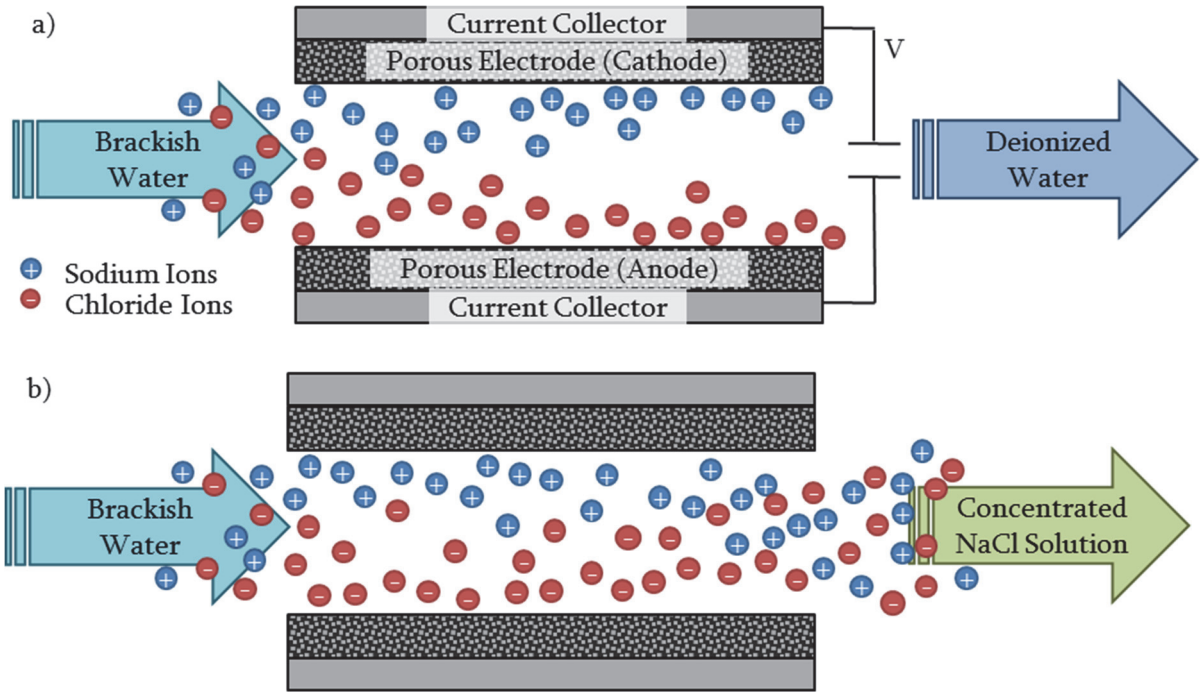

Figure 1.1 Schematic of Flow-by CDI: a) charge step, applied voltage invites Na and Cl ion adsorption to the electrodes, creating deionized effluent. b) discharge step, CDI cell is grounded and ions are released in a highly concentrated waste stream.

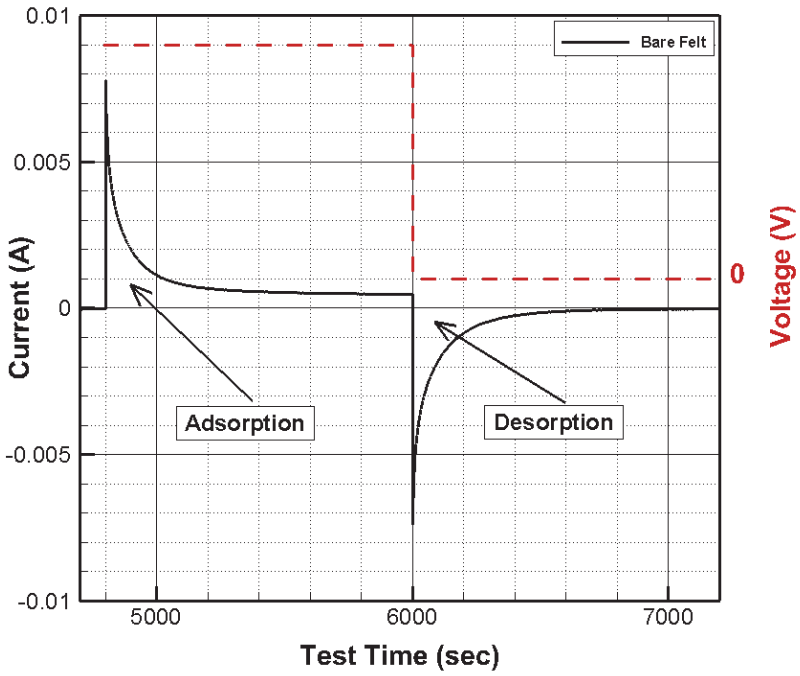

Figure 1.2 Example of typical current profile during the adsorption and desorption steps with zero potential desorption.

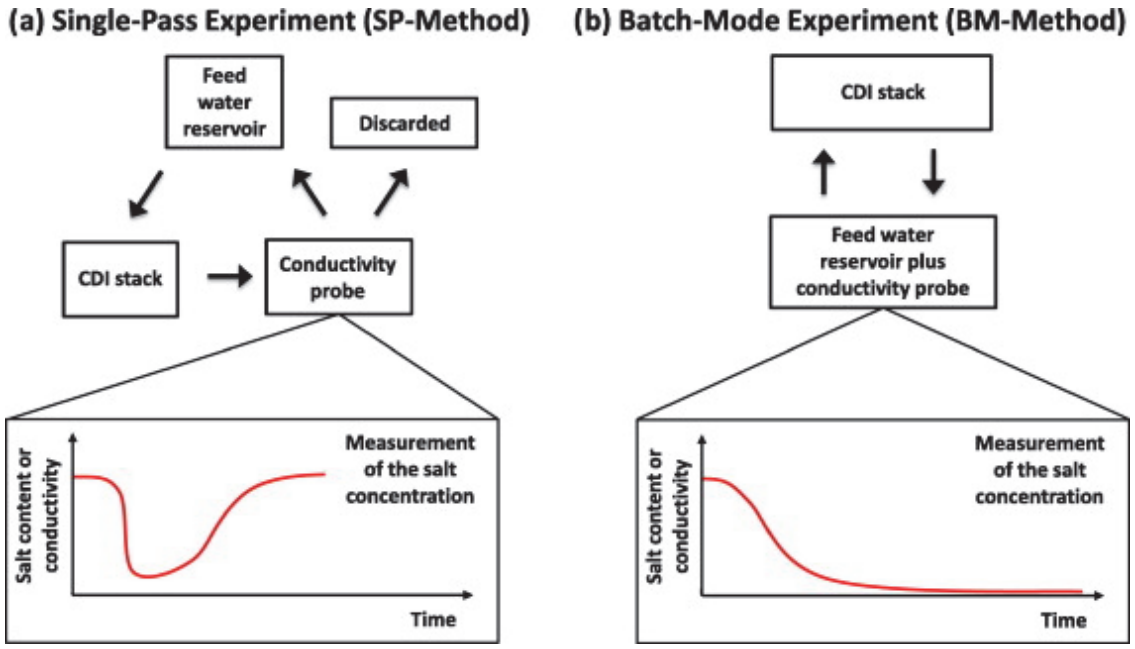

Figure 1.3 Image reproduced from [7] "Schematic of two designs for CDI experiments" by S. Porada et. al. and is licensed under CC BY-NC-ND 4.0. a) Single-pass experiment (SP-method): Water conductivity is measured at the exit of the cell, and the outflow is discarded afterwards. b) Batch-mode experiment (BM-method): Conductivity is measured in a (small) recycle beaker.

The study of flow-by CDI cells dates back to the 1960s [8]. Since then, research studies continue to modify electrode materials and configurations to improve performance. Modifications to the electrolyte flow direction has been studied with flow-through CDI [9], where the flow direction is perpendicular passing through the electrode, allowing for faster ion transfer kinetics. Membrane CDI (MCDI) [10] is another adaptation which incorporates an ion selective membrane to prevent the salt ions from drifting back into the main stream. Flow electrode CDI [11, 12], is a novel approach which replaces the static carbon electrode with a slurry of conductive particles, allowing for a pseudo-continuous operation of CDI. For its simplicity, flow-by CDI is used in the current study.

As this process involves the charging and discharging of an energy storage device, or capacitor, the governing equation is

$$C = \frac{\varepsilon \times A}{d} \tag{1.1}$$

Where ε is the permittivity of the dielectric medium, A is the area of the capacitor, and d is the distance between electrodes. Therefore, the capacitance of a given electrode is directly proportional to the surface area, and indirectly proportional to the distance between the electrodes. These factors retain their importance in CDI and Yoram Oren [13] suggests more specific considerations for CDI electrode material qualities. These are namely: 1) high specific surface area, 2) high electric conductivity, 3) fast response to adsorption and desorption, 4) chemical and electrochemical stability with different pH values, 5) the electrode can be easily shaped for different configurations, and 6) has low propensity for scaling and fouling. The first three points are primarily considered in this study.

1.1.3 Electrode Materials

Common materials from previous studies with flow-by CDI consist of activated carbon, carbon aerogel, graphene, carbon nanotubes, and other carbon-based electrodes as represented in [7, 14-16]. These materials exhibit qualities mentioned above of high specific area and are highly conductive. To date, typically reported salt adsorption ranges between 1 to 15 mg NaCl per gram electrode, see Table 1.1.

The surface area of these materials is typically quantified using BET measurements, where the amount of nitrogen molecules adsorbed to the surface can be measured and equated to the specific surface area of the electrode. It should be noted that nitrogen molecules have a smaller radius than Na or Cl ions, therefore this value may represent areas not entirely accessible to salt ions. Activated carbon typically has a reported specific surface area around 1000-1500 m^2/g [17, 18], carbon aerogel is typically near 1000 m^2/g [19, 20], and graphene ranges from 200-2000 m^2/g [15, 21].

High material surface area is directly related to the number and size of pores in the material. Standard pore sizes are set forth by IUPAC [22] identifying pores with diameters greater than 50 nm as macropores, diameters between 2 and 50 nm as mesopores, and diameters less than 2 nm as micropores. The relationship between surface area and capacitance has been studied to suggest that desalination occurs mainly within the micropores [7, 14-16].

Table 1.1 Results from various experiments with brackish water (≈300-1,000 mg/L NaCl) and 1.2V using batch mode desalination.

Substrate	Applied Potential (V)	Concentration (mg/L NaCl)	mSAC (mg/g)	Ref.
Activated Carbon	1.2	500	1.2	[23]
Activated Carbon	1.2	350	5.29	[18]
Activated Carbon	1.2	500	9.73	[15]
Activated Carbon	1.2	292	10.9	[24]
Carbon Aerogel	1.3	500	2.5	[25]
Carbon Aerogel	1.2	500	2.9	[26]
Carbon Nanotubes	1.2	500	2.57	[27]
Bare Graphite Felt	**1.1**	**1168**	**1.98**	**This work**
GUITAR Felt	**1.1**	**1168**	**0.56**	**This work**
GUITAR-NS Felt	**1.1**	**1168**	**0.05**	**This work**
Hollow Carbon Nanofibers	1.2	42	1.91	[28]
Electrospun Carbon Nanofibers	1.2	300	12.56	[29]
Mesoporous Carbon	1.2	1000	3.5	[30]
Kuraray YP50-F AC	1.2	290	9.1	[14]
Mast Carbon (S-TE11 AC)	1.2	290	8.5	[14]
MSP-20 AC	1.2	290	14.3	[14]
Norit DLC super50 (AC)	1.2	290	7.7	[14]
RG-TiO2	1.2	500	15.1	[31]
TiC-CDC	1.2	290	10.1	[14]

One method for increasing the capacitance of graphene, as it typically has a lower specific surface area, is to apply a modified Hummers' method. Hummers' method involves introducing graphite or graphene to a combination of sodium nitrate, sulfuric acid, and an oxidizing agent [23, 32]. The resulting graphite oxide is advantageous for capacitance and effectively salt adsorption through increasing conductivity, introduces wrinkles and expanded defects, and increases the electrode wettability [33] as shown in Figure 1.4.

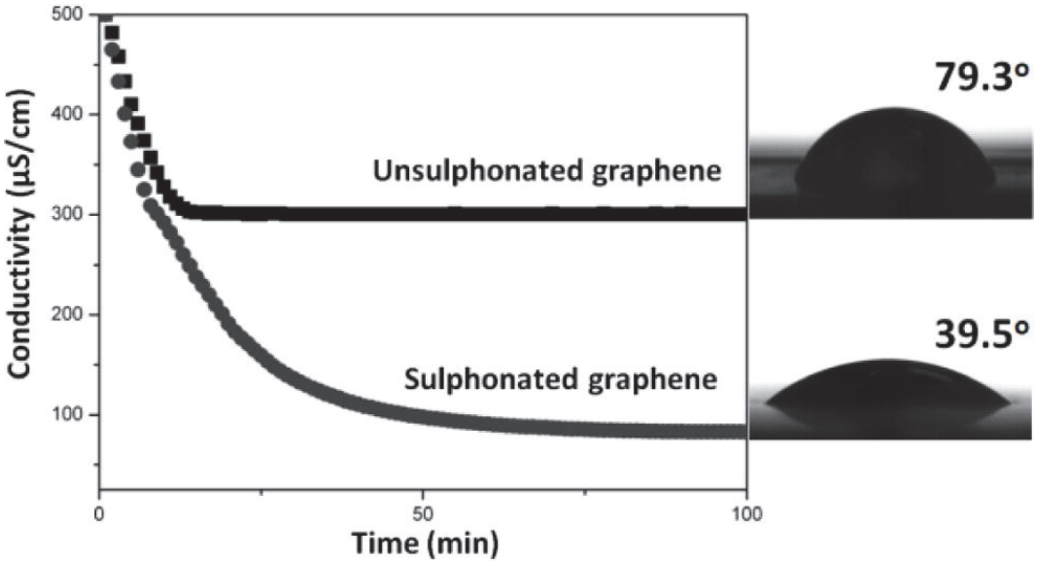

Figure 1.4 Conductivity of graphene with and without modified Hummers' method applied, showing increase of conductivity and surface wetting, reproduced from [33] with permission.

1.1.4 Desalination Performance Parameters

In an extensive review article, Suss et. al [34] describes four reliable parameters used to evaluate the performance of a given electrode in desalination applications. The first and most indicative parameter describing the CDI cell performance is the maximum Salt Adsorption Capacity, mSAC. This is determined by measuring the salt adsorption, typically using batch mode configuration, and dividing it by the total electrode mass.

$$mSAC = \frac{\text{NaCl removed (mg)}}{\text{mass}_{\text{Electrode}}\text{(g)}} \tag{1.2}$$

Salt concentration is typically measured using a conductivity probe inserted in-line with the CDI cell. The relationship between water conductivity and salt concentration is linear by a factor of 0.5 [35]. The electrode mass typically includes the mass of the entire electrode which includes binders and other components that may or may not contribute to the desalination process.

The second key parameter is the Charge Efficiency, Λ, which compares the amount of salt adsorbed to the amount of charge accumulated on the electrode [24]. In an idealized case, the amount of charge accumulated would equate to the amount of salt adsorbed. This is not the case however, discussed later, so both mSAC and accumulated charge are needed for this parameter.

$$\Lambda = \frac{F \times mSAC}{Q_{Electrode}} \tag{1.3}$$

Where F is Faraday's constant 96,485 C/mole and accumulated charge, $Q_{Electrode}$, can be determined by integrating the recorded current with respect to time. If there is a leakage current, the charge should be calculated using either the discharge current profile or by subtracting the leakage current from the charge current profile. This parameter allows a straightforward comparison of the energy required by the system.

The third parameter is the Average Salt Adsorption Rate (ASAR) which relates the salt adsorption as a function of the cycle charge time.

$$ASAR = \frac{\text{NaCl removed (mg)}}{\text{mass}_{\text{Electrode}}(\text{g}) \times \text{charge time}} \tag{1.4}$$

And the fourth parameter is the Current Efficiency, λ, which is relates the salt adsorption rate to the current [34]. This is provides a similar analysis, but for CDI operations where constant current applied instead of a constant voltage.

$$\lambda = \frac{F \times ASAR}{I} \tag{1.5}$$

Charge efficiency values for various carbon-based electrode systems has been summarized in Figure 1.5, showing a trend of increased efficiency as the salt concentration decreases. This is likely attributed to the increasing number of ions initially positioned near the electrode surface of the same charge, which detract from the actual adsorption. For traditional CDI, maximum efficiencies are near 80% at salt concentrations of about 30 mM and below. MCDI approaches near unity within the same approximate concentration range, due to the ion selective membranes.

Considering the thermodynamics of the salt removal process, the minimum amount of energy required for desalination of seawater (500 mM NaCl) is estimated at 1kWh/m^3 of freshwater produced [5, 7, 36]. Comparative studies of energy consumption between CDI processes and RO show that CDI related processes can require as little as 0.12kWh/m^3 when the concentration is below 30 mM, while RO remains at or above 1kWh/m^3 as represented in Figure 1.6.

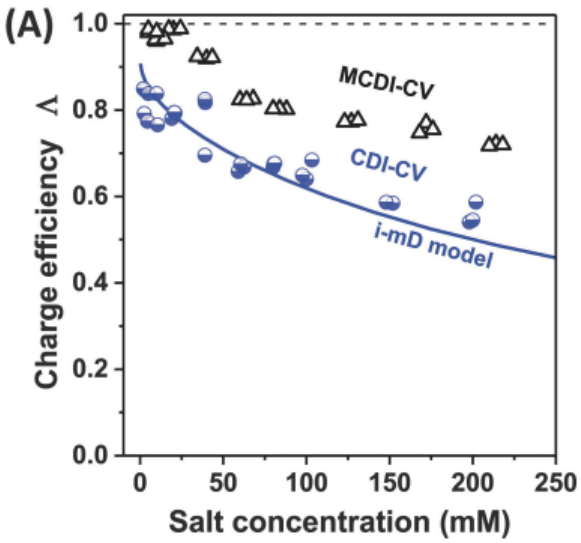

Figure 1.5 Image reproduced from [34] "Selected data for charge efficiency Λ and current efficiency λ as function the salt concentration (A)" by M. E. Suss et. al. and is licensed under CC BY 3.0. Data for charge efficiency are obtained for solid film electrodes at V_{ch} = 1.2 V in a cycle where V_{disch} = 0 V. Solid line denotes calculation results based on the improved mD model.

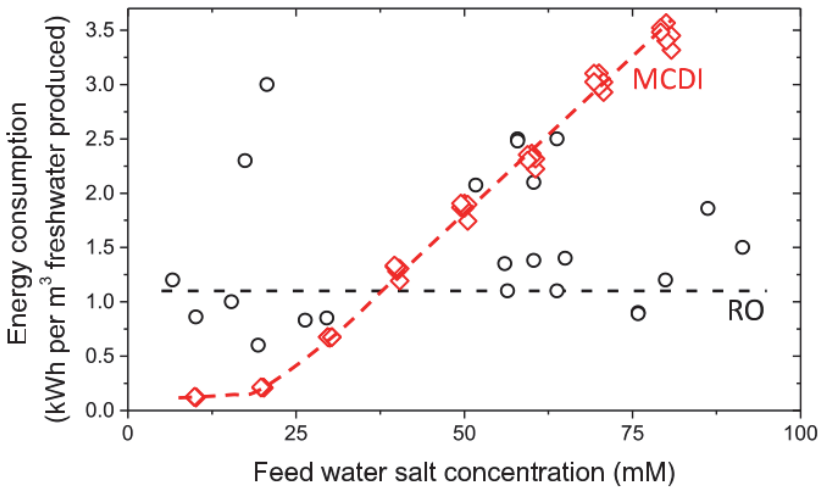

Figure 1.6 Image reproduced from [7] "Energy consumption of water desalination by MCDI and reverse osmosis (RO)" by S. Porada et. al. and is licensed under CC BY-NC-ND 4.0.

These considerations provide motivation toward utilizing Capacitive Deionization methods to treat brackish water efficiently. Another competitive advantage CDI has over other desalination methods is the ability to configure cell pairs in a way that while one cell is discharging, the current can be utilized to help charge the other [37, 38].

1.1.5 Theoretical Models

Understanding the mechanism of ion attraction and transportation between an electrolyte and a charged surface was originally investigated in the mid-1800s by Helmholtz [39]. The initial concept was that at an interface of two media, such as a carbon electrode and NaCl solution, the sum of the charge is equal to zero. Helmholtz assumed that the electrode surface charge would correspond to an equal and opposite accumulation of charge, equating to adsorbed ions. This would translate to a CDI cell having an ideal charge efficiency of 1. However, this concept effectively describes a plane of ions adsorbed to a flat surface is not found with porous media, ions are actually distributed diffusely as described by the Gouy-Chapman layer [40, 41]. Accompanying this is the Stern layer [42], depicted in Figure 1.7A, which acts as a dielectric layer between the surface and the accumulating ions. The thickness of the diffuse layer is estimated to be about 2-3 times the Debeye length, how far the electrostatic effects persist, which is near 3 nm. The diffuse layer interactions are comprised of a combination of ions with charge opposite the electrode, counter-ions, being attracted toward it, and ions of the same charge, co-ions, originally positioned near the carbon surface are repelled when a voltage is applied. This repelling of co-ions also contributes to the electrical current observed, but negatively impacts the amount of counter-ions adsorbed to the surface. This explains why the actual charge efficiency is typically less than one, between 0.6 and 0.8 as observed in Figure 1.5.

Within carbon pores, especially micropores, there is an overlap of these double layers represented in Figure 1.7B. Here the Gouy-Chapman-Stern (GCS) Electric Double Layer (EDL) model is no longer sufficient to describe the adsorption kinetics. Several studies have adapted the GCS model or developed a new one entirely to predict salt adsorption and find agreeable results [43-47]. The most comprehensive and robust model is known as the modified-Donnan (mD) model [17, 48]. The original Donnan model addresses the micropore volume by assuming it contains a constant voltage throughout the entire volume. Improvements on this model are mainly in two parts: first the inclusion of the Stern layer, and second, a term to account for the attraction of ions toward carbon in the absence of a voltage potential [49, 50].

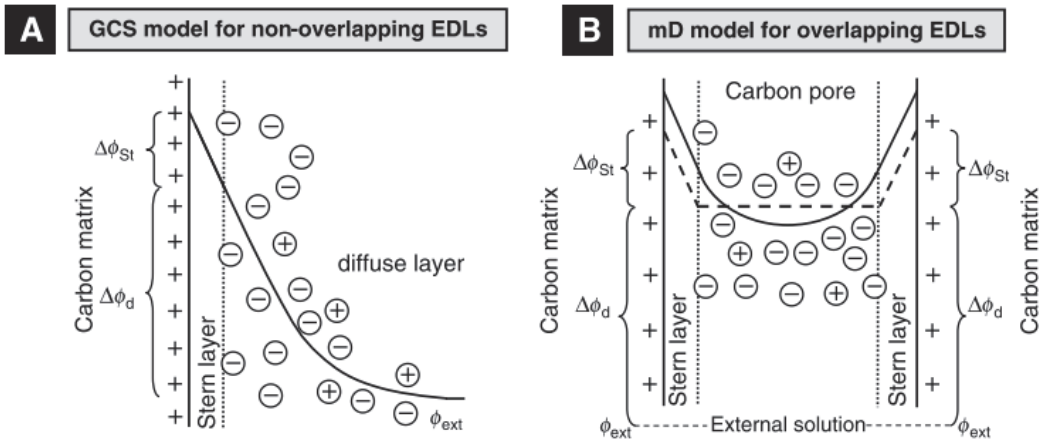

Figure 1.7 Depiction of Gouy-Chapman-Stern model for non-overlapping electrical double layers, A, and the Modified Donnan model for overlapping electrical double layers, B. Reproduced with permission from [49].

1.1.6 Motivation for this Study

This investigation of desalination through the University of Idaho Mechanical Engineering department was initially funded by Vorsana Inc. in 2015. One of their patents [51] involves two counter rotating discs to induce strong a radial counter flow to separate salt from the water. Additionally, and electric field is used to assist in directing ions toward a collection point. Previous studies assessed the feasibility of incorporating a magnetic field to enhance salt recrystallization, however the required magnetic field strength required is far too high for implementation, see CHAPTER 2. An engineering capstone design team at the University of Idaho investigated the fundamental concepts of CDI using model scale channels. Results support the theory of charging capacitors in Eq. (1.1) and are summarized in Appendix A.

A graphene-like thin film called GUITAR, Graphite from University of Idaho Thermalized Asphalt Reaction, was discovered by the Chemistry Department at the University of Idaho under the direction of Frank Cheng [52]. This material shows qualities similar to and even surpassing graphene in areas like conductivity, high corrosion resistance and an extended potential window [53-55]. It can be deposited on surfaces able to withstand high temperatures such as silica wafers, quartz, and carbon-based materials. Current research is focused toward characterizing its electrochemical properties and possibilities in applications such as Vanadium Flow Redox Batteries [56] and sensors [57] and water purification.

The Physics department at the University of Idaho, formerly under the direction of Dave McIlroy, has the capability to grow silicon carbide nanosprings on most substrates [58]. These nanosprings, when coated with GUITAR, can increase specific surface area of the substrate by around 200 m^2/g [53]. Individual nanosprings have a diameter within the range of 10-20 nm and the spiral coil diameter ranges between 70-500 nm [59]. Applications for these nanosprings are in areas such as Hydrogen storage [60], Chemiresistors [61], and sensors [62].

These two materials, GUITAR and nanosprings, can be combined to enhance the conductive surface area of a compatible material like carbon or graphite, see Figure 1.8. Both materials are produced in economical ways which make them competitors to commercial graphene and nanosprings. Therefore, a study of their effectiveness in Capacitive Deionization would contribute highly toward the search for a new electrode material.

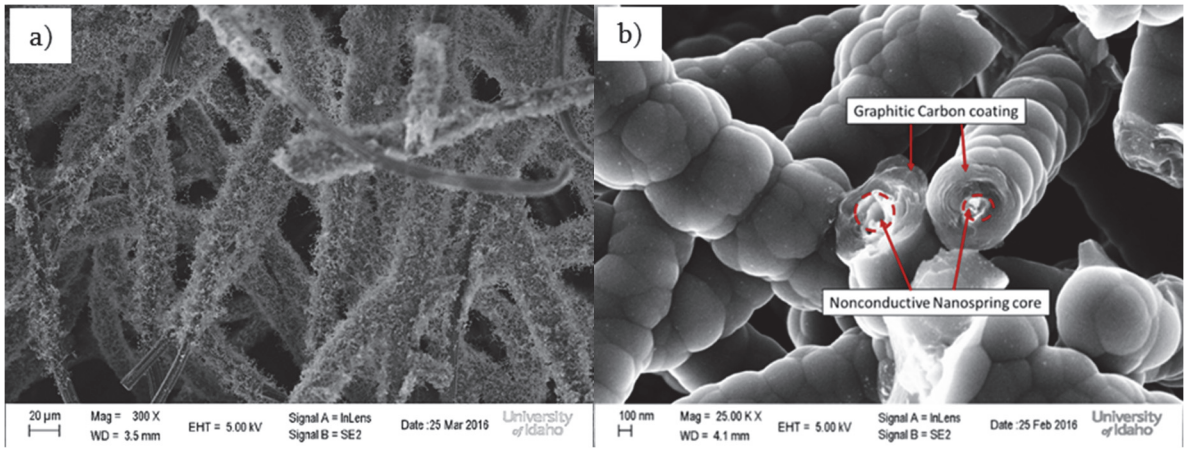

Figure 1.8 SEM images of silica nanosprings, courtesy University of Idaho Physics department, a) grown on SGL graphite felt and b) nanosprings coated with GUITAR.

1.2 Objective and Approach

The objective of this study is to use Capacitive Deionization to evaluate the desalination performance of three different carbon-based electrodes produced at the University of Idaho. These electrodes utilize GUITAR and silica nanosprings to create a conductive network with large pathways for ion transportation, with varied surface area.

The approach taken to this topic of research is through experimentation and modeling, addressed in the order of Figure 1.9. First, a fundamental understanding of capacitive deionization is

developed, proper methods for desalination evaluation established, and the potential for new electrode material is explored. Specifically, the base material for electrodes is selected based on their conductivity and compatibility with a modified Hummers' method. Then electrodes are coated with various thicknesses of GUITAR to determine optimum capacitance. Optimal length of time for the Hummers' method is also determined. Once the best conditions are established, the electrodes are tested for salt adsorption in a small-scale static, batch mode process. Electrodes are tested at two different voltages and two different concentrations. Several methods are explored to evaluate salt adsorption, evaporation, Chloride Ion Selective Electrode (Cl ISE), and conductivity probe. Results are compared to current desalination performance in literature, and suggestions for future research are presented.

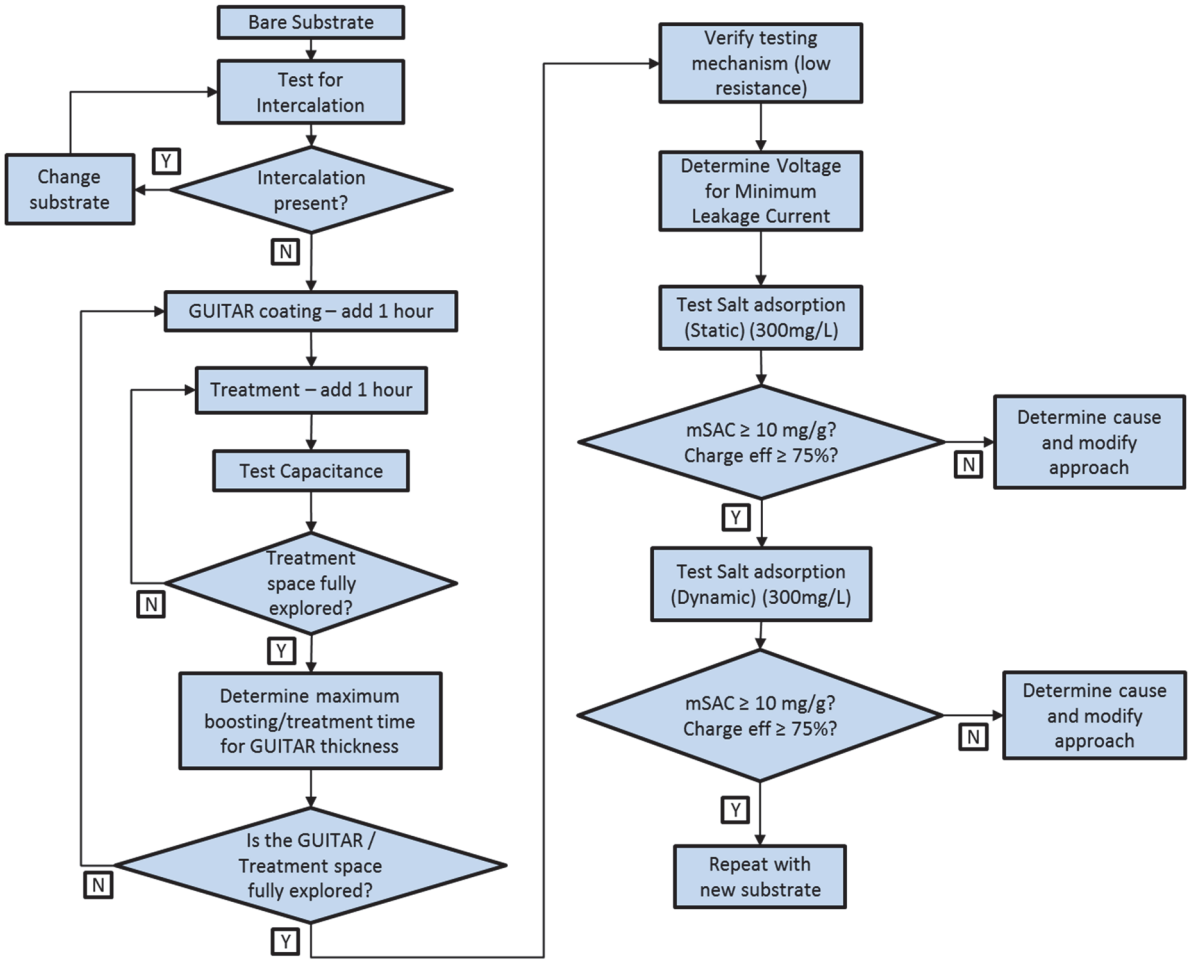

Figure 1.9 Experimental flow chart for Desalination research.

CHAPTER 2 - SMALL SCALE DESALINATION TESTING

2.1 Introduction

This chapter is motivated by the findings from the capstone design team, Appendix A, showing that increased surface area improves salt adsorption capacitance. An investigation of several carbon electrode materials is presented based on compatibility with oxidation treatment as well as capacitive and desalination performance.

2.1.1 Background

The first developments used in this study are the mathematical model of ion motion within a viscous environment with applied electrical and magnetic fields as well as channel prototypes built and tested by an engineering capstone team. The mathematical model shows that using a magnetic field is not feasible to direct ion motion to the walls of a channel. The engineering capstone team designed and tested a straight channel, initially with a 3D printed end cap with three outlets to separate ions near the wall from the main stream. These tests do not yield significant results as the flow is turbulent and mixing occurs. The team then designed a singular outlet end cap and tried two different aspect ratios for the channel. This approach yields appreciable results, confirming the relationships of the capacitance equation. Upon inspection however, the graphite from the channels experienced visible degradation, or exfoliation, after just one test. This is undesirable for a desalination electrode as particulates would contaminate the water.

When the modified Hummers' method discussed previously is applied to graphite foil without GUITAR coating, a severe exfoliation occurs, more than tripling the electrode thickness and rendering it useless as a desalination electrode, see Figure 2.1. This is due to the intercalation of molecules beneath the graphite crystalline layers [55, 63]. This exfoliation can be identified through testing the anodic limits before applying the treatment through Cyclic Voltammetry (CV) with 1M H_2SO_4. Figure 2.2 shows a comparison of the current from such tests, the first from bare graphite foil, and the second from bare graphite felt, another electrode material under consideration. The intercalation peak appears only on the graphite foil. Evidence of intercalation persists even after the conductive thin film material GUITAR, which shows signs of little intercalation, is applied.

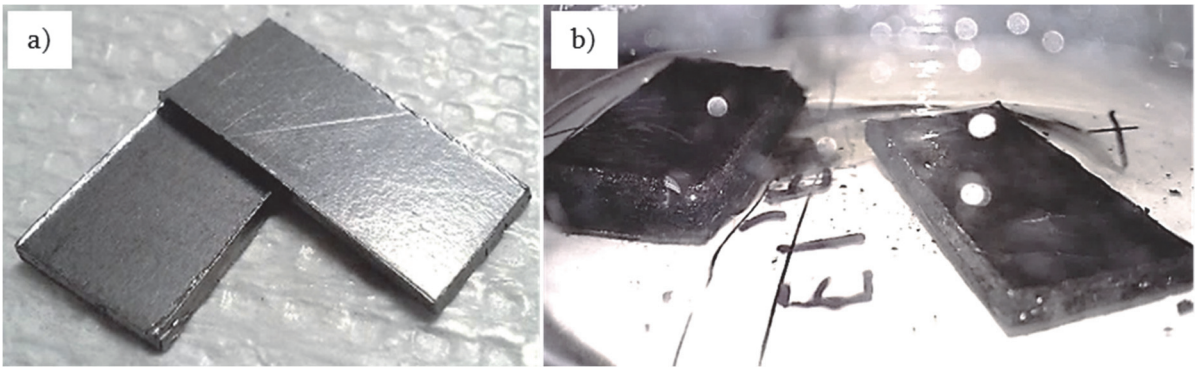

Figure 2.1 a) Graphite foil used for electrodes in capstone design prototypes. b) Exfoliated GUITAR-coated graphite foil electrodes after applying modified Hummers' method.

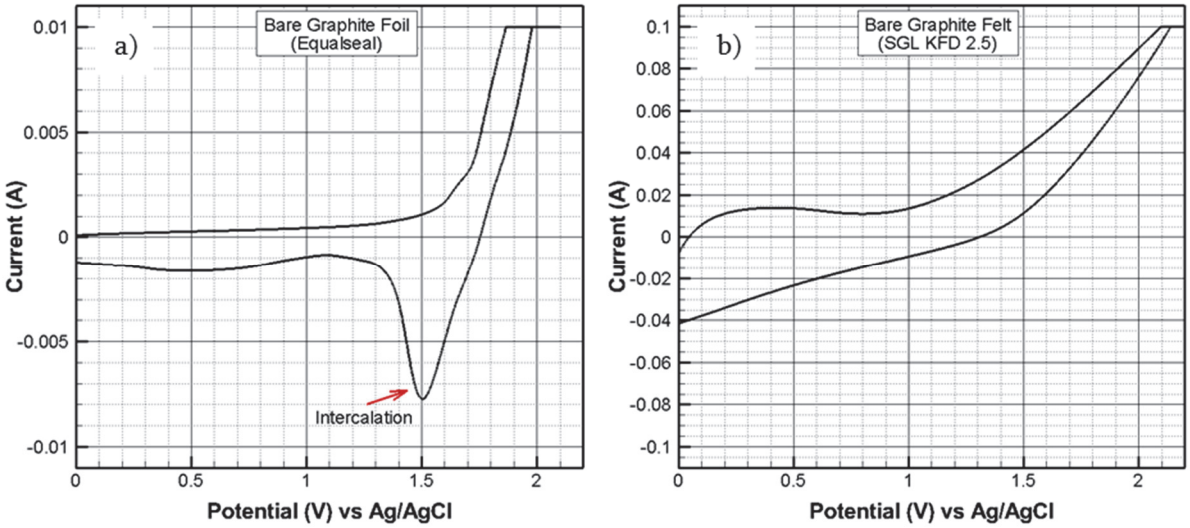

Figure 2.2 Anodic limit tests with CV results sweeping between 0V-2.2V in 1M H_2SO_4 for a) graphite foil and b) bare graphite felt (KFD 2.5). Intercalation peak with graphite foil.

An additional failure is that following the GUITAR coating, the foil forms internal bubbles. This is most likely due to the manufacturing process of compressing two graphite sheets together, resulting in a weakness in the center. Graphite foil is therefore determined unsuitable as the primary electrode substrate and is replaced with graphite felt typically used in battery applications. This material presents a higher surface area than a flat electrode like the foil, and shows no evidence of intercalation.

2.2 Methods

2.2.1 Materials

Figure 2.3 Electrodes used in experiments: a) SGL bare graphite felt, b) GUITAR-coated SGL graphite felt, and c) GUITAR-coated SGL graphite felt with nanosprings.

All electrodes used in this comparison contain the base substrate of bare graphite felt (SGL SIGRACELL KFD 2.5 Battery Felt), hereafter referred to as Bare Felt. Electrodes are cut to be 2.5 cm x 1.1 cm, with a total volume of 0.872 cm^3. Comparisons in this study are made between Bare Felt, GUITAR-coated graphite felt coated for 20 minutes, 60 minutes, and 120 minutes, as well as GUITAR-coated nanosprings on GUITAR-coated graphite felt, see Figure 2.3. GUITAR-coated graphite felt and graphite felt with GUITAR-coated nanosprings are hereafter referred to as GUITAR Felt and GUITAR-NS Felt respectively. The average mass of the electrodes used in each test are 0.0730 g for Bare Felt, 0.0750 g for GUITAR Felt, and 0.2750 g for GUITAR-NS Felt.

Specific surface area as measured using BET measurements for the Bare Felt are reported around 0.6 m^2/g which increases to near 2.6 m^2/g after GUITAR coating. GUITAR-coated nanosprings contribute an estimated 200 m^2/g, bringing the specific surface area of the GUITAR-NS Felt around 20.5 m^2/g.

Electrode contact resistance is measured with a handheld multimeter. Material resistance for the treated Bare Felt, GUITAR Felt, and GUITAR-NS Felt are 15-30 Ω/cm, 4-5 Ω/cm, and 1-3 Ω/cm respectively.

Individual electrode capacitance is measured using a three electrode Cyclic Voltammetry (CV-50W) system, with Ag/AgCl as the reference electrode and carbon basket as the counter electrode. The CV setup and exampled results from this study are represented in Figure 2.4. A sweep rate of 50 mV/sec is used between potentials 0.2 and 0.5V in a solution of 5 mM NaCl for all tests.

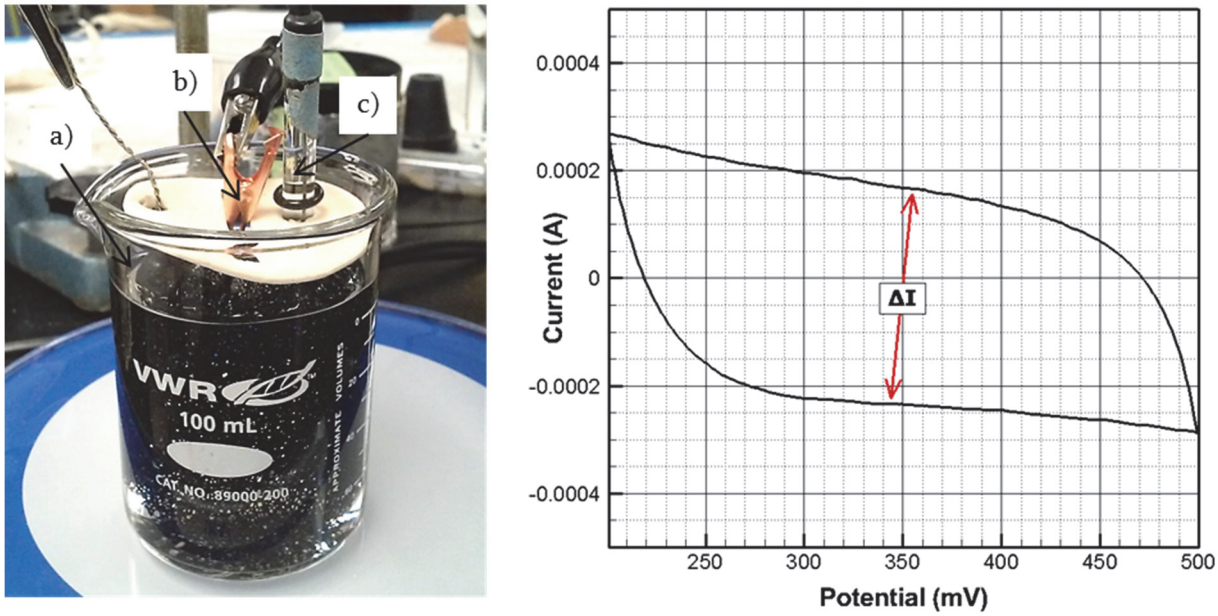

Figure 2.4 Left: 3 electrode CV test cell with a) carbon basket counter electrode, b) working electrode, and c) Ag/AgCl reference electrode. Right: example CV results, where ΔI is the total difference between current at 350 mV.

Capacitance is calculated by dividing the average current by the potential sweep rate.

$$C = \frac{\frac{\Delta I}{2}}{\frac{dV}{dt}} \tag{2.1}$$

Typical means of producing the conductive GUITAR thin film involves either porcelain crucibles or a small quartz tube furnace [64]. The GUITAR in this study is produced using a large quartz tube furnace, heating the substrate and precursor to 900 degrees Celsius. This change accommodates larger sample size and increases the number of samples coated in one batch, Figure 2.5. This increased sample yield is offset by a decrease in precursor concentration, which results in a thinner film at the same amount of coating time.

Some mass loss occurs within the process as the nitrogen used contains a small percentage of oxygen and the felt samples are exposed to high temperatures. This mass loss is measured to determine an optimum range of sample placement within the quartz carrier and furnace, the distribution of which can be seen in Figure 2.6. The amount of GUITAR deposited is also a function of position within the furnace, and varies in a similar fashion as the mass loss.

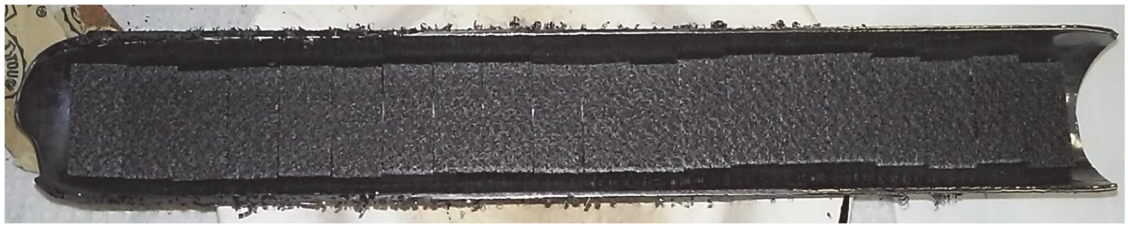

Figure 2.5 Graphite felt samples in quartz boat after GUITAR coating.

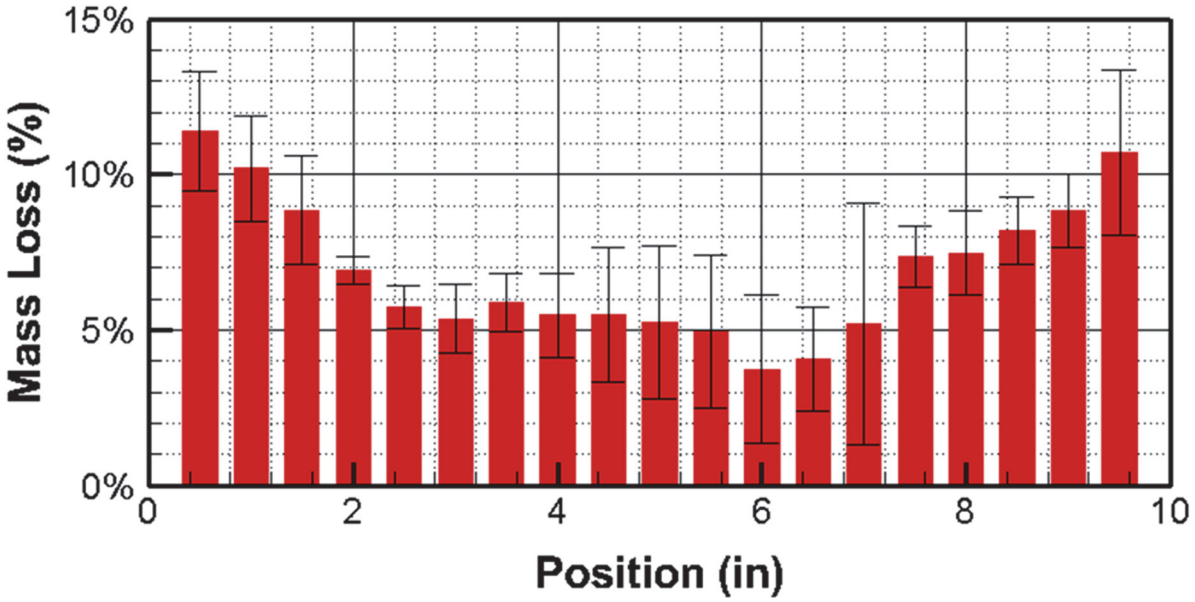

Figure 2.6 Average graphite felt mass loss percent from the 20 minutes of high heat exposure before GUITAR coating, as a function of position along the quartz carrier boat.

The silica nanosprings are infused within the GUITAR Felt using the procedures established in [58]. An overview of the electrode preparation process for this study is represented in Figure 2.7.

A modified Hummer's method is applied to GUITAR for the intended outcomes presented in literature of increased capacitance. The oxidizing solution consists of concentrated sulfuric acid + 0.7M $NaNO_3$ + 1.28M H_2O_2, hereafter referred to as treatment. Lengths of treatment exposure compared in this study are 0, 5, 20, 60, 120, and 180 minutes at 60 degrees Celsius. The electrodes are then thoroughly rinsed with deionized water and ultrasonication before any CDI tests are performed.

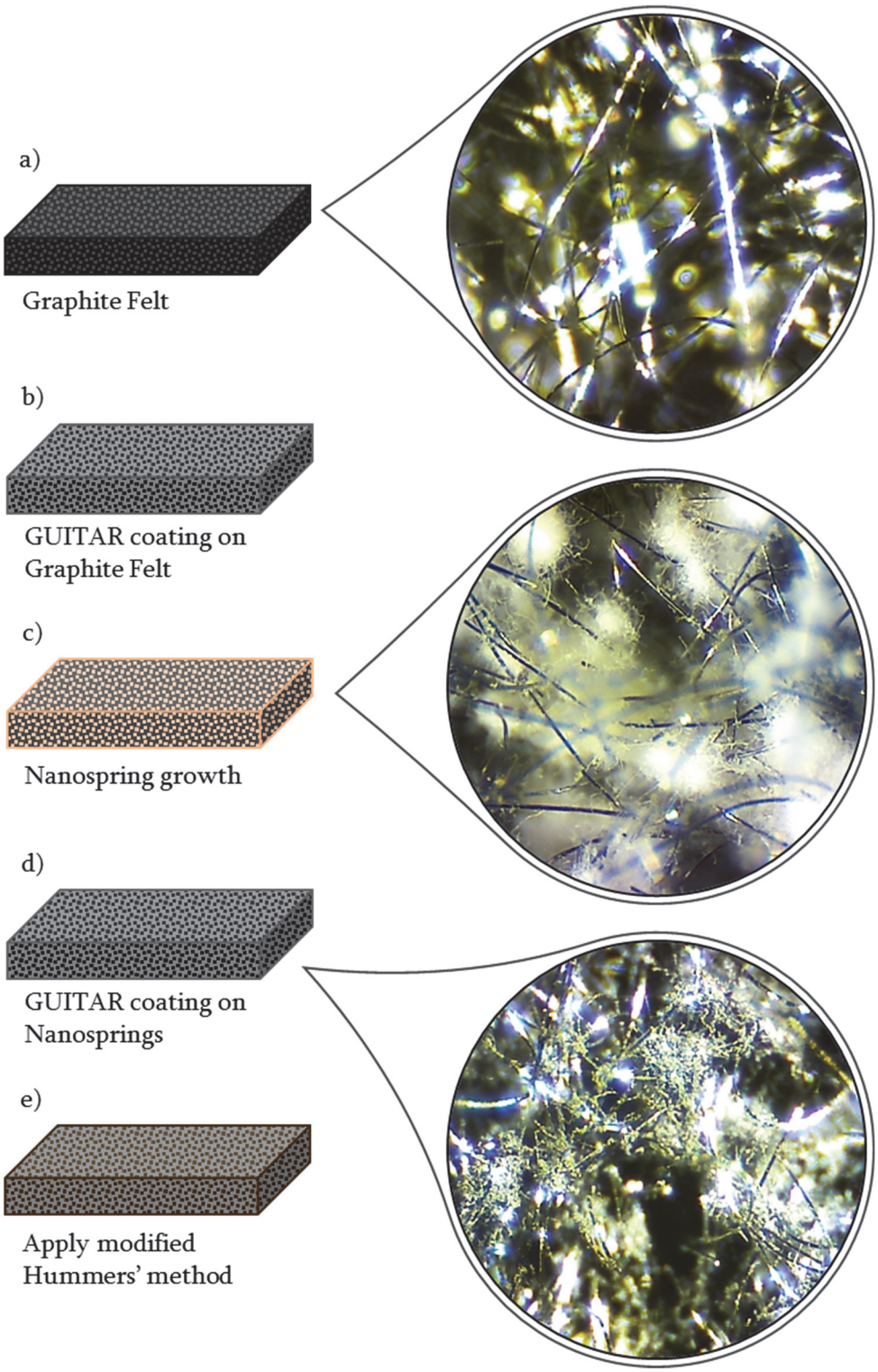

Figure 2.7 Schematic of electrode preparation stages: a) graphite felt electrode is cut to size, b) coated with GUITAR, then either e) treated with modified Hummers' method, or c) prepared for nanospring growth, d) entire substrate coated with GUITAR, and then e).

2.2.2 CDI Test Cell Setup

The CDI tests are performed within a 30ml glass vial initially, and later in an 80ml beaker to decrease sample extraction impact on the test solution concentration, schematically represented in Figure 2.8. The cell voltage potential is applied via Arbin Battery Tester (Arbin Instruments MSTAT BT2000) to the platinum wire current collectors, 0.1-0.25 mm diameter. Graphite felt electrodes are separated by a 25 μm microporous membrane (Celgard 3501) and pressure is applied through a plastic clip at the base. The test electrolyte concentration is either 5 mM or 20 mM NaCl depending on the test, and is constantly stirred for uniform concentration via chemical stir bar.

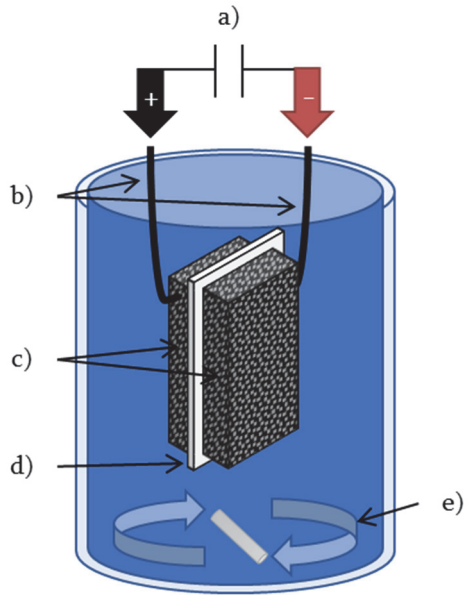

Figure 2.8 Small scale CDI test setup: a) applied potential via Arbin Battery Tester, b) Pt wire current collectors, c) graphite felt electrodes, d) 25 μm separator, and e) stirred NaCl solution.

After treatment, the electrodes are thoroughly rinsed and stored in deionized water. Prior to testing, they are dried in an oven at 130 degrees Celsius for a minimum of 2 hours. The electrodes are soaked in a solution of 20 mM for 2 hours with no voltage potential applied to allow for natural ion adsorption to the uncharged carbon atoms. After soaking, the test voltage is applied for 20 minutes, followed by a 20 minute period of zero potential grounding, and then repeated for a second and third cycle. Operating cell voltages are 1.1V and an optimized voltage determined by current symmetry, described in further detail in 2.3.

Typical experimental arrangements involve an in-line conductivity probe to determine the effluent salt concentration, allowing continuous conductivity data collection simultaneous with the current data. Instrumentation interference from a ground loop occurs when placing instruments in the direct vicinity of the active CDI cell, discussed in CHAPTER 3. Therefore, salt adsorption is measured with sample extraction by precision pipette. Methods and instruments used to quantify salt concentration are evaporation and mass measurement, Chloride Ion Selective Electrode (ISE), and Vernier conductivity probe.

2.2.3 Chloride Ion Selective Electrode Measurement

Test solution samples, 0.2 ml, are extracted every 4 minutes over the duration of both the charge and discharge steps. The extraction samples are then diluted with 7.3 ml of deionized water and 0.15 ml of 5M $NaNO_3$ Ion Stabilizing Activity Buffer (ISAB). The samples are mixed thoroughly and then set aside to settle for several hours before measurement. Cl ISE voltage readings are compared against three calibration sets of standard serially diluted 0.3M NaCl down to $3e^{-5}$M NaCl, also containing a ratio of 1:50 ISAB, see Figure 2.9. A linear fit is applied to the calibration data points and used to calculate the salt concentration of the extraction samples. Calibration readings are recorded and averaged before and after sample testing to ensure accuracy.

The manufacturer provides standard solutions of high and low chloride concentrations, 1,000 mg/L (1,806 mg/L NaCl) and 10 mg/L (18.06 mg/L NaCl) respectively, to suggest a reasonable detection range. The initial CDI tests are performed at a concentration of 5mM NaCl (292 mg/L) which is typically used in literature to easily discern desalination capacity.

The dilution factor of 1:37 mentioned previously corresponds to a salt concentration at or below 7.8 mg/L. This is near the low detection point of the Cl ISE and is determined insufficient to accurately measure desalination. In order to increase measurement accuracy and maintain a low brackish water concentration, the test solution concentration is increased to 20 mM NaCl (1168 mg/L), near 31.5 mg/L after extraction dilution.

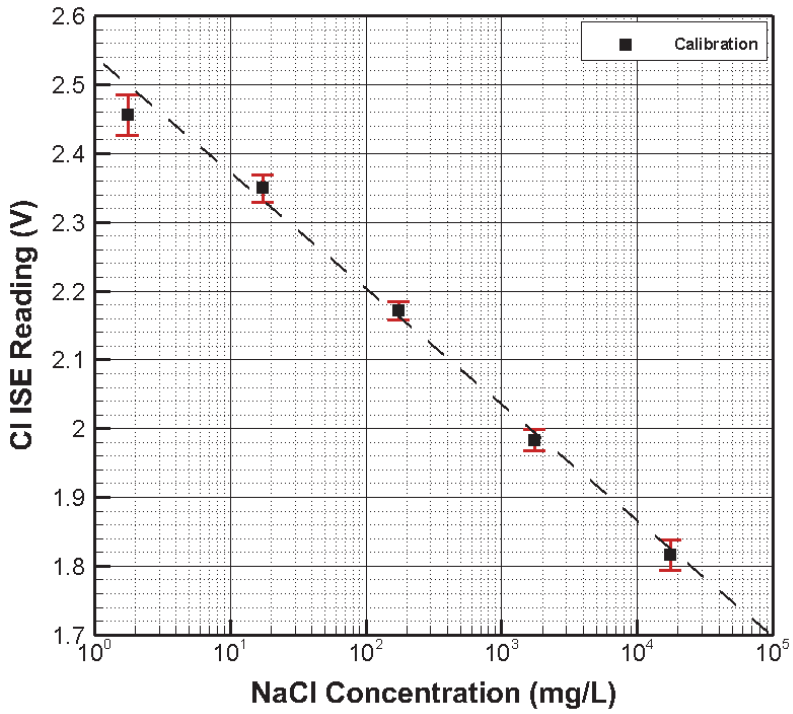

Figure 2.9 Example of Cl ISE calibration points averaged from three different sets, taken before and after sample measurement.

The Cl ISE utilizes the Nernst Equation, to determine the concentration of chloride ions, where 0.05916 is the theoretical slope.

$$E = E_0 + \frac{0.05916}{n} \times \log_{10}\left(Cl^-\right) \tag{2.2}$$

Using the calibration method defined earlier, the actual slope and intercept of the linear fit can be determined and rearranged as follows to calculate the chloride ion concentration within the cell.

$$Cl^- = \frac{1}{vol} \times 10^{\frac{V_{meas} - b}{m}} \tag{2.3}$$

Here V_{meas} is the measured voltage from the Cl ISE, and vol is the volume of the extracted sample before dilution. To convert the chloride concentration to sodium chloride the following relationship is used

$$NaCl\left(\frac{mg}{L}\right) = 1.8065 \times Cl\left(\frac{mg}{L}\right) \tag{2.4}$$

2.3 Results and Discussion

2.3.1 Capacitance Boosting

Initial tests with Bare Felt and GUITAR Felt showed that the addition of GUITAR alone does not improve capacitance. This is in part associated with the hydrophobic nature of GUITAR, and thus the modified Hummers' method discussed earlier is considered. Previous experiments in the Chemistry lab revealed that applying a 3 hour treatment to GUITAR coated on a quartz slide achieved a maximum boosting of capacitance by a magnitude of near 200 times [65]. The substrate material and GUITAR deposition method used in these previous experiments are different than the current study, requiring a new study on optimized treatment time. The design of experiment involves the Bare Felt with various GUITAR coating times in the large tube furnace and various treatment exposure times to determine the conditions for maximized capacitance boosting.

The results of varying the length of treatment time are displayed in Figure 2.10 where electrodes of three GUITAR thicknesses are represented through coat times of 20, 60, and 120 minutes. Maximum capacitance was achieved for all samples within 20 minutes of exposure as opposed to 3 hours. The hypothesis for this is because the larger tube furnace yields a thinner layer of GUITAR in comparison to other methods. Maximum specific capacitance for the Bare Felt, 20, 60, and 120 minute GUITAR Felt are 5.09 μF, 8.35 μF, 8.11 μF, and 8.84 μF respectively. The treatment positively impacts the capacitance of all GUITAR-coated electrodes, boosting by an average of 16 times, while the Bare Felt is negatively impacted.

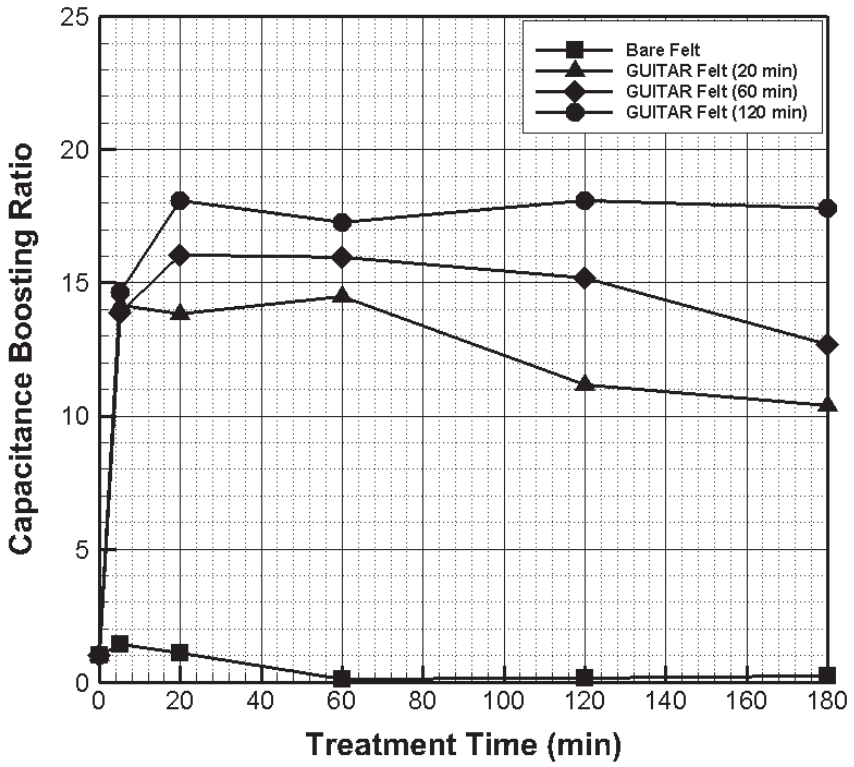

Figure 2.10 Capacitance from single electrode CV for various thicknesses of GUITAR, represented by 20, 60 and 120 minutes of coating, and applied treatment times of 5, 20, 60, 120, and 180 minutes (conc. H_2SO_4 + 0.7M $NaNO_3$ + 1.28M H_2O_2).

2.3.2 Addressing Hydrophobicity

One of the characteristics that GUITAR possesses similar to graphene is that it is highly hydrophobic which reduces the effectiveness of the electrode in desalination. While applying the Hummers' method dramatically increases hydrophilicity, it also modifies the surface with Quinone groups. A short study is performed with three methods of electrode wetting: initial wetting with isopropanol alcohol, Plasma Prep III for 1 minute, and 20 minutes of treatment, results compared in Figure 2.11. For all instances of the GUITAR-coated electrodes, the capacitance from applying 20 minutes of treatment is more than double the capacitance from other wetting methods. This suggests that simply addressing the hydrophobic nature of GUITAR, i.e. with isopropanol alcohol, is not the main contributor to maximizing capacitance boosting.

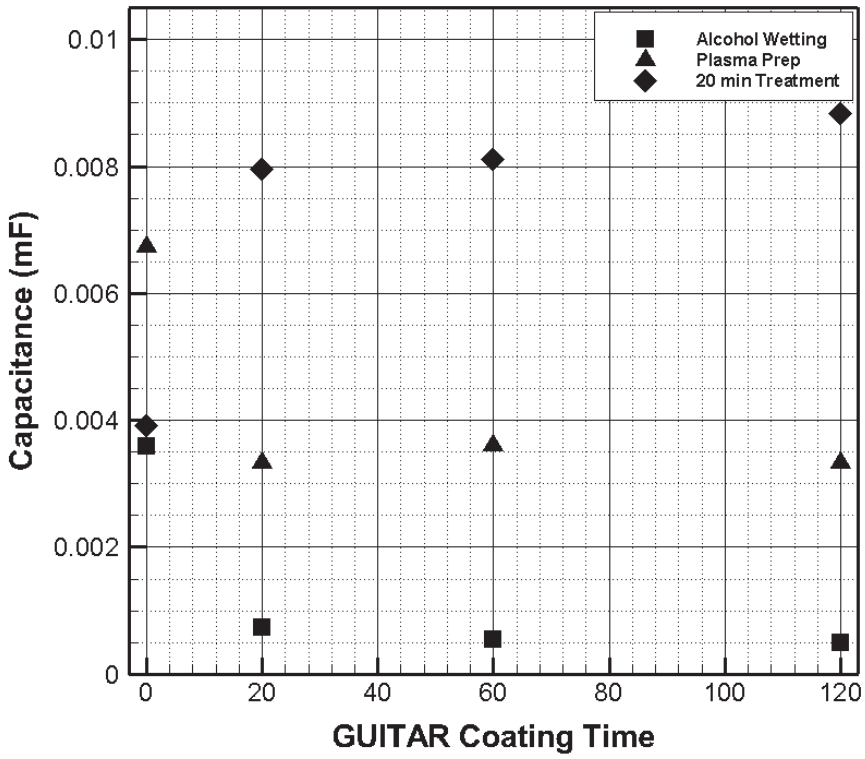

Figure 2.11 Capacitance from single electrode CV in 5mM NaCl, 50mV/sec sweep rate between 0.2-0.5V for GUITAR Felt with 0, 20, 60, and 120 minutes of coating, using different wetting mechanisms; isopropanol alcohol, Plasma Prep, and modified Hummers' method at 20 minutes.

2.3.3 CDI Results – Initial

Results from the first CDI experiments are presented in Figure 2.12, where salt adsorption capacity is calculated from conductivity measurements and uses the entire electrode mass. Here evidence suggests that the GUITAR Felt has a higher capacity than nanosprings, and both have a higher capacity than the Bare Felt. This trend is supported by the previous findings from capacitance boosting. This is promising, however confidence in experiment repeatability is low due to the large error bars, so other methods of salt detection are investigated.

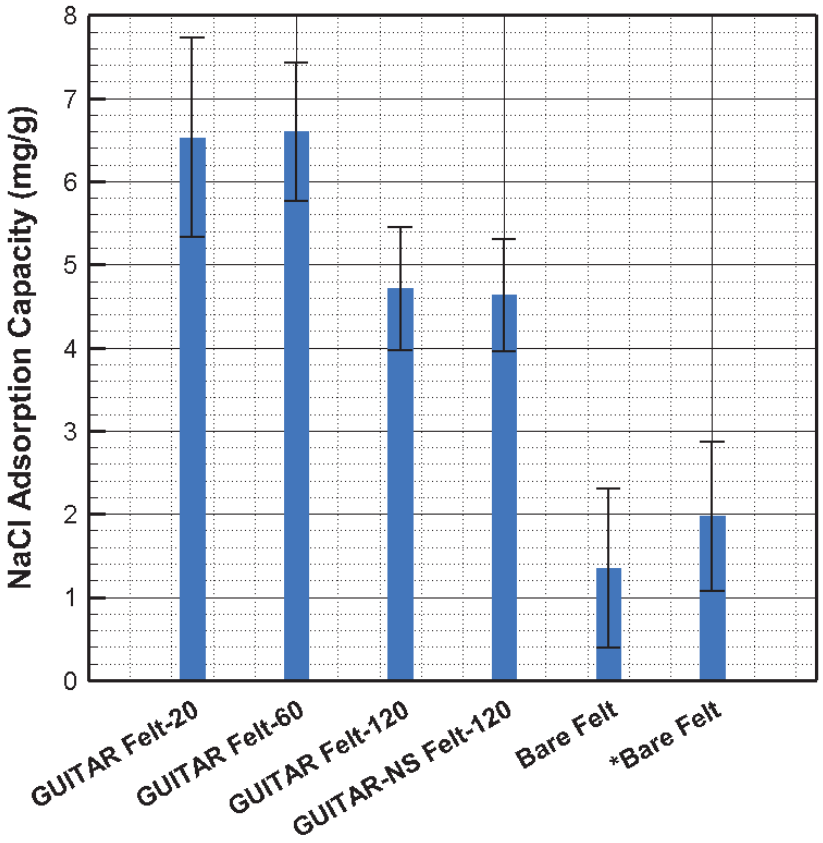

Figure 2.12 Initial salt adsorption results of GUITAR Felt with 0, 20, 60, and 120 minutes coating and GUITAR-NS Felt all with 20 minutes modified Hummers' method applied (except *Bare Felt). Adsorption based on conductivity change from initial sample to sample after 9 minutes of charging at 1.2V in 5mM NaCl.

2.3.4 Addressing Leakage Current

While performing preliminary CDI tests with the electrodes, it was observed that although the current decays to a plateau, representing complete ion saturation, it does not always converge upon zero current, see end of charge step in Figure 1.2. This residual current during the charge step may indicate corrosion or some other reaction from the current collectors or electrode. A short experiment is performed to investigate whether the exposed current collector causes the residual current by isolating the current collector from the electrolyte with paraffin wax. No significant difference resulted, indicating the parasitic reaction or corrosion must be from the electrode.

A series of adsorption and desorption tests are performed with each electrode over a range of potentials from 0.6-1.2V, each having been treated for 20 minutes, represented in Figure 2.13, Figure 2.14, and Figure 2.15 by a-g. The current is recorded while the cell is charged for 60 seconds and then discharged at zero volts for 180 seconds to allow sufficient electrode regeneration. The test solution is 5 mM NaCl, the same as previous desalination experiments. For each electrode, as the voltage potential increases, the difference between the charge and discharge current at 60 seconds, representative of the leakage current, also increases.

This relationship between voltage and leakage current is supported by [44, 66, 67] and is attributed to corrosion or parasitic reactions. Recommended methods to help minimize these unwanted reactions are reducing dissolved oxygen content, lowering the cell potential, or simply subtracting it when calculating salt adsorption capacity. In this study, the test results are used to determine an optimum voltage where the ratio of charge to discharge current after 60 seconds are close to symmetrical, or greater than 80%. The discharge current profile shows no evidence of the leakage current, as it decays to zero, and is determined to represent the true salt adsorption capacity. A plot of the ratios with respect to applied potential in Figure 2.16 shows Bare Felt is acceptable at a voltage below 0.6V, while GUITAR Felt is acceptable up to 0.7V, and GUITAR-NS Felt up to 0.8V.

The charging behavior of the electrodes can be determined by fitting the discharge current profile with both exponential and double exponential curve fits. The current from an ideal capacitor follows a single exponential behavior, while a double exponential curve indicates there are two time constants, a quick charge like an ideal capacitor and a slow charge from ion diffusion. Each discharge current curve is fitted with both a single and double exponential curve fit, represented by either 1 or 2 respectively in Figure 2.13, Figure 2.14, and Figure 2.15. Without exception, the discharge curve is best described using a double exponential curve fit, suggesting that the charge process involves the diffusion of ions and the Electric Double Layer. This is important to consider in future modelling of ion motion in CDI.

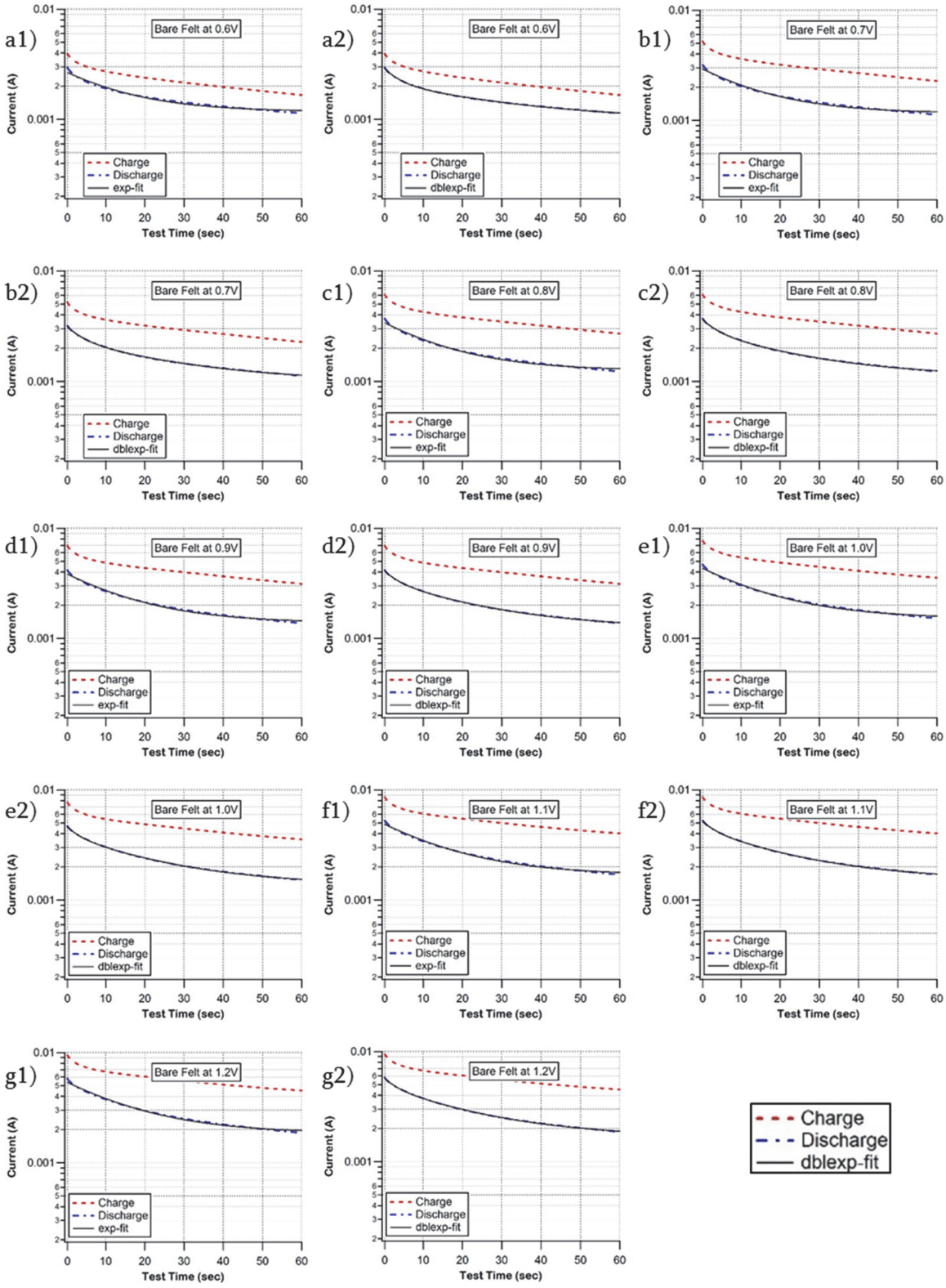

Figure 2.13 Study of leakage current from Bare Felt as a function of applied voltage, ranging from 0.6V-1.2V, a-g respectively. Discharge current is fitted with 1) an exponential and 2) a double exponential.

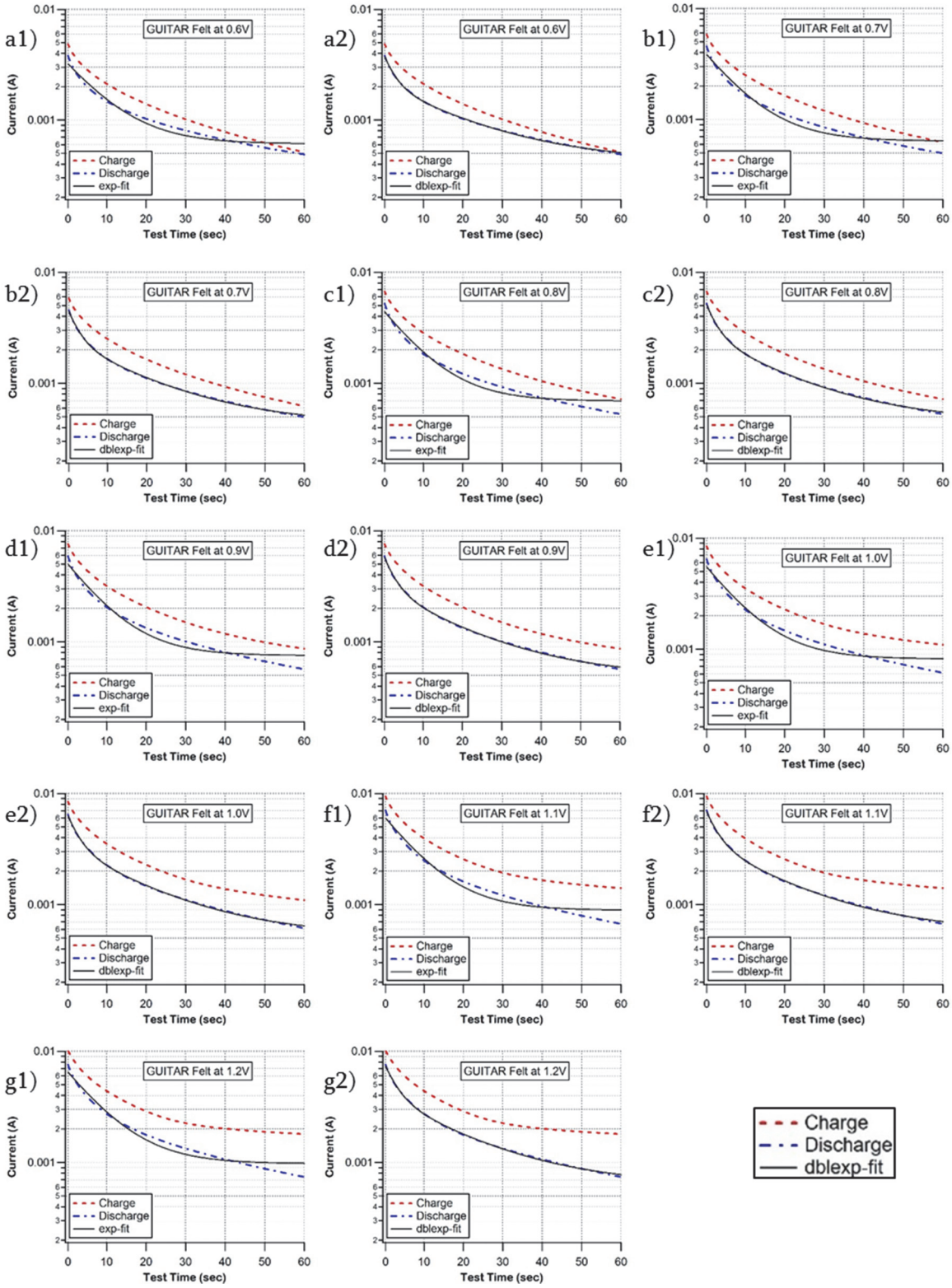

Figure 2.14 Study of leakage current from GUITAR Felt as a function of applied voltage, ranging from 0.6V-1.2V, a-g respectively. Discharge current is fitted with 1) an exponential and 2) a double exponential.

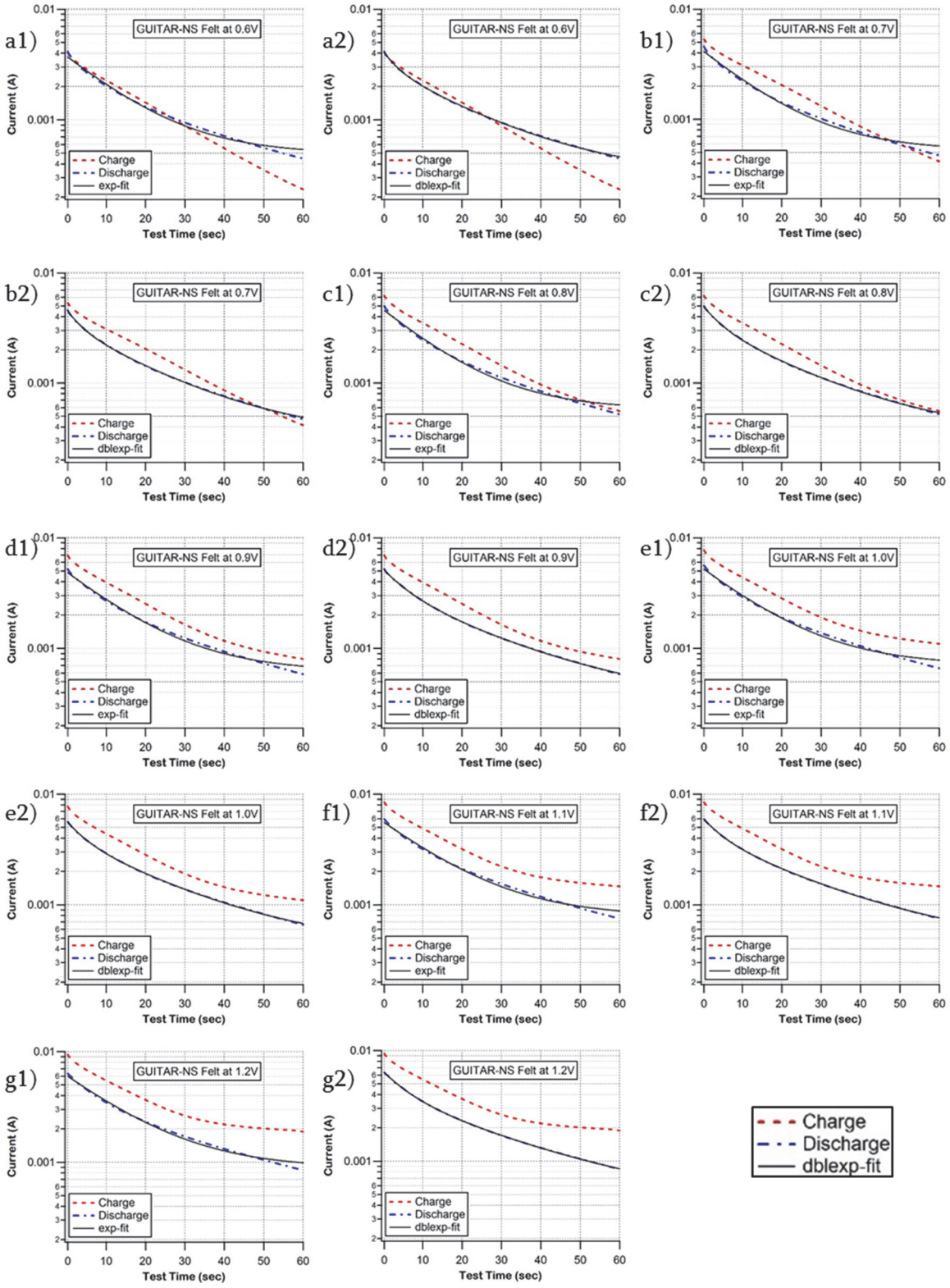

Figure 2.15 Study of leakage current from GUITAR-NS Felt as a function of applied voltage, ranging from 0.6V-1.2V, a-g respectively. Discharge current is fitted with 1) an exponential and 2) a double exponential.

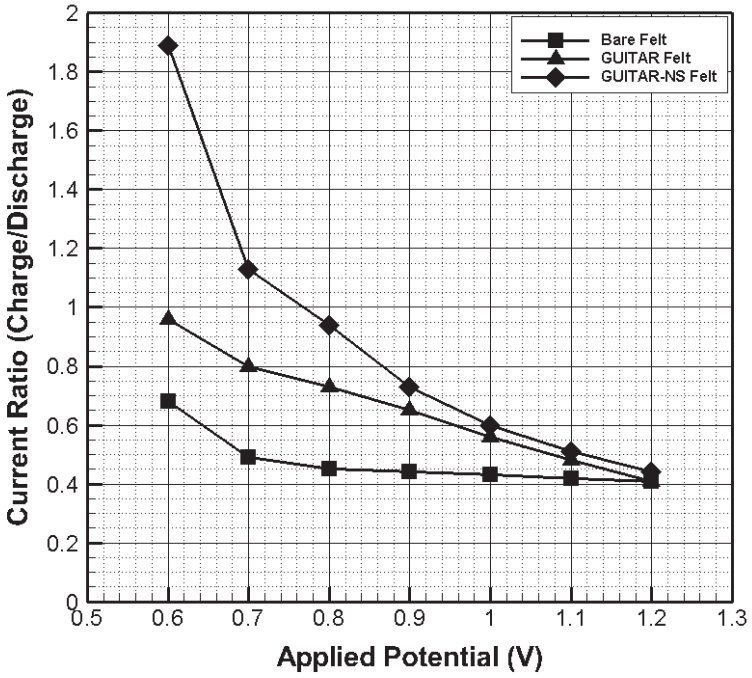

Figure 2.16 Ratios of charge current to discharge current values after 60 seconds at voltages between 0.6-1.2V. Values above 0.8 were determined as acceptable for symmetry of charge and discharge profiles.

2.3.5 CDI Results – Evaporation

One alternative method of salt adsorption detection is based on evaporation and mass difference. The procedure involves obtaining the initial dry mass of a glass beaker and filling it with deionized water. The CDI cell is operated within a separate test beaker, and is removed from the test cell just before the switch point of zero cell grounding. It is quickly inserted into the glass beaker filled with deionized water to allow ion discharge. After a full discharge, the water is evaporated from the beaker and the dry mass is measured again. Theoretically, the mass difference represents the amount of salt adsorbed.

The results from the experiment are shown in Figure 2.17 against a white and black backdrop for visibility. Although the measured mass difference was 3.3 mg for the GUITAR Felt and 2.3 mg for GUITAR-NS Felt, which corresponds to 22 and 4.2 mg/g mSAC values respectively, there are several concerns. This method presents uncertainties in mass measurement, extra salt solution removed via water droplets on the electrodes and current collectors, and the presence of carbon particles in the solution. Since GUITAR is brittle and is coated on small fibers, these small carbon

particles result naturally from electrode handling. This method is therefore determined unsuitable for accurately measuring salt adsorption.

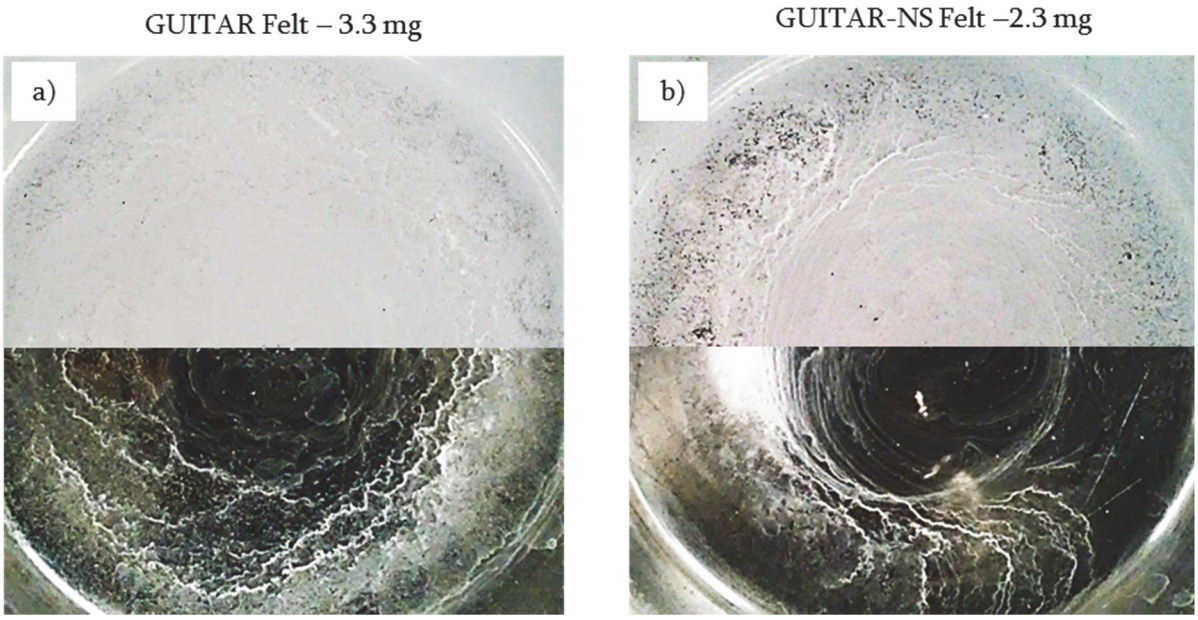

Figure 2.17 Evaporated remains after CDI tests for a) GUITAR Felt and b) GUITAR-NS Felt. White and black backdrops reveal the presence of both salt and carbon particles.

2.3.6 CDI Results – Cl ISE

The next method investigated in measuring NaCl adsorption is the Cl Ion Selective Electrode. Using the procedure outlined in the methods section previously, current profiles from operating the CDI cell and electrodes at their respective optimum voltages are presented in Figure 2.18. Here the residual current at the tail end of the charge portion is successfully reduced. The magnitude of charge accumulated is interesting because Bare Felt accumulates the most charge, then GUITAR Felt, and least amount of charge is accumulated by the GUITAR-NS Felt. The calculated salt content as a function of test time is represented in Figure 2.19. Here GUITAR Felt shows the most adsorption, and GUITAR-NS the least, but all following the same decreasing trend.

Additional CDI tests were performed at 1.1V, Figure 2.20, to demonstrate performance at a high voltage similar to literature and commercial operation. Here the leakage current is visible, especially with the Bare Felt. The calculated salt content from the Cl ISE readings as a function of test time is represented in Figure 2.21. Here again GUITAR Felt shows the most adsorption, while

GUITAR-NS and Bare Felt are similar but less. What is interesting to note here is that at a higher voltage, the salt adsorption is less than at the optimized voltages.

In both test cases, the salt concentration decreases during the charge step in a manner similar to other batch mode processes. However, during the discharge step the concentration continues to decrease as opposed to increasing back up to the initial concentration. This result may be due to error in the experiment or unaccounted for salt adsorption to the uncharged carbon surface. A test comparing the measured adsorption between CDI cells with a potential of 0.7V applied and the same cells without any voltage applied for the same length of time is presented in Figure 2.22. In both cases the electrodes are rinsed with DI water, dried in an oven, and then placed in 5 mM NaCl for 2 hours before operating the cell for 45 minutes.

The recorded salt adsorption results from this test show GUITAR-NS Felt and GUITAR Felt with greater adsorption than Bare Felt. The trend of continued decrease is present in both accounts, and the adsorption magnitude of the cell with no voltage exceeds the adsorption of the cell with an applied voltage for each electrode. This indicates either that the dominating adsorption in these tests is the natural adsorption, or there is some experimental error in either the sample extraction or Cl ISE readings.

The large magnitude of salt adsorbed and variation of results suggests that this method of detecting salt adsorption is insufficient for such low concentrations and sample extraction. Calculating the charge efficiency based on the measured salt adsorption and accumulated charge from integrating the current results in values significantly greater than 1. Therefore, it is determined to revisit measuring electrolyte conductivity, as it is the method consistently presented in literature.

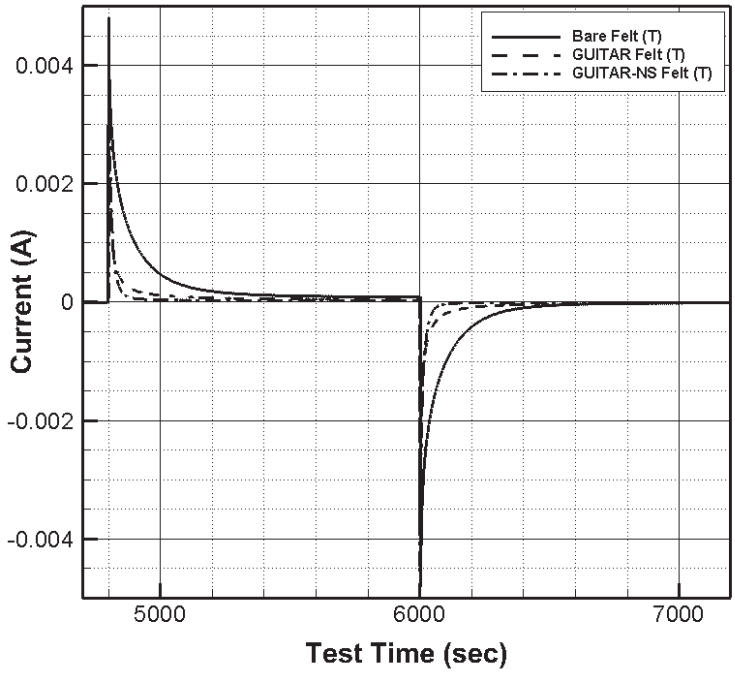

Figure 2.18 CDI Current profiles from third cycle at optimized voltages in 20 mM NaCl.

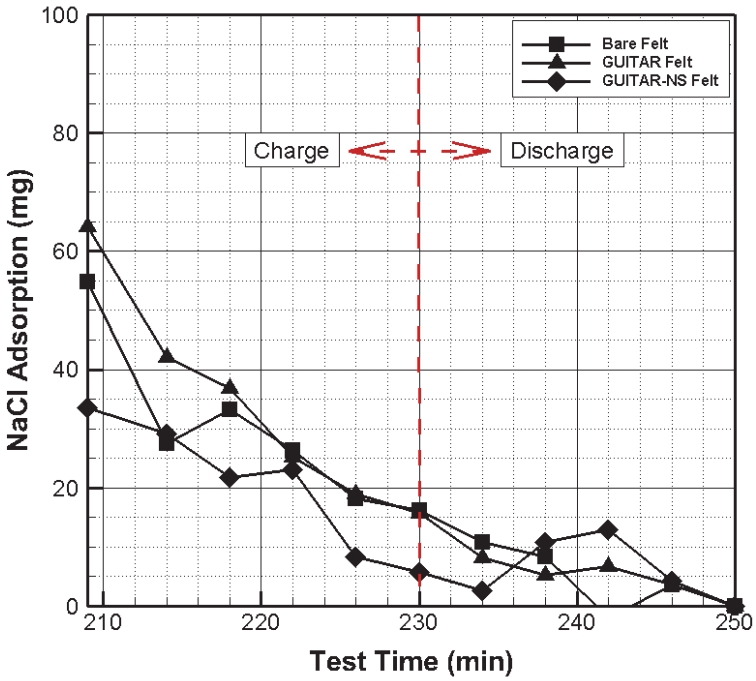

Figure 2.19 Normalized CDI salt adsorption detected at optimized voltages using Cl ISE. Charge step occurs between 210-230 minutes, and discharge step between 230-250 minutes.

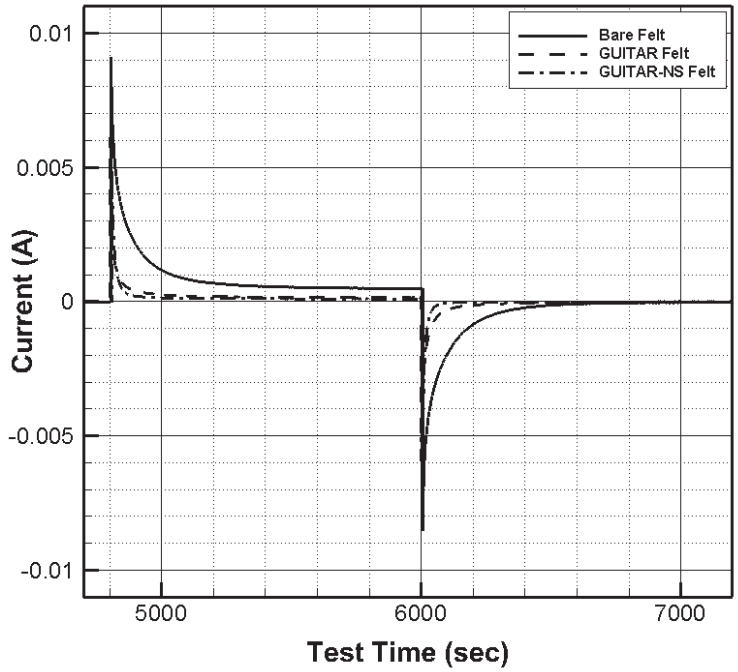

Figure 2.20 CDI Current profiles from third cycle at 1.1V in 20 mM NaCl.

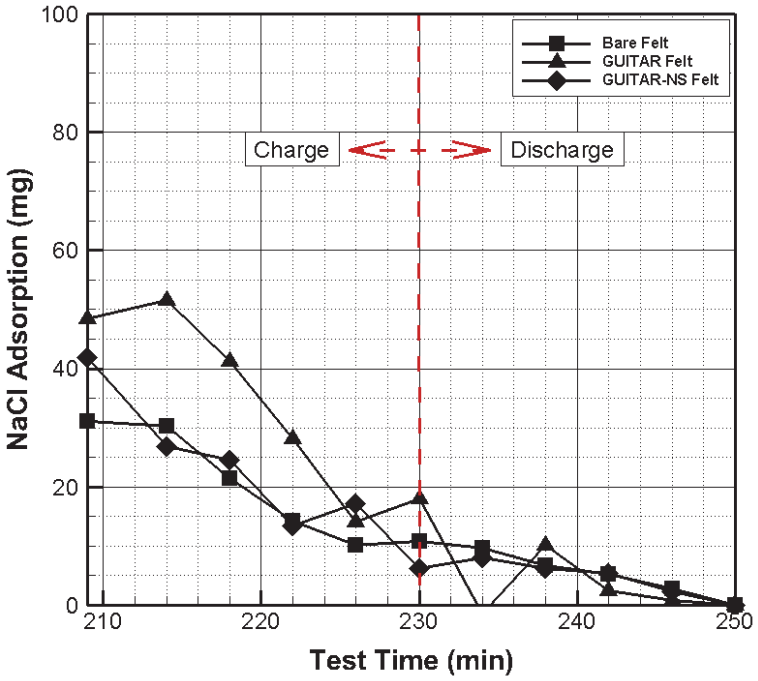

Figure 2.21 Normalized CDI salt adsorption detected at 1.1V using Cl ISE. Charge step occurs between 210-230 minutes, and discharge step between 230-250 minutes.

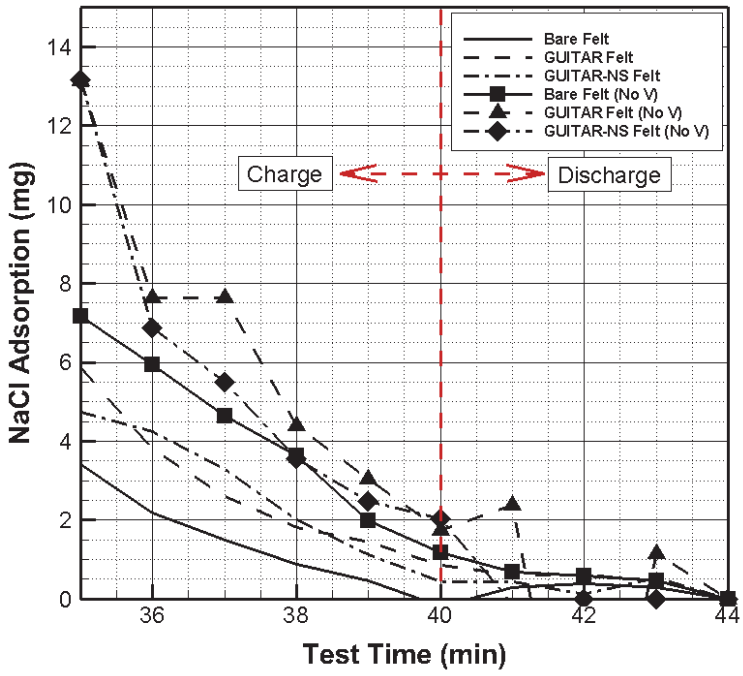

Figure 2.22 Comparison of Cl ISE results at 0.7V applied and no applied voltage over the same length of time.

2.3.7 CDI Results – Conductivity

Here the test conditions of 2.3.6 are repeated with the exceptions of concentration being measured using the conductivity probe and the extraction sample size is doubled to 0.4 ml to increase detectible concentration. Increasing the sample size requires a reduction in the number of sample points to minimize impact on the overall cell concentration.

The current profiles of both the optimized and 1.1V tests resemble those in the previous section, drawing the same conclusions of Bare Felt accumulating the most charge, then GUITAR Felt, and then GUITAR-NS with the least, see Figure 2.23 and Figure 2.25.

The conductivity probe results, Figure 2.24, do not show the same overall trends as those presented by the Cl ISE previously. The data is relatively flat for each and there is no prominent change during either the charge or discharge steps, suggesting very little salt adsorption. The results from operating each set of electrodes at 1.1V, Figure 2.26, shows slightly more variation with decreasing trends during the charge step and increasing trends during the discharge step. Unfortunately, the variation is within the uncertainty of the conductivity probe.

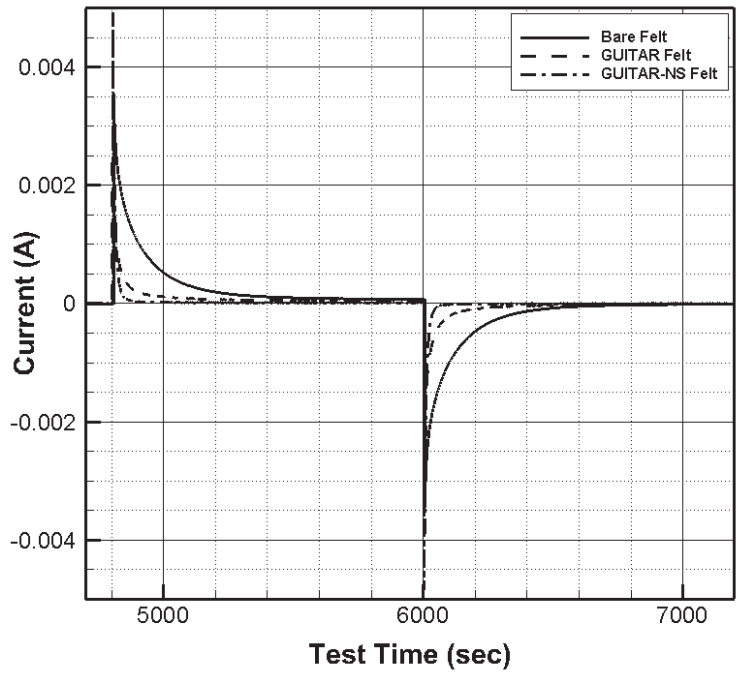

Figure 2.23 CDI Current profiles from third cycle at optimized voltages in 20 mM NaCl.

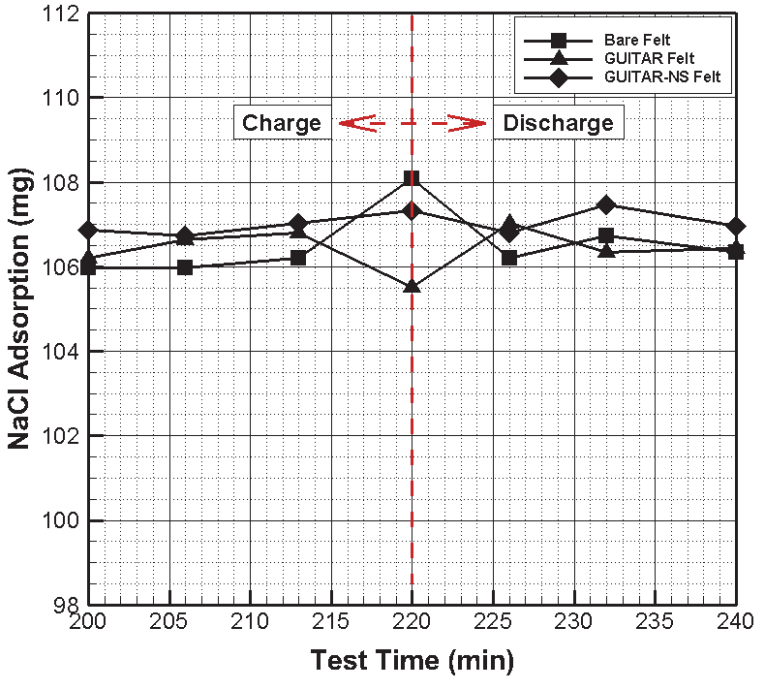

Figure 2.24 CDI salt adsorption detected at optimized voltages using conductivity. Charge step occurs between 200-220 minutes, and discharge step between 220-240 minutes.

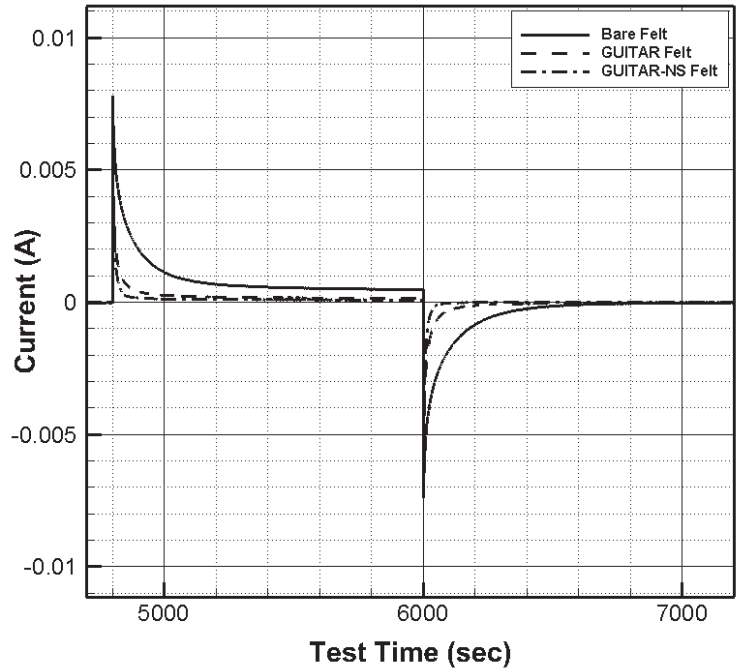

Figure 2.25 CDI Current profiles from third cycle at 1.1V in 20 mM NaCl.

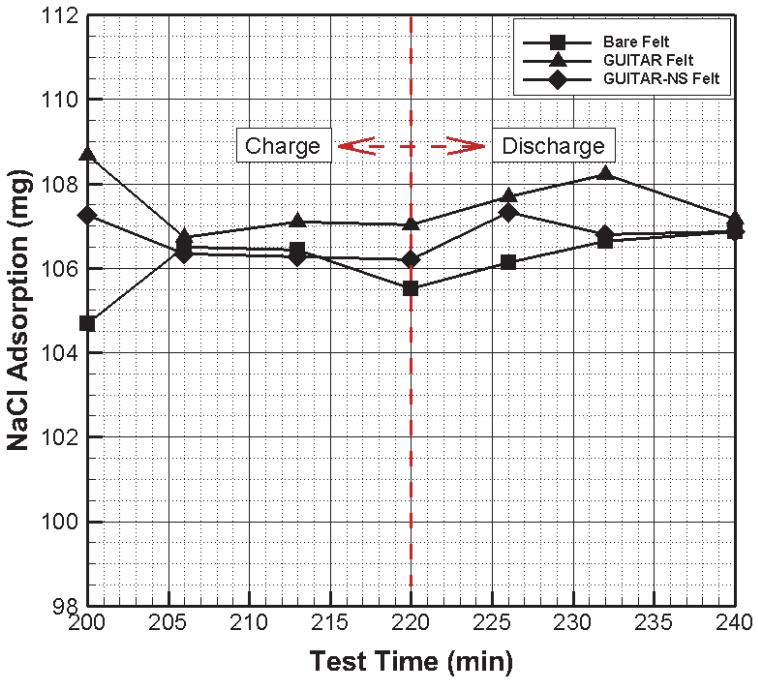

Figure 2.26 CDI Salt adsorption detected at 1.1V using conductivity. Charge step occurs between 200-220 minutes, and discharge step between 220-240 minutes.

The maximum salt adsorption capacity values are calculated using the difference between start and end values of charge step conductivity and utilize the entire electrode mass, including silica nanosprings. Measured mSAC values along with the calculated charge accumulation and resulting charge efficiency are presented in Table 2.1 and Table 2.2. The negative mSAC values and charge efficiency magnitudes greater than 1 suggest the CDI test setup may have issues to be resolved. For comparison purposes, a theoretical mSAC value is also presented which uses the measured charge accumulation and an assumed charge efficiency of 0.8, see Figure 1.5. The current profiles present the same trends, regardless of measurement instrumentation or operating voltage and is considered a more reliable method of determining salt adsorption in this study. These mSAC values are no greater than 2 for Bare Felt and decrease by roughly an order of magnitude to GUITAR Felt and then GUITAR-NS Felt, suggesting a lower surface area than materials used in literature.

Table 2.1 Comparison of mSAC and charge efficiency values for optimized voltage tests.

Substrate	$mSAC_{ACT}$ (mg/g)	Charge (C)	Λ_{ACT}	$mSAC_{\Lambda=0.8}$ (mg/g)
Bare Felt	-14.44	0.306	-11.33	1.02
GUITAR Felt	4.51	0.109	10.22	0.35
GUITAR-NS Felt	-0.78	0.04	-18.57	0.03

Table 2.2 Comparison of charge efficiency and mSAC values for 1.1V tests.

Substrate	$mSAC_{ACT}$ (mg/g)	Charge (C)	Λ_{ACT}	$mSAC_{\Lambda=0.8}$ (mg/g)
Bare Felt	-5.66	0.595	-2.28	1.98
GUITAR Felt	11.03	0.172	15.84	0.56
GUITAR-NS Felt	1.81	0.062	27.96	0.05

2.3.8 CDI Results – Larger Electrode

As results are still within the uncertainty of the detection device, a test is performed to investigate the effect of increasing the geometric area of the electrode. The Bare Felt electrode area is increased from 1.1 cm x 2.5 cm to 6 cm x 2 cm. The same CDI cell test procedure used in previous

tests is applied, operating at 1.1V. Current profiles and adsorption data from this electrode are represented alongside the other electrodes from 1.1V tests in Figure 2.27 and Figure 2.28.

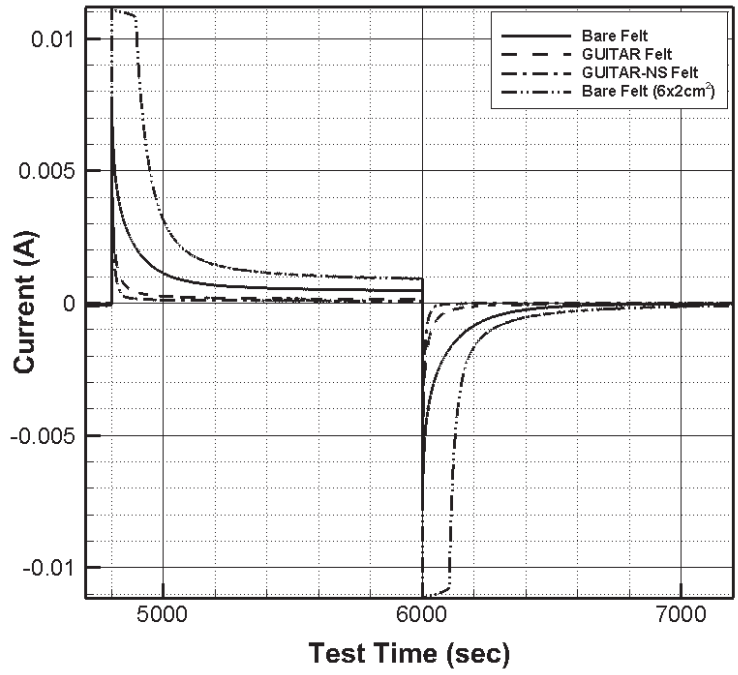

Figure 2.27 CDI Current profiles from third cycle at 1.1V in 20 mM NaCl.

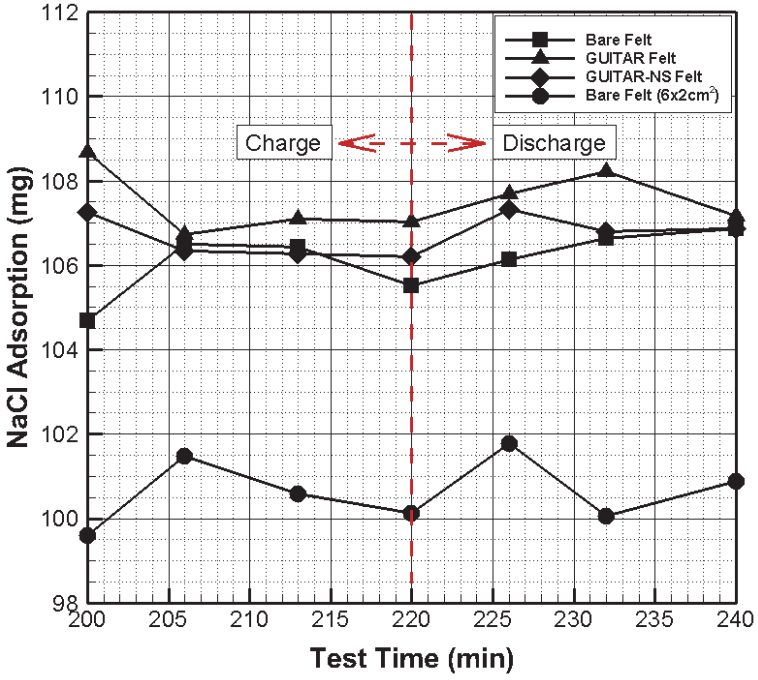

Figure 2.28 CDI Salt adsorption detected at 1.1V using conductivity, including 6x2 cm^2 Bare Felt. Charge step occurs between 200-220 minutes, and discharge step between 220-240 minutes.

2.4 Conclusions

As discussed previously, the porosity of a material is a large contributing factor to the electrode adsorption capacity. The current profiles from each test performed indicate that the Bare Felt has a greater capacity for salt adsorption over both GUITAR Felt and GUITAR-NS Felt electrodes. It is known that the Bare Felt is a porous material and GUITAR is not, which suggests that the GUITAR coating process is inhibiting ion access to the pores. Introducing a modified Hummers' method does increase the capacitance of the GUITAR-coated electrodes by an order of magnitude.

Introducing silica nanosprings to the GUITAR Felt, although increasing the surface area in BET measurements, shows a reverse impact on the adsorption capacity. One contributing factor to this is that in the preparation process, there is a GUITAR coating deposited before and after the nanosprings are grown. This is intended to ensure continuity of the GUITAR coating to help with electrical conductivity. This additional amount of GUITAR only increases the effective barrier to the pores.

Increasing the size of the electrode used made little difference in the amount of salt adsorbed during the CDI test. It can be concluded that while the Bare Felt is porous, it does not have sufficient specific surface area to adsorb enough salt for an appreciable difference in the test solution concentration. Of the three methods investigated, the conductivity probe is the most realistic and reliable method of salt adsorption, but an electrode with larger adsorption capacity is needed to improve confidence in observed measurement.

CHAPTER 3 - DYNAMIC FLOW CELL DESIGN

3.1 Introduction

This chapter discusses the instrument interference which motivated sample extraction for gathering salt adsorption data and its significance for future testing. A CDI cell design is presented to address dynamic flow conditions and incorporate in-line conductivity measurement.

3.1.1 Background

The current study investigates CDI using batch mode tests within a single open beaker, Figure 3.2a, for ease of electrochemical testing. Typically in literature the CDI system design is similar to Figure 3.1 where conductivity is measured in-line. A simple test is performed to evaluate the two arrangements, Figure 3.2, and their impact on conductivity probe readings, Figure 3.3. It is found that significant interference occurs when the conductivity probe is placed in the direct vicinity of the active cell, while very minor interference is measured with the probe in a remote location.

This interference does not come from the magnetic stir plate because the solution in each scenario is constantly stirred. It is also not related to salt adsorption since the drop is immediate, where adsorption is time dependent on the minute time scale, even with a uniformly mixed solution. The IEEE [68] defines this with the term 'ground loop' when two grounds are connected by a conducting path, in this case saline solution, in a way that one or both are not at the same ground potential. The tubing bridge provides enough distance and electrical resistance to dampen the interference effects and is therefore a reliable method to detect real-time conductivity changes.

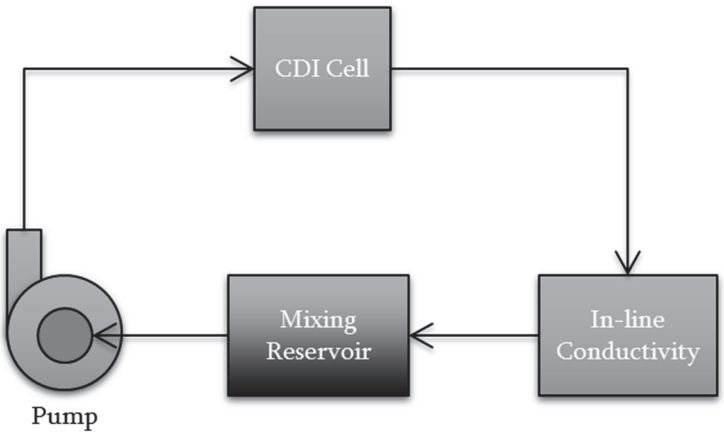

Figure 3.1 Schematic of dynamic flow system for CDI testing.

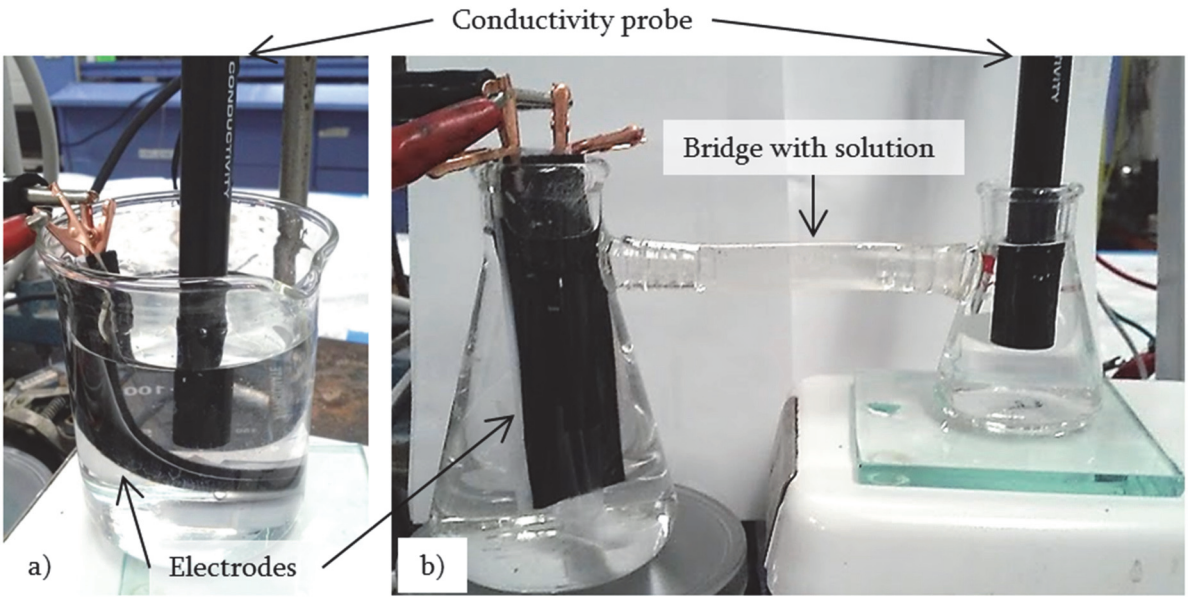

Figure 3.2 Two configurations for conductivity measurement: a) conductivity probe in direct vicinity of active cell, and b) conductivity probe in a remote location connected by a tube with NaCl solution.

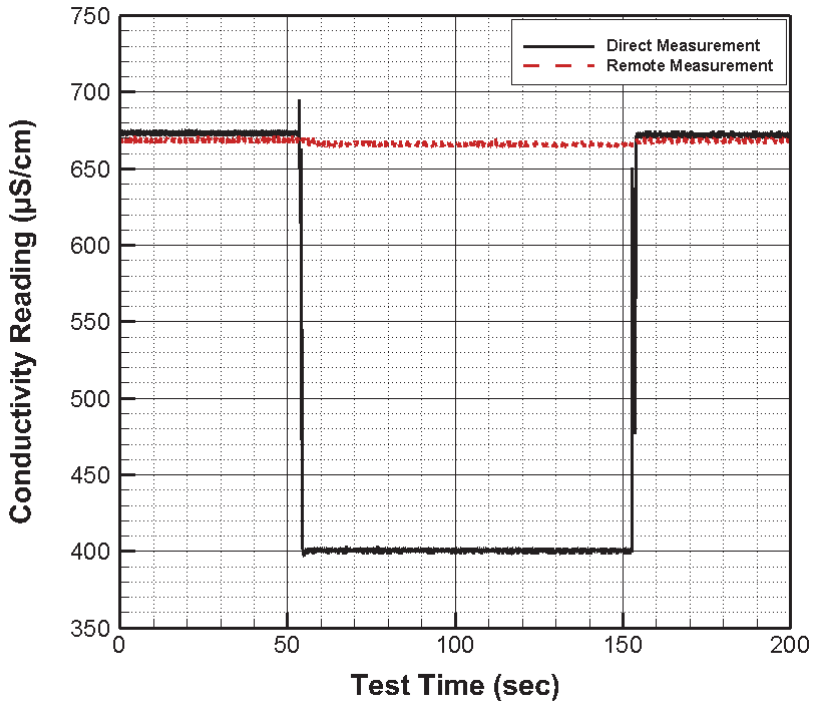

Figure 3.3 Conductivity probe readings for direct and remote probe placement in NaCl solution. Voltage is applied to the CDI cell only between 60-150 seconds.

3.2 Cell Design

A CDI cell is most effective when housed in an enclosure that allows moderated electrolyte flow past the electrodes, minimizes the dead volume, has the ability to incorporate multiple stacks, and measures both current and conductivity continuously. Such a configuration can accommodate both single pass and batch mode operation. Methods for capacitive deionization cells typically follow the designs set forth in the patent by Tran et al [69]. Here are presented similar designs for such a housing and system, see Figure 3.4.

As the current study investigates graphite felt electrodes, the housing is designed for such electrodes. The model can be manipulated to accommodate various electrode area, thickness, and configuration. The housing is designed to be machined out of clear acrylic with slots for the graphite current collector, electrode, and rubber O-ring. A microporous membrane is to be placed between the electrodes, and the entire assembly compressed together to minimize distance between electrodes and ensure a good seal. The electrolyte will enter the cell through one hole, and pass by the electrodes through to the other hole to either be recirculated or the next cell. The cell is designed in such a way that multiple cells could be stacked to increase the effective electrode surface area, allowing more substantial desalination effects to be observed.

Two prototypes of the cell were created to determine feasibility of design and gain feedback from stakeholders. The first is 3D printed with ABS plastic, directly representing the CAD design, Figure 3.5a. The second was machined in the machine shop, incorporating changes from a circular O-ring channel to a rectangular channel for ease of machining, see Figure 3.5b.

The system would require appropriately sized tubing, adapters for the housing, a peristaltic or other low volume displacement pump, conductivity meter, and potentiostat such as the Arbin instrument used in previous experiments. This addresses the need for remote conductivity measurement to allow continuous data as well as CDI testing.

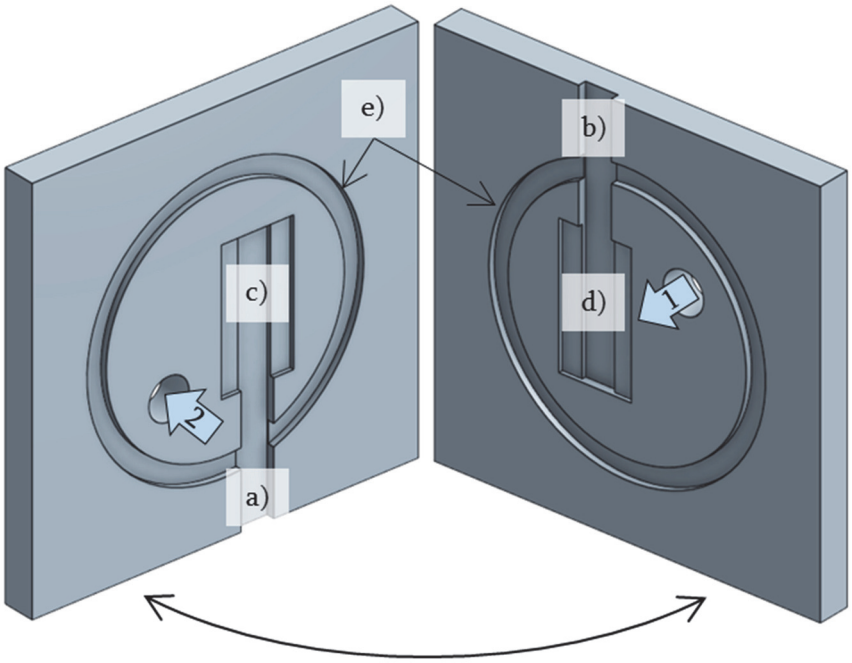

Figure 3.4 3D model of flow cell housing design: a) and b) slots for graphite current collectors, c) and d) slots for test electrodes, and e) slot for rubber O-ring. Arrows indicate flow direction.

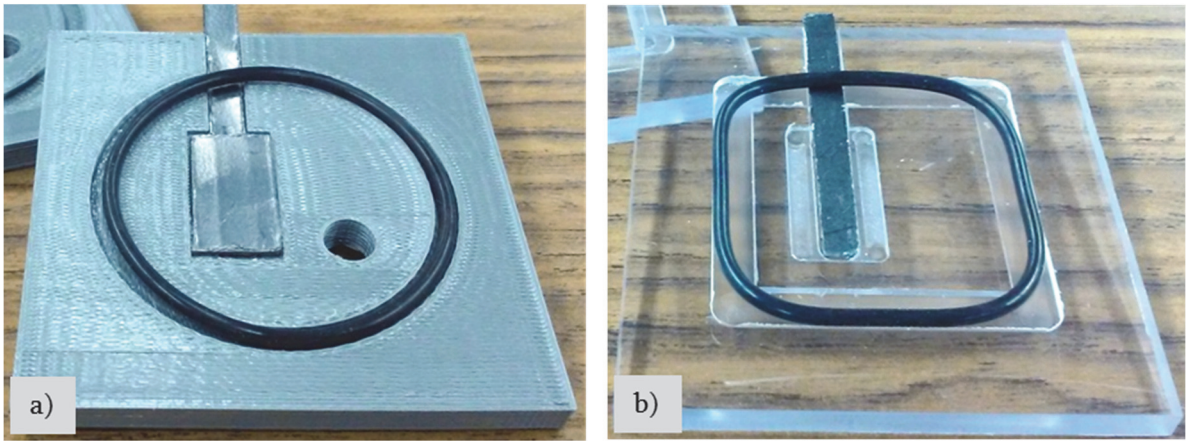

Figure 3.5 a) 3D printed prototype of flow cell housing with graphite current collector and rubber O-ring. b) Flow cell housing machined in the University of Idaho machine shop.

CHAPTER 4 - ION MOTION MATHEMATICAL MODEL IN ELECTRIC AND MAGNETIC FIELDS

4.1 Introduction

This chapter is motivated by the proposal by Vorsana Inc. to incorporate both magnetic and electric fields into a desalination process. Here a mathematical model describing ion motion influenced by combination of perpendicular electric and magnetic fields in both free space, vacuum, and salt water environments is presented. Resources used as a basis for the scenarios are supported by [70, 71].

4.1.1 Problem Description

The setup of this analysis is a 1" square channel with a flow rate of 0.1 gallons per minute (gpm) or velocity of 0.0098 meters per second. Although desalination involves both Na and Cl ions, in order to create a conservative model, the following calculations incorporate Cl, as it has the larger mass. In modeling the ion trajectory, the starting position is taken along the centerline of the channel. The current model assumes the salt ions have already dissociated and overcome the intermolecular force between them.

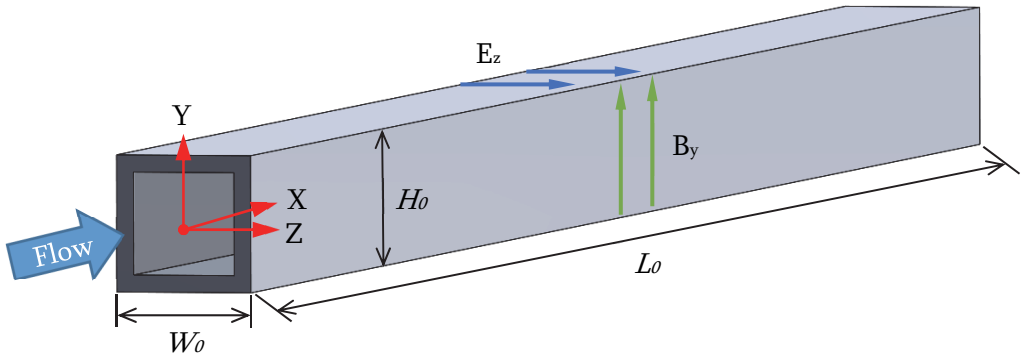

Figure 4.1 Reference coordinate system relating to electric and magnetic field analysis.

The governing equation for ion motion within magnetic and electric fields is the Lorentz force [72] equation

$$\boldsymbol{F} = m\boldsymbol{a} = q\left(\boldsymbol{E} + \boldsymbol{V} \times \boldsymbol{B}\right) \tag{4.1}$$

Where q is the ion charge, $\boldsymbol{E}$, is the electric field, $\boldsymbol{V}$ is the velocity, and $\boldsymbol{B}$ is the magnetic field. It is comprised of two parts, a force due to the electric field, $q\boldsymbol{E}$, and due to the magnetic field $q(\boldsymbol{V}\times\boldsymbol{B})$. As a convention, the fields are oriented as shown in Figure 4.1 with the direction of flow in the positive x direction. These fields are examined within environments of static and dynamic vacuum or salt water. Each environment is subject to three different field scenarios: electric field only, magnetic field only, and a mixed field of orthogonal electric and magnetic fields.

4.2 Electric Field Only (Vacuum)

4.2.1 No Initial Velocity (Vacuum)

A stationary charged ion within a vacuum subject to a uniform electric field of strength $\boldsymbol{E}$ will begin to accelerate to the oppositely charged side due to the Lorentz force

$$\boldsymbol{F} = m\boldsymbol{a} = q\boldsymbol{E} \tag{4.2}$$

This acceleration is constant with a magnitude of Eq. (4.3) in the direction of the electric field.

$$\frac{dw}{dt} = \frac{qE_z}{m} \tag{4.3}$$

The velocity as a function of time is found by integrating Eq. (4.3) to get

$$w(t) = \frac{qE_z}{m}t \tag{4.4}$$

By integrating Eq. (4.4), the z position is found

$$z(t) = \int \frac{dw}{dt} = \int \frac{qE_z}{m}tdt = \frac{qE_z}{2m}t^2 + c \tag{4.5}$$

With the initial conditions of $z = 0$ and $w = 0$ at $t = 0$, the integration constant is zero.

Solving (4.5) for t gives the time it takes the ion to reattach to the channel wall, t_R

$$t_R = \sqrt{\frac{2zm}{qE_z}} \tag{4.6}$$

The x position of the ion can be modeled for any time using

$$x = u_0 t \tag{4.7}$$

Allowing the reattachment length, L_R, to be found using the time obtained in Eq. (4.6)

$$L_R = u_0 t_R \tag{4.8}$$

In this case u_0 is zero and therefore so is L_R. See Table 4.1 for parametric study with different field strengths.

4.2.2 Initial Velocity Normal to the Field (Vacuum)

If ion has an initial velocity in the x direction within a vacuum, the only change is the reattachment length. This is determined by applying the initial condition of $u_0 = V_0$ in Eq. (4.8).

The displacement in the z direction is also expressed by Eq. (4.5) at any time t by substituting

$$z = \frac{qE_z}{2m} t^2 = \frac{qE_z}{2m} \left(\frac{x}{u} \right)^2 \tag{4.9}$$

The trajectory is parabolic in nature as observed in Figure 4.2 for an ion when E_z is 1000 V/m, mass, m, is 5.89e^{-26} kg, q is 1.602e^{-19} C, and V_0 is 3e^5 m/s. This velocity is much higher than would be feasible, but demonstrates the parabolic curvature and a reattachment length near 1 m. More realistic velocities would result in a very short reattachment length.

$$z = \frac{1.602 \times 10^{-19} C}{5.89 \times 10^{-26} kg} \times \frac{1000 \frac{V}{m}}{2} \times \frac{x^2}{(3 \times 10^5 \frac{m}{s})^2} \tag{4.10}$$

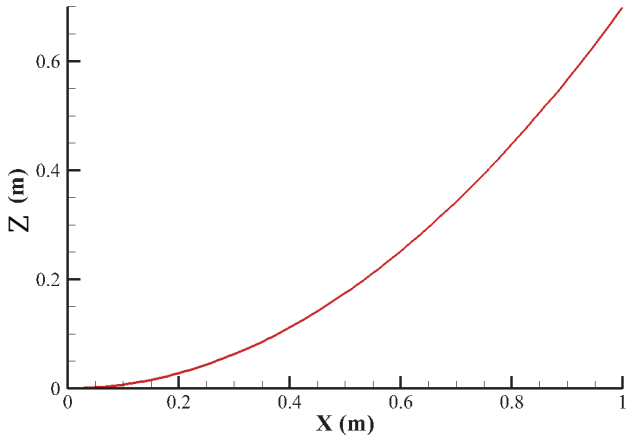

Figure 4.2 Representation of parabolic trajectory as x increases.

The trajectories of under three different field strengths are plotted in Figure 4.3. The parameters of these scenarios along with corresponding scenarios from section 4.2.1 are recorded in Table 4.1

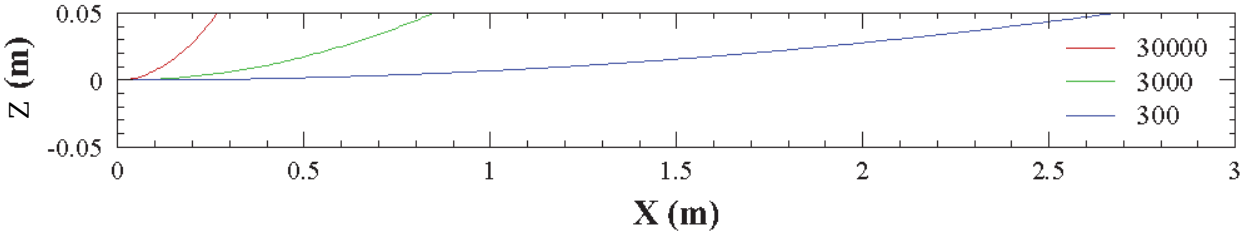

Figure 4.3 Schematic representation of ion trajectory due to electric field only (expanded *y* axis for better resolution).

Table 4.1 Parametric study of scenarios 4.2.1 and 4.2.2; electric field only in a vacuum.

Initial Velocity (V_0)	Field Strength (E_z)	Re-attachment Length (L_R)	Re-attachment time (t_R)	Electric Field Force (F_z)
0 m/s	240 V/m	0 m	6.24E-06 sec	3.85E-17 N
0 m/s	1,000 V/m	0 m	3.06E-06 sec	1.60E-16 N
0 m/s	10,000 V/m	0 m	9.66E-07 sec	1.60E-15 N
3E+05 m/s	240 V/m	1.871 m	6.24E-06 sec	3.85E-17 N
3E+05 m/s	1,000 V/m	0.916 m	3.06E-06 sec	1.60E-16 N
3E+05 m/s	10,000 V/m	0.289 m	9.66E-07 sec	1.60E-15 N

4.3 Magnetic Field Only (Vacuum)

4.3.1 No Initial Velocity (Vacuum)

A charged stationary ion within a vacuum subject to a uniform magnetic field B_y will experience no net force from the field and therefore remain stationary. This is evident as the governing Eq. (4.1) is proportional to the velocity perpendicular to the field.

4.3.2 Initial Velocity Normal to the Field (Vacuum)

When an initial velocity perpendicular to the magnetic field is applied to the ion, the field generates a force on the ion with a magnitude

$$\boldsymbol{F} = q\left(\boldsymbol{V}_0 \times \boldsymbol{B}\right) \tag{4.11}$$

From the centripetal force equation

$$F_z = \frac{m{u_0}^2}{R} = qB_y u_0 \tag{4.12}$$

The radius, R, of the ion path is therefore

$$R = \frac{mu_0}{qB_y} \tag{4.13}$$

Applying the principles of circular geometry provides

$$x^2 + y^2 = R^2 \tag{4.14}$$

allowing the reattachment length to be solved using half of the channel width, W_0.

$$L_R = \sqrt{R^2 - \left(R - \frac{W_0}{2}\right)^2} \tag{4.15}$$

This is assuming the point of origin is (0, 0) and the ion starting point is R. The time to reattach is found by determining the angle, θ, from start to the channel wall

$$\theta = \cos^{-1}\left(1 - \frac{W_0}{2R}\right) \tag{4.16}$$

Solving for the time it takes to travel along that arc length.

$$t_R = \frac{R\theta}{u_0} \tag{4.17}$$

An example of the ion path shape is represented in Figure 4.4 where B_z is 0.1 T, m is 5.89e^{-26} kg, q is 1.602e^{-19} C, and an initial ion velocity, V_0, of 3e^5 m/s.

$$R = \frac{5.89\times10^{-26}\,kg}{1.602\times10^{-19}\,C} \times \frac{3\times10^5\,\frac{m}{s}}{0.1T} = 1.1 \text{ meters} \tag{4.18}$$

This centripetal force acts perpendicular to both the magnetic field lines and the instantaneous velocity of the ion. Converting the motion to Cartesian system quantifies this force, Q, in x and z, see Figure 4.4

$$F_x = m\frac{du}{dt} = qQ_x = -qB_y w(t) \tag{4.19}$$

$$F_z = m\frac{dw}{dt} = -qQ_z = qB_y u(t) \tag{4.20}$$

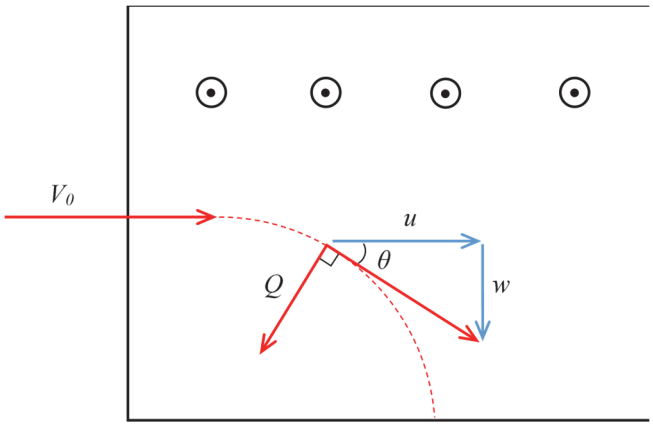

Figure 4.4 Schematic of ion trajectory due to magnetic field normal to the page.

The velocities u and w can be determined by taking the derivative of acceleration as expressed in Eqs. (4.19) and (4.20) with respect to time

$$\frac{d^2u}{dt^2} = -\frac{qB_y}{m}\frac{dw}{dt} = -\left(\frac{qB_y}{m}\right)^2 u(t) \tag{4.21}$$

$$\frac{d^2w}{dt^2} = \frac{qB_y}{m}\frac{du}{dt} = -\left(\frac{qB_y}{m}\right)^2 w(t) \tag{4.22}$$

Then solving the second order ODEs to get

$$u(t) = u_0 \cos\left(\frac{qB_y}{m}\right)t \tag{4.23}$$

$$w(t) = u_0 \sin\left(\frac{qB_y}{m}\right)t \tag{4.24}$$

The x and z position are found by integration

$$x = \int u dt = \int u_0 \cos\frac{qB_y}{m} t dt = u_0 \frac{m}{qB_y} \sin\frac{qB_y}{m} t + x_0 \tag{4.25}$$

$$z = \int w dt = \int u_0 \sin\frac{qB_y}{m} t dt = -u_0 \frac{m}{qB_y} \cos\frac{qB_y}{m} t + z_0 \tag{4.26}$$

Eq. (4.26) can be rearranged to solve for t_R by evaluating z_0 at (0, R) and given the channel width

$$t_R = \left(\frac{m}{qB_y}\right) \cos^{-1}\left(\frac{\frac{W_0}{2} - R}{-u_0 \frac{m}{qB_y}}\right) \tag{4.27}$$

Table 4.2 Parametric study of scenarios 4.3.2; magnetic field only in a vacuum.

Initial Velocity (V_0)	Field Strength (B_y)	Re-attachment Length (L_R)	Re-attachment time (t_R)	Force (F_z)
3E+05 m/s	0.1 T	0.167 m	5.58E-07 sec	4.81E-15 N
3E+05 m/s	0.2 T	0.119 m	3.95E-07 sec	9.61E-15 N
3E+05 m/s	0.5 T	0.075 m	2.51E-07 sec	2.40E-14 N

If the ion's velocity is at an angle, the trajectory will be in a helical shape, rather than simply circular. The helical pitch is determined by the incoming angle θ

$$p = \frac{2\pi m}{qB_y}\left(u_0 \cos\theta\right) \tag{4.28}$$

The initial angle affects the radius of curvature as well, this can be quantified by

$$R = \frac{m(u_0 \sin\theta)}{qB_y} \tag{4.29}$$

4.3.3 Force Comparison between Electric and Magnetic fields

Comparing the Lorentz force in the z direction from each scenario is useful in designing a channel. The force from the electric field is constant, while the force from the magnetic field is a function of u and v. As shown in Table 4.1 and Table 4.2 the overall force magnitude is similar to each other

at electric and magnetic field strengths of 10,000 V/m and 0.1 T respectively. However, the force acting in the x direction due to the magnetic field is very small because w is small.

4.4 Orthogonal Electric and Magnetic Fields (Vacuum)

4.4.1 No Initial Velocity (Vacuum)

For a stationary ion within mixed orthogonal electric and magnetic fields, the ion motion is influenced by both fields, represented schematically in Figure 4.5. Initially, the electric field exerts a force, F_E, to accelerate the ion, which then invites the Lorentz force from the magnetic field, $F_{B(E)}$. The magnetic field is also affected by the ion velocity in the x direction, $F_{B(v)}$.

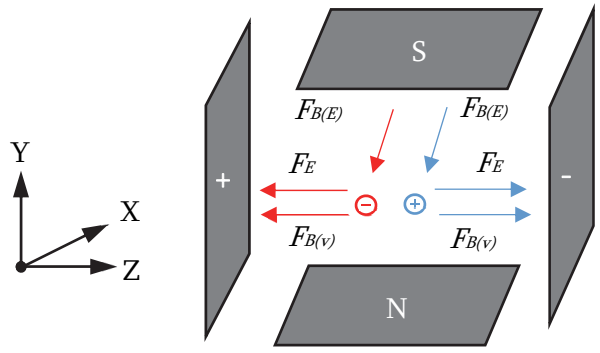

Figure 4.5 Schematic of forces acting on ions from orthogonal electric and magnetic fields.

Looking at the x components of the Lorentz force equation shows

$$a_x = \frac{q}{m}\left(i \cdot \left(\boldsymbol{V} \times \boldsymbol{B}\right)\right)$$

$$\frac{du}{dt} = \frac{q}{m}\left(i \times \begin{pmatrix} \hat{i} & \hat{j} & \hat{k} \\ u & 0 & w \\ 0 & B_y & 0 \end{pmatrix}\right)$$

$$\frac{du}{dt} = \frac{q}{m}\left(i \cdot \left(-wB_y i + uB_y k\right)\right)$$

$$\frac{du}{dt} = -\frac{qB_y}{m}w \tag{4.30}$$

And similarly for the y and z velocity components

$$\frac{dv}{dt} = 0 \tag{4.31}$$

$$\frac{dw}{dt} = \frac{qE_z}{m} + \frac{qB_y}{m}u \tag{4.32}$$

Solving Eq. (4.30) for the u velocity component requires differentiating again and substitution such that

$$\frac{d^2u}{dt^2} = -\frac{qB_y}{m}\left(\frac{qE_z}{m} + \frac{qB_y}{m}u\right)$$

$$\frac{d^2u}{dt^2} = -\frac{qB_y}{m}\left(\frac{qB_y}{m}\frac{E_z}{B_y} + \frac{qB_y}{m}u\right)$$

$$\frac{d^2u}{dt^2} + \left(\frac{qB_y}{m}\right)^2 u = -\left(\frac{qB_y}{m}\right)^2 \frac{E_z}{B_y} \tag{4.33}$$

The general solution of this second order ODE is

$$u(t) = A\cos\frac{qB_y}{m}t + B\sin\frac{qB_y}{m}t - \frac{E_z}{B_y} \tag{4.34}$$

The general solution of w is found similarly from Eq. (4.32)

$$\frac{d^2w}{dt^2} + \left(\frac{qB_y}{m}\right)^2 w = 0$$

$$w(t) = C\cos\frac{qB_y}{m}t + D\sin\frac{qB_y}{m}t \tag{4.35}$$

where the coefficients A, B, C, and D are found using the following initial conditions

$$u(0) = w(0) = 0 \tag{4.36}$$

$$u'(0) = -\frac{qB_y}{m}w(0) \tag{4.37}$$

$$w'(0) = \frac{qE_z}{m} + \frac{qB_y}{m}u(0) \tag{4.38}$$

so that

$$A = \frac{E_z}{B_y};\ B = 0;\ C = 0;\ D = \frac{E_z}{B_y}$$

This yields the following velocity components

$$u = \frac{E_z}{B_y}\cos\left(\frac{qB_y}{m}t\right) - \frac{E_z}{B_y} \tag{4.39}$$

$$v = v_0;\ y = vt + y_0 \tag{4.40}$$

$$w = \frac{E_z}{B_y}\sin\left(\frac{qB_y}{m}t\right) \tag{4.41}$$

Taking the integral of Eqs. (4.39) and (4.41) provides the x and z position at a given time t

$$\int u dt = \int \frac{E_z}{B_y}\cos\left(\frac{qB_y}{m}t\right) - \frac{E_z}{B_y} dt$$

$$\int w dt = \int \frac{E_z}{B_y}\sin\left(\frac{qB_y}{m}t\right) dt$$

$$x = \frac{E_z}{B_y}\frac{m}{qB_y}\sin\frac{qB_y}{m}t - \frac{E_z}{B_y}t + x_0 \tag{4.42}$$

$$z = -\frac{E_z}{B_y}\frac{m}{qB_y}\cos\frac{qB_y}{m}t + z_0 \tag{4.43}$$

The time to reattachment is determined by solving for t when $z = \frac{W_0}{2}$

$$t_R = \frac{m}{qB_y}\cos^{-1}\left(-\frac{\frac{W_0}{2}}{\frac{E_z}{B_y}\frac{m}{qB_y}}\right) \tag{4.44}$$

Which makes the reattachment length to be the value of x at time t_R. Because there is no motion in the x direction initially, once the electric field causes motion in the z direction, the magnetic field begins to pull in the negative x direction. While this result does not contribute to productive downstream separation, it does aid in understanding the physical interactions to be used in future models.

4.4.2 Initial Velocity Normal to the Field (Vacuum)

Providing an initial velocity on the ion in the x direction will follow the same analysis as the previous section, 4.4.1, with the exception of changing the initial conditions so $u_0 \neq 0$, see Figure 4.5 again.

The velocity components with an initial velocity present are similar to Eqs. (4.39), (4.40), and (4.41).

$$u = \left(u_0 + \frac{E_z}{B_y}\right)\cos\left(\frac{qB_y}{m}t\right) - \frac{E_z}{B_y} \tag{4.45}$$

$$v = v_0;\ y = vt + y_0 \tag{4.46}$$

$$w = \left(u_0 + \frac{E_z}{B_y}\right)\sin\left(\frac{qB_y}{m}t\right) \tag{4.47}$$

Integrating Eq. (4.45) with respect to time gives the x position downstream

$$x = \left(u_0 + \frac{E_z}{B_y}\right)\frac{m}{qB_y}\sin\frac{qB_y}{m}t - \frac{E_z}{B_y}t \tag{4.48}$$

and integrating Eq. (4.47) with respect to time gives the z position

$$z = -\left(u_0 + \frac{E_z}{B_y} \right) \frac{m}{qB_y} \cos \frac{qB_y}{m} t \tag{4.49}$$

The reattachment time is found using the same conditions for z as in Eq. (4.44).

$$t_R = \frac{m}{qB_y} \cos^{-1} \left(- \frac{\frac{W_0}{2}}{\left(u_0 + \frac{E_z}{B_y} \right) \frac{m}{qB_y}} \right) \tag{4.50}$$

The x position at t_R is the reattachment length. A comparison of the reattachment lengths, times, and net forces in the z direction are presented in Table 4.3. When there is no initial velocity under magnetic field strengths greater than 0.2 T, the ion trajectory radius is smaller than the width of the channel, resulting in an undefined reattachment length and time.

Table 4.3 Parametric study of scenarios 4.4.1 and 4.4.2; mixed orthogonal magnetic and electric fields in a vacuum.

Initial Velocity (V_0)	Field Strength (E_z)	Field Strength (B_y)	Re-attachment Length (L_R)	Re-attachment time (t_R)	Net Force (F_z)
0 m/s	1,000 V/m	0.1 T	-7.07E-02 m	7.07E-06 sec	1.05E-16 N
0 m/s	1,000 V/m	0.2 T	-4.29E-02 m	8.58E-06 sec	1.53E-16 N
0 m/s	1,000 V/m	0.5 T	-	-	-
3E+05 m/s	1,000 V/m	0.1 T	-5.81E-02 m	5.81E-06 sec	1.58E-16 N
3E+05 m/s	1,000 V/m	0.2 T	-1.46E-02 m	2.93E-06 sec	1.57E-16 N
3E+05 m/s	1,000 V/m	0.5 T	-2.39E-03 m	1.20E-06 sec	1.51E-16 N

4.5 Electric Field Only (Salt Water)

4.5.1 No Initial Velocity (Salt Water)

When considering the motion of an initially stationary charged ion within a salt solution subject to an electric field, the viscous forces must be considered. Applying Stokes' Law defines this opposing force, F_s as

$$\boldsymbol{F}_S = -6\pi\eta r_0 \boldsymbol{V} \tag{4.51}$$

where η is the fluid viscosity, V is the flow velocity past the object, and r_0 is the radius of the object. Since the ion motion is in the z direction, the velocity component is w and the sum of forces is equal to the following

$$m\frac{dw}{dt} = qE_z - 6\pi\eta r_0 w \tag{4.52}$$

Integrating Eq. (4.52) with respect to time for the instantaneous velocity using separation of variables we obtain

$$\int \frac{dw}{dt} = \int \frac{1}{m}\left(qE_z - 6\pi\eta r_0 w\right)$$

$$\int \left(\frac{m}{qE_z - 6\pi\eta r_0 w}\right) dw = \int dt$$

$$t + c = \frac{\ln\left(\frac{qE_z}{m} - \frac{6\pi\eta r_0}{m} w\right)}{-\frac{6\pi\eta r_0}{m}} \tag{4.53}$$

Using log rules w is expressed in the following terms

$$-\frac{6\pi\eta r_0}{m}\left(t + c\right) = \ln\left(\frac{qE_z}{m} - \frac{6\pi\eta r_0}{m} w\right)$$

$$\frac{qE_z}{m} - \frac{6\pi\eta r_0}{m} w = e^{-\frac{6\pi\eta r_0}{m}(t+c)}$$

$$w = \frac{\frac{qE_z}{m} - e^{\frac{-6\pi\eta r_0}{m}(t+c)}}{\frac{6\pi\eta r_0}{m}} \tag{4.54}$$

The initial conditions of $w_0 = 0$ allow the integrating constant c to be determined from Eq. (4.53)

$$c = \frac{\ln\left(\frac{qE_z}{m}\right)}{-\frac{6\pi\eta r_0}{m}} \tag{4.55}$$

Applying substitution, w at any instantaneous time t can now be expressed as

$$w(t) = \frac{\frac{qE_z}{m} - e^{\frac{-6\pi\eta r_0}{m}\left(t + \frac{\ln\left(\frac{qE_z}{m}\right)}{\frac{-6\pi\eta r_0}{m}}\right)}}{\frac{6\pi\eta r_0}{m}}$$

$$w(t) = \frac{\frac{qE_z}{m} - e^{\ln\left(\frac{qE_z}{m}\right) + \frac{-6\pi\eta r_0}{m}t}}{\frac{6\pi\eta r_0}{m}}$$

$$w(t) = \frac{\frac{qE_z}{m} - \frac{qE_z}{m}e^{\frac{-6\pi\eta r_0}{m}t}}{\frac{6\pi\eta r_0}{m}}$$

$$w(t) = \frac{qE_z}{6\pi\eta r_0}\left(1 - e^{\frac{-6\pi\eta r_0}{m}t}\right) \tag{4.56}$$

From Eq. (4.56) the z position can be found by integrating with respect to time

$$\int w(t)dt = \int \frac{qE_z}{6\pi\eta r_0}\left(1 - e^{\frac{-6\pi\eta r_0}{m}t}\right)dt$$

$$\int \frac{dz}{dt}dt = \frac{qE_z}{6\pi\eta r_0}\int 1 - e^{\frac{-6\pi\eta r_0}{m}t}dt$$

$$z = \frac{qE_z}{6\pi\eta r_0}t + \frac{mqE_z}{\left(6\pi\eta r_0\right)^2}e^{\frac{-6\pi\eta r_0}{m}t} + z_0 \tag{4.57}$$

We can simplify the Eq. (4.57) by recognizing that the term $e^{\frac{-6\pi\eta r_0}{m}t} \approx 0$ because $m \ll 6\pi\eta r_0$ which can be seen with a simple order of magnitude analysis of each term, with E=10000 V/m.

$$z = \frac{10^{-15}}{10^{-12}} t + \frac{10^{-41}}{\left(10^{-12}\right)^2} e^{-10^{14} t} + 0 \tag{4.58}$$

Plotting Eq. (4.57) also supports this as the function becomes linear within only a few seconds, indicating the velocity is constant and the z position is proportional to a ratio of the Lorentz and friction force.

$$z = \frac{qE_z}{6\pi\eta r_0} t + z_0 \tag{4.59}$$

Which yields the reattachment time equation

$$t_R = \frac{6\pi\eta r_0}{qE_z}\left(z - z_0\right) \tag{4.60}$$

The distance to re-attachment is determined by Eq. (4.8), where $u_0 = 0$, hence $L_R = 0$.

4.5.2 Flow Velocity Normal to the Field (Salt Water)

If the salt water in the channel has a fixed flow rate, the ion will carry the same velocity in the x direction, because the electric field only impacts the motion in the z direction. The velocity in the z direction is also influenced by viscous forces as it moves past water molecules, see Eq. (4.56).

The reattachment time for the ion is the same as the previous section as there are no additional forces in the z direction. The reattachment length is also determined by Eq. (4.8), with $u_0 \neq 0$. A comparison of the reattachment lengths and times are presented in Table 4.4.

Table 4.4 Parametric study of scenarios 4.5.1 and 4.5.2; electric field only in salt water.

Initial Velocity (V_0)	Field Strength (E_z)	Reattachment Length (L_R)	Reattachment time (t_R)
0 m/s	240 V/m	0 m	1.36E+03 sec
0 m/s	1,000 V/m	0 m	3.26E+02 sec
0 m/s	10,000 V/m	0 m	3.26E+01 sec
0.00978 m/s	240 V/m	13.28 m	1.36E+03 sec
0.00978 m/s	1,000 V/m	3.19 m	3.26E+02 sec
0.00978 m/s	10,000 V/m	0.32 m	3.26E+01 sec

4.6 Magnetic Field Only (Salt Water)

4.6.1 No Initial Velocity (Salt Water)

As stated in section 4.3.1, when an ion is stationary within a magnetic field, regardless of the medium, it will not experience a Lorentz force, resulting in no change in position.

4.6.2 Flow Velocity Normal to the Field (Salt Water)

When an ion is in motion subject to a magnetic field in salt water, Eq. (4.51) is still applied, only $\boldsymbol{V}$ now was two components, w and a relative u velocity.

$$m\frac{du}{dt} = -qB_y w - 6\pi\eta r_0\left(u - u_0\right) \tag{4.61}$$

$$m\frac{dw}{dt} = qB_y u - 6\pi\eta r_0 w \tag{4.62}$$

To simplify the equations, we will let $C_1 = qE_z$, $C_2 = qB_y$, and $C_3 = 6\pi\eta r_0$.

This is a coupled system of ODEs that can be solved through elimination and initial conditions. First solving Eq. (4.61) for w, we obtain

$$w = -\frac{m}{C_2}\frac{du}{dt} - \frac{C_3}{C_2}\left(u - u_0\right) \tag{4.63}$$

Substituting w into Eq. (4.62)

$$m\frac{d}{dt}\left(-\frac{m}{C_2}\frac{du}{dt} - \frac{C_3}{C_2}\left(u - u_0\right)\right) = C_2 u - C_3\left(-\frac{m}{C_2}\frac{du}{dt} - \frac{C_3}{C_2}\left(u - u_0\right)\right)$$

$$-\frac{m}{C_2}\frac{d^2u}{dt^2} - \frac{C_3}{C_2}\frac{du}{dt} + \frac{C_3}{C_2}u_0\frac{d}{dt} = \frac{C_2}{m}u - \frac{C_3}{m}\left(-\frac{m}{C_2}\frac{du}{dt} - \frac{C_3}{C_2}u + \frac{C_3}{C_2}u_0\right)$$

$$\frac{d^2u}{dt^2} + \frac{C_3}{m}\frac{du}{dt} = -\left(\frac{C_2}{m}\right)^2 u - \frac{C_3}{m}\frac{du}{dt} - \left(\frac{C_3}{m}\right)^2 u + \left(\frac{C_3}{m}\right)^2 u_0$$

$$\frac{d^2u}{dt^2} + 2\frac{C_3}{m}\frac{du}{dt} + \left[\left(\frac{C_2}{m}\right)^2 + \left(\frac{C_3}{m}\right)^2\right]u = \left(\frac{C_3}{m}\right)^2 u_0 \tag{4.64}$$

Using the quadratic solution formula to solve for the eigenvalues

$$\lambda_u = \frac{-2\frac{C_3}{m} \pm \sqrt{4\left(\frac{C_3}{m}\right)^2 - 4\left[\left(\frac{C_3}{m}\right)^2 + \left(\frac{C_2}{m}\right)^2\right]}}{2}$$

$$\lambda_u = -\frac{C_3}{m} \pm \sqrt{-\left(\frac{C_2}{m}\right)^2}$$

$$\lambda_u = -\frac{C_3}{m} \pm i\frac{C_2}{m} \tag{4.65}$$

Therefore the general solution for u is

$$u = e^{\frac{-C_3}{m}t}\left(A\cos\frac{C_2}{m}t + B\sin\frac{C_2}{m}t\right) + \frac{\left(\frac{C_3}{m}\right)^2}{\left(\frac{C_2}{m}\right)^2 + \left(\frac{C_3}{m}\right)^2}u_0 \tag{4.66}$$

Here we see the exponential term, $e^{\frac{-6\pi\eta r_0}{m}t}$ again and can assume it to be negligible which simplifies Eq. (4.66) considerably to the following

$$u = \frac{\left(C_3\right)^2}{\left(C_2\right)^2 + \left(C_3\right)^2}u_0 \tag{4.67}$$

The process is similar for the w velocity, first solving Eq. (4.62) for u

$$u = \frac{m}{C_2}\frac{dw}{dt} + \frac{C_3}{C_2}w \tag{4.68}$$

and substituting u within Eq. (4.61)

$$m\frac{d}{dt}\left(\frac{m}{C_2}\frac{dw}{dt}+\frac{C_3}{C_2}w\right)=-C_2w-C_3\left[\left(\frac{m}{C_2}\frac{dw}{dt}+\frac{C_3}{C_2}w\right)-u_0\right]$$

$$\frac{m}{C_2}\frac{d^2w}{dt^2}+\frac{C_3}{C_2}\frac{dw}{dt}=-\frac{C_2w}{m}-\frac{C_3}{m}\left(\frac{m}{C_2}\frac{dw}{dt}+\frac{C_3}{C_2}w-u_0\right)$$

$$\frac{d^2w}{dt^2}+\frac{C_3}{m}\frac{dw}{dt}=-\left(\frac{C_2}{m}\right)^2w-\frac{C_3}{m}\frac{dw}{dt}-\left(\frac{C_3}{m}\right)^2w+\frac{C_2}{m}\frac{C_3}{m}u_0$$

$$\frac{d^2w}{dt^2}+2\frac{C_3}{m}\frac{dw}{dt}+\left[\left(\frac{C_3}{m}\right)^2+\left(\frac{C_2}{m}\right)^2\right]w=\frac{C_2}{m}\frac{C_3}{m}u_0 \tag{4.69}$$

The eigenvalues of Eq. (4.69) are complex

$$\lambda_w=\frac{-2\frac{C_3}{m}\pm\sqrt{\left(2\frac{C_3}{m}\right)^2-4\left[\left(\frac{C_3}{m}\right)^2+\left(\frac{C_2}{m}\right)^2\right]}}{2}$$

$$\lambda_w=-\frac{C_3}{m}\pm i\frac{C_2}{m} \tag{4.70}$$

resulting in the following expression for w

$$w=e^{\frac{-C_3}{m}t}\left(A\cos\frac{C_2}{m}t+B\sin\frac{C_2}{m}t\right)+\frac{\frac{C_2}{m}\frac{C_3}{m}}{\left(\frac{C_3}{m}\right)^2+\left(\frac{C_2}{m}\right)^2}u_0 \tag{4.71}$$

Simplifying the exponential term, Eq. (4.71) now becomes

$$w=\frac{C_2C_3}{\left(C_3\right)^2+\left(C_2\right)^2}u_0 \tag{4.72}$$

Eq. (4.72) can be integrated to find the z position

$$\int w dt=\int\frac{C_2C_3}{\left(C_3\right)^2+\left(C_2\right)^2}u_0dt$$

$$z = \frac{C_2 C_3}{(C_3)^2 + (C_2)^2} u_0 t + z_0 \tag{4.73}$$

The reattachment time equation is then

$$t_R = \left(\frac{W_0}{2} - z_0 \right) \left(\frac{(C_2)^2 + (C_3)^2}{C_3 C_2 u_0} \right) \tag{4.74}$$

The reattachment length can be found by integrating Eq. (4.67) and substituting the reattachment time. A summary of the reattachment lengths and times are presented in Table 4.5.

$$\int u dt = \int \frac{(C_3)^2}{(C_2)^2 + (C_3)^2} u_0 dt$$

$$x = \frac{(C_3)^2}{(C_2)^2 + (C_3)^2} u_0 t \tag{4.75}$$

Table 4.5 Parametric study of scenarios 4.6.2; magnetic field only in salt water.

Initial Velocity (V_0)	Field Strength (B_y)	Reattachment Length (L_R)	Reattachment time (t_R)
0.00978 m/s	0.1 T	3.26E+06 m	3.33E+08 sec
0.00978 m/s	0.2 T	1.63E+06 m	1.67E+08 sec
0.00978 m/s	0.5 T	6.52E+05 m	6.66E+07 sec

The angle at which the ion travels can be modeled using Eq.(4.67) and Eq. (4.72), with Figure 4.4 as a reference so that

$$\tan\theta = \frac{w}{u} = \frac{C_2}{C_3} \tag{4.76}$$

For a sample magnetic field of 1 T, and viscosity of 0.001 poise, the resulting angle of deflection would be 2.97e-06 degrees. This would require a very long and straight channel to begin to see an effect in the deflection. Table 4.6 shows the relationship between reattachment lengths and deflection angles associated with larger magnetic fields.

Table 4.6 Required magnetic field strength values for the given angles of deflection.

Deflection Angle from B field	Field Strength (B)	Reattachment Length (L_R)
2.23E-06	1 T	3.26E+05 m
1.12E-05	5 T	6.52E+04 m
1.00E-04	45 T	7.24E+03 m

4.7 Orthogonal Electric and Magnetic Fields (Salt Water)

4.7.1 No Initial Velocity (Salt Water)

When both fields are present in a salt water solution and there is no initial velocity, $u_0 = 0$, the ion will act similar to section 4.4.1 with the addition of a viscous term.

$$m\frac{du}{dt} = -qB_y w - 6\pi\eta r_0\left(u - u_0\right) \tag{4.77}$$

$$m\frac{dw}{dt} = q\left[E_z + B_y u\right] - 6\pi\eta r_0 w \tag{4.78}$$

Solving Eq. (4.77) for w

$$w = -\frac{m}{C_2}\frac{du}{dt} - \frac{C_3}{C_2}\left(u - u_0\right) \tag{4.79}$$

Substituting w into Eq. (4.78)

$$m\frac{d}{dt}\left(-\frac{m}{C_2}\frac{du}{dt} - \frac{C_3}{C_2}\left(u - u_0\right)\right) = C_1 + C_2 u - C_3\left(-\frac{m}{C_2}\frac{du}{dt} - \frac{C_3}{C_2}\left(u - u_0\right)\right)$$

$$-\frac{m}{C_2}\frac{d^2u}{dt^2} - \frac{C_3}{C_2}\frac{du}{dt} + \frac{C_3}{C_2}u_0\frac{d}{dt} = \frac{C_1}{m} + \frac{C_2}{m}u - \frac{C_3}{m}\left(-\frac{m}{C_2}\frac{du}{dt} - \frac{C_3}{C_2}u + \frac{C_3}{C_2}u_0\right)$$

$$\frac{d^2u}{dt^2} + \frac{C_3}{m}\frac{du}{dt} = \frac{-C_2}{m}\frac{C_1}{m} - \left(\frac{C_2}{m}\right)^2 u - \frac{C_3}{m}\frac{du}{dt} - \left(\frac{C_3}{m}\right)^2 u + \left(\frac{C_3}{m}\right)^2 u_0$$

$$\frac{d^2u}{dt^2} + 2\frac{C_3}{m}\frac{du}{dt} + \left[\left(\frac{C_2}{m}\right)^2 + \left(\frac{C_3}{m}\right)^2\right]u = \frac{-C_2}{m}\frac{C_1}{m} + \left(\frac{C_3}{m}\right)^2 u_0 \tag{4.80}$$

Using the quadratic solution formula to solve for the eigenvalues of Eq. (4.80)

$$\lambda_u = \frac{-2\frac{C_3}{m} \pm \sqrt{4\left(\frac{C_3}{m}\right)^2 - 4\left[\left(\frac{C_3}{m}\right)^2 + \left(\frac{C_2}{m}\right)^2\right]}}{2}$$

$$\lambda_u = -\frac{C_3}{m} \pm \sqrt{-\left(\frac{C_2}{m}\right)^2}$$

$$\lambda_u = -\frac{C_3}{m} \pm i\frac{C_2}{m} \tag{4.81}$$

Therefore the general solution for u is

$$u = e^{\frac{-C_3}{m}t}\left(A\cos\frac{C_2}{m}t + B\sin\frac{C_2}{m}t\right) + \frac{-\frac{C_2}{m}\frac{C_1}{m}}{\left(\frac{C_2}{m}\right)^2 + \left(\frac{C_3}{m}\right)^2} + \frac{\left(\frac{C_3}{m}\right)^2}{\left(\frac{C_2}{m}\right)^2 + \left(\frac{C_3}{m}\right)^2}u_0 \tag{4.82}$$

Again the exponential term, $e^{\frac{-6\pi\eta r_0}{m}t}$ appears which simplifies Eq. (4.82) to the following

$$u = \frac{\left(C_3\right)^2 u_0 - C_2C_1}{\left(C_2\right)^2 + \left(C_3\right)^2} \tag{4.83}$$

By integrating Eq. (4.83), the x position can be determined

$$\int u dt = \int \frac{\left(C_3\right)^2 u_0 - C_2C_1}{\left(C_2\right)^2 + \left(C_3\right)^2} dt$$

$$x = \left(\frac{\left(C_3\right)^2 u_0 - C_2C_1}{\left(C_2\right)^2 + \left(C_3\right)^2}\right)t \tag{4.84}$$

The process is similar for w, solving for u within Eq. (4.78)

$$u = \frac{m}{C_2}\frac{dw}{dt} + \frac{C_3}{C_2}w - \frac{C_1}{C_2} \tag{4.85}$$

Substituting Eq. (4.85) into Eq. (4.77)

$$m\frac{d}{dt}\left(\frac{m}{C_2}\frac{dw}{dt}+\frac{C_3}{C_2}w-\frac{C_1}{C_2}\right)=-C_2w-C_3\left[\left(\frac{m}{C_2}\frac{dw}{dt}+\frac{C_3}{C_2}w-\frac{C_1}{C_2}\right)-u_0\right]$$

$$\frac{m}{C_2}\frac{d^2w}{dt^2}+\frac{C_3}{C_2}\frac{dw}{dt}=-\frac{C_2}{m}w-\frac{C_3}{m}\left(\frac{m}{C_2}\frac{dw}{dt}+\frac{C_3}{C_2}w-\frac{C_1}{C_2}-u_0\right)$$

$$\frac{d^2w}{dt^2}+\frac{C_3}{m}\frac{dw}{dt}=-\left(\frac{C_2}{m}\right)^2w-\frac{C_3}{m}\frac{dw}{dt}-\left(\frac{C_3}{m}\right)^2w+\frac{C_3}{m}\frac{C_1}{m}+\frac{C_2}{m}\frac{C_3}{m}u_0$$

$$\frac{d^2w}{dt^2}+2\frac{C_3}{m}\frac{dw}{dt}+\left[\left(\frac{C_3}{m}\right)^2+\left(\frac{C_2}{m}\right)^2\right]w=\frac{C_3}{m}\frac{C_1}{m}+\frac{C_2}{m}\frac{C_3}{m}u_0 \tag{4.86}$$

The eigenvalues are complex

$$\lambda_w=\frac{-2\frac{C_3}{m}\pm\sqrt{\left(2\frac{C_3}{m}\right)^2-4\left[\left(\frac{C_3}{m}\right)^2+\left(\frac{C_2}{m}\right)^2\right]}}{2}$$

$$\lambda_w=-\frac{C_3}{m}\pm i\frac{C_2}{m} \tag{4.87}$$

Therefore the general solution for w is

$$w=e^{\frac{-C_3}{m}t}\left(A\cos\frac{C_2}{m}t+B\sin\frac{C_2}{m}t\right)+\frac{\frac{C_3}{m}\frac{C_1}{m}}{\left(\frac{C_3}{m}\right)^2+\left(\frac{C_2}{m}\right)^2}+\frac{\frac{C_2}{m}\frac{C_3}{m}}{\left(\frac{C_3}{m}\right)^2+\left(\frac{C_2}{m}\right)^2}u_0 \tag{4.88}$$

Eliminating the exponential term, $e^{\frac{-6\pi\eta r_0}{m}t}$ and simplifying provides the following

$$w=\frac{C_3C_1+C_2C_3u_0}{\left(C_3\right)^2+\left(C_2\right)^2} \tag{4.89}$$

Integrating with respect to time gives the z position

$$\int w dt=\int\frac{C_3C_1+C_2C_3u_0}{\left(C_3\right)^2+\left(C_2\right)^2}dt$$

$$z = \left(\frac{C_3 C_1 + C_2 C_3 u_0}{\left(C_3\right)^2 + \left(C_2\right)^2} \right) t + z_0 \tag{4.90}$$

Therefore the reattachment time equation is

$$t_R = \left(\frac{W_0}{2} - z_0 \right) \left(\frac{\left(C_2\right)^2 + \left(C_3\right)^2}{C_3 C_1 + C_3 C_2 u_0} \right) \tag{4.91}$$

And substituting the result from Eq. (4.91) into Eq. (4.84) will give the reattachment length.

4.7.2 Flow Velocity Normal to the Field (Salt Water)

Using the derivations from the previous section, each component can be found when $u_0 \neq 0$. A summary of several scenarios varying the initial velocity and magnetic field strength while keeping the electric field strength constant, is presented in Table 4.7.

Table 4.7 Parametric study of scenarios 4.7.1 and 4.7.2; mixed orthogonal magnetic and electric fields in salt water.

Initial Velocity (V_0)	Field Strength (E_z)	Field Strength (B_y)	Re-attachment Length (L_R)	Re-attachment time (t_R)
0 m/s	1,000 V/m	0.1 T	-4.95E-11 m	-3.26E+02 sec
0 m/s	1,000 V/m	0.2 T	-9.90E-11 m	-3.26E+02 sec
0 m/s	1,000 V/m	0.5 T	-2.47E-10 m	-3.26E+02 sec
0.00978 m/s	1,000 V/m	0.1 T	-3.19E+00 m	-3.26E+02 sec
0.00978 m/s	1,000 V/m	0.2 T	-3.19E+00 m	-3.26E+02 sec
0.00978 m/s	1,000 V/m	0.5 T	-3.19E+00 m	-3.26E+02 sec

The comparison presented in Table 4.8 and Table 4.9 is based on the assumption that an ion entering a vacuum will have an initial velocity, but there is no mean flow velocity. Under the same fields within a salt water, the initial velocity exists as does a mean flow velocity.

When under an electric field only, the *u* velocity is equal to that of the initial or mean flow, and the *w* velocity is significantly higher (about 10^{10}) within the vacuum than in the salt water. When under a magnetic field alone in salt water, the *w* velocity components are significantly lower than the electric field under the same conditions (about 10^{-6}). With an initial velocity a vacuum under

combined fields, the w velocity is slightly higher than the electric field only. Mixed fields within salt water primarily reflects the velocities of an ion under an electric field only as well.

Table 4.8 Summary of projected ion velocities at the wall in a vacuum.

Environment	Fields	Initial/Mean Velocity (u_0)	u velocity (at t_R)	w velocity (at t_R)
Vacuum	E_z (1000 V/m)	0 m/s	-	2.6E+04 m/s
		3.0E+05 m/s	3.0E+05 m/s	2.6E+04 m/s
	B_y (0.5 T)	0 m/s	-	-
		3.0E+05 m/s	5.0E-02 m/s	5.6E-02 m/s
	E_z (1000 V/m) B_y (0.5 T)	0 m/s	-	-
		3.0E+05 m/s	-1.9E+04 m/s	3.2E+05 m/s

Table 4.9 Summary of projected ion velocities at the wall in salt water.

Environment	Fields	Initial/Mean Velocity (u_0)	u velocity (at t_R)	w velocity (at t_R)
Salt Water	E_z (1000 V/m)	0 m/s	-	3.9E-04 m/s
		9.8E-03 m/s	9.8E-03 m/s	3.9E-04 m/s
	B_y (0.5 T)	0 m/s	-	-
		9.8E-03 m/s	9.8E-03 m/s	1.9E-10 m/s
	E_z (1000 V/m) B_y (0.5 T)	0 m/s	-7.6E-13 m/s	3.9E-04 m/s
		9.8E-03 m/s	9.8E-03 m/s	3.9E-04 m/s

4.8 Conclusions

From the derivations of u and w velocities of a Cl ion just presented, it can be concluded that an electric field will have the greatest impact on ion motion within a salt water environment. In order for a magnetic field to provide sufficient force on ions in motion, the required magnitude would be far greater than economically and physically possible for the scale of this project. This is motivation to pursue Capacitive Deionization, which involves an electric field, as presented in CHAPTER 2.

CHAPTER 5 – CONCLUSIONS AND FUTURE WORK

5.1 Small Scale Desalination Testing

The present work provides a foundation upon which future desalination research involving GUITAR and other electrode materials can be conducted with confidence. The search for a CDI electrode material that is robust, economical, and highly competitive to RO is yet to be discovered, and therefore drives continued research on effective electrodes.

GUITAR does maintain attractive qualities as an electrode material such as high conductivity, corrosion resistance, the allowance of a wider potential window, and ability to coat a variety of substrates. However, the concluding limitation found in this study is that due to lack of micropores, its adsorption capacity is limited. Although Bare Felt is a porous substrate, when GUITAR, a non-porous material is coated on the surface, the accessible surface area is reduced.

Although the introduction of nanosprings theoretically increased the surface area of the GUITAR-coated graphite felt, a decrease in salt adsorption occurred. One reason is that effectively two coatings are present, one before the nanosprings' growth and one after. This compounds the effect of the GUITAR, making the direct deposition of GUITAR not advantageous in desalination.

Overall, the surface area of the electrodes involved in this study are significantly less than materials used in other studies, such as carbon aerogel or activated carbon. Increasing the Bare Felt electrode size appears to have little impact on the amount of salt adsorbed. Therefore one route to be taken would be to coat an extremely high surface area material with a very thin layer of GUITAR, so as to obtain favorable characteristics of low corrosion as well, but not to interfere with the micropores.

There are other methods of electrode creation with GUITAR that are not presented in this study due to lack of time. One of interest is to create particle electrodes with nano-sized GUITAR particles by ultrasonification and use a binder to adhere the slurry to a graphite current collector. This general method of electrode preparation is also utilized in studies by other research universities. From previous measurements by the Chemistry Department, particle electrodes have a specific surface area BET measurement near 20 m^2/g. This is still relatively low in comparison to

activated carbons or carbon aerogels, however, it is an improvement over the surface areas presented in the current study and could yield increased desalination.

5.2 Dynamic Flow Cell Design

With the incorporation of the flow cell design presented in 3.2, conductivity measurements can be made in real-time, eliminating error introduced by sample extraction and dilution. This also allows comparison of electrode performance over long periods of operation. Introducing a new system also presents new parameters to be optimized. Future studies can investigate how varying the solution flow rate impacts the capacity and charge time of the CDI cell, similar to [10, 36].

The setup can also be modified to represent a single pass mode by incorporating an upstream reservoir and diverting the effluent to waste. Such an arrangement more accurately represents industrial CDI operations, and presents opportunities to investigate impacting factors on energy consumption.

5.3 Theoretical Modeling

The mathematical model presented in this thesis discusses ion motion within the mean flow of a channel subjected to a combination of orthogonal electric and magnetic fields. The magnitude of force contributed by even a large magnetic field is significantly less than an electric field and is considered infeasible.

In regards to modeling the Electric Double Layer, since the graphite felt used in the experiments is porous, it is of interest to combine both scales of models, general ion motion in brackish water and a GCS model based on the non-overlapping double layer theory. If electrodes of significantly higher surface area from micropores are used, such as activated carbon, incorporating the modified Donnan model would be used to address the overlapping double layers.

These ion motion models within the mean flow and EDLs have potential to be simulated with Computational Fluid Dynamics, similar to [73] with the Vorsana Inc. Desalinator rotating disk design, and coupled with ANSYS Maxwell to model magnetic and electric fields. Using reliable methods of verification and validation established in the following studies [74, 75], a full prediction of CDI desalination can be realized and applied to various geometries and systems.

REFERENCES

[1] M. He, M. Russo, and M. Anderson, "Hydroclimatic characteristics of the 2012–2015 California drought from an operational perspective," *Climate,* vol. 5, 2017.

[2] *Guidelines for drinking-water quality*. Geneva: World Health Organization, 2011.

[3] *Water in crisis: a guide to the worlds fresh water resources*. New York, New York Oxford University Press Inc., 1993.

[4] M. Shatat and S. B. Riffat, "Water desalination technologies utilizing conventional and renewable energy sources," *International Journal of Low-Carbon Technologies,* vol. 9, pp. 1-19, 2012.

[5] M. A. Anderson, A. L. Cudero, and J. Palma, "Capacitive deionization as an electrochemical means of saving energy and delivering clean water. Comparison to present desalination practices: Will it compete?," *Electrochimica Acta,* vol. 55, pp. 3845-3856, 2010.

[6] T. J. Welgemoed and C. F. Schutte, "Capacitive deionization technology™: an alternative desalination solution," *Desalination,* vol. 183, pp. 327-340, 2005.

[7] S. Porada, R. Zhao, A. van der Wal, V. Presser, and P. M. Biesheuvel, "Review on the science and technology of water desalination by capacitive deionization," *Progress in Materials Science,* vol. 58, pp. 1388-1442, 2013.

[8] J. W. Blair and G. W. Murphy, "Electrochemical demineralization of water with porous electrodes of large surface area," in *Saline Water Conversion*. vol. 27, ed: American Chemical Society, 1960.

[9] A. M. Johnson and J. Newman, "Desalting by means of porous carbon electrodes," *Journal of The Electrochemical Society,* vol. 118, pp. 510-517, 1971.

[10] J.-B. Lee, K.-K. Park, H.-M. Eum, and C.-W. Lee, "Desalination of a thermal power plant wastewater by membrane capacitive deionization," *Desalination,* vol. 196, pp. 125-134, 2006.

[11] K. B. Hatzell, E. Iwama, A. Ferris, B. Daffos, K. Urita, T. Tzedakis*, et al.*, "Capacitive deionization concept based on suspension electrodes without ion exchange membranes," *Electrochemistry Communications,* vol. 43, pp. 18-21, 2014.

[12] Y. Gendel, A. K. E. Rommerskirchen, O. David, and M. Wessling, "Batch mode and continuous desalination of water using flowing carbon deionization (FCDI) technology," *Electrochemistry Communications,* vol. 46, pp. 152-156, 2014.

[13] Y. Oren, "Capacitive deionization (CDI) for desalination and water treatment — past, present and future (a review)," *Desalination,* vol. 228, pp. 10-29, 2008.

[14] S. Porada, L. Borchardt, M. Oschatz, M. Bryjak, J. S. Atchison, K. J. Keesman*, et al.*, "Direct prediction of the desalination performance of porous carbon electrodes for capacitive deionization," *Energy & Environmental Science,* vol. 6, p. 3700, 2013.

[15] Y. Liu, C. Nie, X. Liu, X. Xu, Z. Sun, and L. Pan, "Review on carbon-based composite materials for capacitive deionization," *RSC Advances,* vol. 5, pp. 15205-15225, 2015.

[16] A. G. El-Deen, R. M. Boom, H. Y. Kim, H. Duan, M. B. Chan-Park, and J. H. Choi, "Flexible 3D nanoporous graphene for desalination and bio-decontamination of brackish water via asymmetric capacitive deionization," *ACS Applied Materials & Interfaces,* vol. 8, pp. 25313-25325, 2016.

[17] S. Porada, L. Weinstein, R. Dash, A. van der Wal, M. Bryjak, Y. Gogotsi, *et al.*, "Water desalination using capacitive deionization with microporous carbon electrodes," *ACS Applied Materials & Interfaces,* vol. 4, pp. 1194-1199, 2012.

[18] C.-H. Hou and C.-Y. Huang, "A comparative study of electrosorption selectivity of ions by activated carbon electrodes in capacitive deionization," *Desalination,* vol. 314, pp. 124-129, 2013.

[19] R. W. Pekala, J. C. Farmer, C. T. Alviso, T. D. Tran, S. T. Mayer, J. M. Miller, *et al.*, "Carbon aerogels for electrochemical applications," *Journal of Non-Crystalline Solids,* vol. 225, pp. 74-80, 1998.

[20] R. Saliger, U. Fischer, C. Herta, and J. Fricke, "High surface area carbon aerogels for supercapacitors," *Journal of Non-Crystalline Solids,* vol. 225, pp. 81-85, 1998.

[21] Z.-H. Huang, Z. Yang, F. Kang, and M. Inagaki, "Carbon electrodes for capacitive deionization," *Journal of Materials Chemistry A,* vol. 5, pp. 470-496, 2017.

[22] J. Rouquerol, D. Avnir, C. W. Fairbridge, D. H. Everett, J. M. Haynes, N. Pernicone, *et al.*, "Recommendations for the characterization of porous solids (Technical Report)," in *Pure and Applied Chemistry* vol. 66, ed, 1994, p. 1739.

[23] H. Li, L. Zou, L. Pan, and Z. Sun, "Novel graphene-like electrodes for capacitive deionization," *Environmental Science & Technology,* vol. 44, pp. 8692-8697, 2010.

[24] R. Zhao, P. M. Biesheuvel, H. Miedema, H. Bruning, and A. van der Wal, "Charge efficiency: a functional tool to probe the double-layer structure inside of porous electrodes and application in the modeling of capacitive deionization," *The Journal of Physical Chemistry Letters,* vol. 1, pp. 205-210, 2010.

[25] P. Xu, J. E. Drewes, D. Heil, and G. Wang, "Treatment of brackish produced water using carbon aerogel-based capacitive deionization technology," *Water Research,* vol. 42, pp. 2605-2617, 2008.

[26] J. C. Farmer, D. V. Fix, G. V. Mack, R. W. Pekala, and J. F. Poco, "Capacitive deionization of NaCl and NaNO3 solutions with carbon aerogel electrodes," *Journal of The Electrochemical Society,* vol. 143, pp. 159-169, 1996.

[27] M. Wang, Z.-H. Huang, L. Wang, M.-X. Wang, F. Kang, and H. Hou, "Electrospun ultrafine carbon fiber webs for electrochemical capacitive desalination," *New Journal of Chemistry,* vol. 34, p. 1843, 2010.

[28] A. G. El-Deen, N. A. M. Barakat, K. A. Khalil, and H. Y. Kim, "Hollow carbon nanofibers as an effective electrode for brackish water desalination using the capacitive deionization process," *New Journal of Chemistry,* vol. 38, pp. 198-205, 2014.

[29] Y. Liu, J. Ma, T. Lu, and L. Pan, "Electrospun carbon nanofibers reinforced 3D porous carbon polyhedra network derived from metal-organic frameworks for capacitive deionization," *Scientific Reports,* vol. 6, p. 32784, 2016.

[30] C. Tsouris, R. Mayes, J. Kiggans, K. Sharma, S. Yiacoumi, D. DePaoli, *et al.*, "Mesoporous carbon for capacitive deionization of saline water," *Environmental Science & Technology,* vol. 45, pp. 10243-10249, 2011.

[31] H. Yin, S. Zhao, J. Wan, H. Tang, L. Chang, L. He, *et al.*, "Three-dimensional graphene/metal oxide nanoparticle hybrids for high-performance capacitive deionization of saline water," *Advanced Materials,* vol. 25, pp. 6270-6276, 2013.

[32] H. Li, T. Lu, L. Pan, Y. Zhang, and Z. Sun, "Electrosorption behavior of graphene in NaCl solutions," *Journal of Materials Chemistry,* vol. 19, pp. 6773-6779, 2009.

[33] B. Jia and L. Zou, "Wettability and its influence on graphene nansoheets as electrode material for capacitive deionization," *Chemical Physics Letters,* vol. 548, pp. 23-28, 2012.

[34] M. E. Suss, S. Porada, X. Sun, P. M. Biesheuvel, J. Yoon, and V. Presser, "Water desalination via capacitive deionization: what is it and what can we expect from it?," *Energy & Environmental Science,* vol. 8, pp. 2296-2319, 2015.

[35] W. M. Haynes, *CRC handbook of chemistry and physics*, 95 ed. Hoboken CRC press, 2014.

[36] R. Zhao, S. Porada, P. M. Biesheuvel, and A. van der Wal, "Energy consumption in membrane capacitive deionization for different water recoveries and flow rates, and comparison with reverse osmosis," *Desalination,* vol. 330, pp. 35-41, 2013.

[37] E. García-Quismondo, C. Santos, J. Lado, J. s. Palma, and M. A. Anderson, "Optimizing the energy efficiency of capacitive deionization reactors working under real-world conditions," *Environmental Science & Technology,* vol. 47, pp. 11866-11872, 2013.

[38] J. M. Silva, "Methods and systems for purifying aqueous liquids," ed: Google Patents, 2012.

[39] H. von Helmholtz, "Ueber einige gesetze der vertheilung elektrischer ströme in körperlichen leitern mit anwendung auf die thierisch-elektrischen versuche," *Annalen der Physik,* vol. 165, pp. 211-233, 1853.

[40] M. Gouy, "Sur la constitution de la charge électrique à la surface d'un électrolyte," *Journal of Theoretical & Applied Physics,* vol. 9, pp. 457-468, 1910.

[41] D. L. Chapman, "LI. A contribution to the theory of electrocapillarity," *Philosophical Magazine,* vol. 25, pp. 475-481, 1913.

[42] O. Stern, "Zur theorie der elektrolytischen doppelschicht," *Zeitschrifte fur Elektrochemie,* vol. 30, pp. 508-516, 1924.

[43] Y. A. C. Jande and W. S. Kim, "Modeling the capacitive deionization batch mode operation for desalination," *Journal of Industrial and Engineering Chemistry,* vol. 20, pp. 3356-3360, 2014.

[44] A. Hemmatifar, M. Stadermann, and J. G. Santiago, "Two-dimensional porous electrode model for capacitive deionization," *The Journal of Physical Chemistry C,* vol. 119, pp. 24681-24694, 2015.

[45] E. N. Guyes, A. N. Shocron, A. Simanovski, P. M. Biesheuvel, and M. E. Suss, "A one-dimensional model for water desalination by flow-through electrode capacitive deionization," *Desalination,* vol. 415, pp. 8-13, 2017.

[46] S. Porada, M. Bryjak, A. van der Wal, and P. M. Biesheuvel, "Effect of electrode thickness variation on operation of capacitive deionization," *Electrochimica Acta,* vol. 75, pp. 148-156, 2012.

[47] R. Zhao, M. van Soestbergen, H. H. M. Rijnaarts, A. van der Wal, M. Z. Bazant, and P. M. Biesheuvel, "Time-dependent ion selectivity in capacitive charging of porous electrodes," *Journal of Colloid and Interface Science,* vol. 384, pp. 38-44, 2012.

[48] P. M. Biesheuvel, R. Zhao, S. Porada, and A. van der Wal, "Theory of membrane capacitive deionization including the effect of the electrode pore space," *Journal of Colloid and Interface Science,* vol. 360, pp. 239-48, 2011.

[49] P. M. Biesheuvel, S. Porada, M. Levi, and M. Z. Bazant, "Attractive forces in microporous carbon electrodes for capacitive deionization," *Journal of Solid State Electrochemistry,* vol. 18, pp. 1365-1376, 2014.

[50] H. A. Arafat, M. Franz, and N. G. Pinto, "Effect of salt on the mechanism of adsorption of aromatics on activated carbon," *Langmuir,* vol. 15, pp. 5997-6003, 1999.

[51] W. H. McCutchen, "Radial counterflow inductive desalination," ed: Google Patents, 2011.

[52] I. F. Cheng, Y. Xie, R. Allen Gonzales, P. R. Brejna, J. P. Sundararajan, B. A. Fouetio Kengne*, et al.*, "Synthesis of graphene paper from pyrolyzed asphalt," *Carbon,* vol. 49, pp. 2852-2861, 2011.

[53] I. F. Cheng, I. Gyan, and H. Zhu, "Synthesis and electrochemical properties of GUITAR: a breakthrough material for energy storage," presentation in *Idaho Academy of Science meeting*, Moscow, Idaho, 2014.

[54] I. O. Gyan, P. M. Wojcik, D. E. Aston, D. N. McIlroy, and I. F. Cheng, "A study of the electrochemical properties of a new graphitic material: GUITAR," *ChemElectroChem,* vol. 2, pp. 700-706, 2015.

[55] I. F. Cheng, Y. Xie, I. O. Gyan, and N. W. Nicholas, "Highest measured anodic stability in aqueous solutions: graphenic electrodes from the thermolyzed asphalt reaction," *RSC Advances,* vol. 3, pp. 2379-2384, 2013.

[56] I. F. Cheng, "Batteries: recent advances in carbon materials," *C-Journal of Carbon Research,* vol. 3, p. 1, 2017.

[57] I. O. Gyan and I. F. Cheng, "Electrochemical study of biologically relevant molecules at electrodes constructed from GUITAR, a new carbon allotrope," *Microchemical Journal,* vol. 122, pp. 39-44, 2015.

[58] D. Zhang, A. Alkhateeb, H. Han, H. Mahmood, D. N. McIlroy, and M. G. Norton, "Silicon carbide nanosprings," *Nano Letters,* vol. 3, pp. 983-987, 2003.

[59] P. M. Wojcik, P. V. Bakharev, G. Corti, and D. N. McIlroy, "Nucleation, evolution, and growth dynamics of amorphous silica nanosprings," *Materials Research Express,* vol. 4, p. 015004, 2017.

[60] M. G. Norton, D. N. McIlroy, G. Corti, and M. A. Miller, "Silica nanosprings–a novel nanostructured material for hydrogen storage," in *Clean Technology Conference*, Houston, 2009, pp. 3-7.

[61] V. Dobrokhotov, L. Oakes, D. Sowell, A. Larin, J. Hall, A. Kengne*, et al.*, "ZnO coated nanospring-based chemiresistors," *Journal of Applied Physics,* vol. 111, p. 044311, 2012.

[62] V. P. Bakharev and N. D. McIlroy, "Signal-to-noise enhancement of a nanospring redox-based sensor by lock-in amplification," *Sensors,* vol. 15, pp. 13110-13120, 2015.

[63] K. W. Hathcock, J. C. Brumfield, C. A. Goss, E. A. Irene, and R. W. Murray, "Incipient electrochemical oxidation of highly oriented pyrolytic graphite: correlation between surface blistering and electrolyte anion intercalation," *Analytical Chemistry,* vol. 67, pp. 2201-2206, 1995.

[64] Y. Xie, S. D. McAllister, S. A. Hyde, J. P. Sundararajan, B. A. FouetioKengne, D. N. McIlroy*, et al.*, "Sulfur as an important co-factor in the formation of multilayer graphene in the thermolyzed asphalt reaction," *Journal of Materials Chemistry,* vol. 22, pp. 5723-5729, 2012.

[65] H. Smith, H. Zhu, and I. F. Cheng, "Capacitance of GUITAR- a new allotrope of carbon," University of Idaho Chemistry Department, internal poster presentation, 2016.

[66] A. Hemmatifar, J. W. Palko, M. Stadermann, and J. G. Santiago, "Energy breakdown in capacitive deionization," *Water Research,* vol. 104, pp. 303-311, 2016.

[67] Y. Bouhadana, M. Ben-Tzion, A. Soffer, and D. Aurbach, "A control system for operating and investigating reactors: The demonstration of parasitic reactions in the water desalination by capacitive de-ionization," *Desalination,* vol. 268, pp. 253-261, 2011.

[68] "IEEE recommended practice for powering and grounding electronic equipment," vol. Std 1100-2005 (Revision of IEEE Std 1100-1999), ed: IEEE, 2006, pp. 1-703.

[69] T. D. Tran, J. C. Farmer, and L. Murguia, "Method and apparatus for capacitive deionization and electrochemical purification and regeneration of electrodes," ed: Google Patents, 2001.

[70] G. L. Richard, "Method and apparatus for separating ions from a fluid stream," ed: Google Patents, 2004.

[71] 莫剑雄, " 对'一种节能的海水淡化装置的设计思想'一文的商榷," *净水技术,* pp. 36-38, 1990.

[72] R. De Luca, "Ion motion in salt water flowing under a transverse magnetic field," *EPJ Web of Conferences,* vol. 33, p. 02011, 2012.

[73] T. Xing, "Direct numerical simulation of open Von Kármán swirling flow," *Journal of Hydrodynamics,* vol. 26, pp. 165-177, 2014.

[74] T. Xing and F. Stern, "Factors of safety for Richardson extrapolation," *Journal of Fluids Engineering,* vol. 132, p. 061403, 2010.

[75] T. Xing and F. Stern, "Closure to "Discussion of 'Factors of safety for Richardson extrapolation'"(2011, ASME J. Fluids Eng., 133, p. 115501)," *Journal of Fluids Engineering,* vol. 133, p. 115502, 2011.

APPENDIX – SENIOR DESIGN PROJECT

Introduction

As an introductory study of capacitive deionization, a team of senior-level engineering students assisted in constructing and testing a desalination device for Vorsana Inc. The sponsor desired a system capable of generating a salt reduction of 50% and flow rate of 0.1 gpm. Guided by research and the findings of CHAPTER 4, the team decided to construct a system utilizing Capacitive Deionization. The team observed a maximum salt reduction of 14% and confirmed the correlation of increased surface area to increased capacitance, see Table A.1 and Table A.2. This appendix presents the results achieved using a Capacitive Deionization setup using straight channels of various aspect ratios to achieve desalination.

Methods

The experimental setup consisted of a test CDI channel section, two upstream reservoir tanks for both deionized water and salt water solution (~0.6M NaCl). To minimize energy required by the system, flow for the system was gravity-driven with elevated reservoirs, see Figure A.1. Flow control of the given system was provided by two ball valves, one upstream and one downstream of the channel, see Figure A.2. The method of CDI testing was single pass, as the effluent was collected in a separate tank and not recycled. The flow within the system was regulated at < 0.1gpm at the outlet with a globe valve. The channel sections were constructed with 1" PVC square tubing and a 4"x1" High Aspect Ratio Channel (HARC) manufactured out of acrylic, see Figure A.3. Channel end caps were designed to minimize turbulence and 3D printed with PLA to minimize turbulence.

The channel electrodes were constructed of flexible graphite sheets (Equalseal, 1/32" thickness). A voltage potential of 1.2V via DC power supply was applied to the electrodes via wire soldered connection and alligator clips for the square and High Aspect Ratio channels respectively. Electric current data was recorded via current probe (Tektronix) and a Tektronix Digital Oscilloscope. Salt reduction was measured using a conductivity meter (Oakton Con450) for the initial reservoir and effluent samples collected for each test.

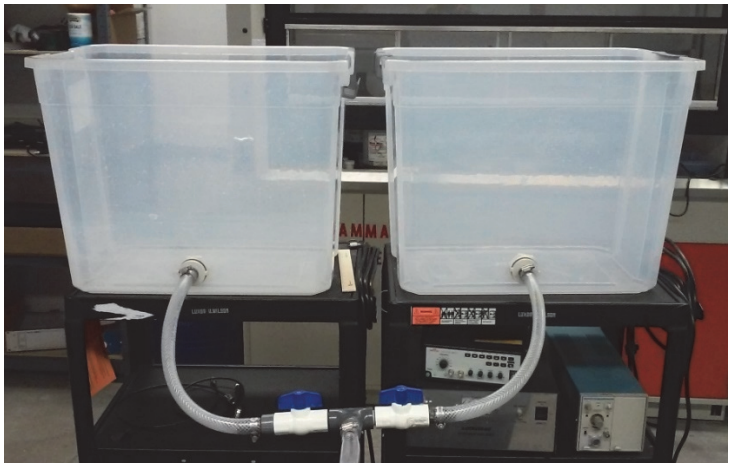

Figure A.1 Two tanks used for Desalintaion experiment: Left, 0.5M NaCl solution reservoir, and Right, Deionized Water reservoir for rinsing.

Figure A.2 Flow control valve setup and experimental channel. Ball valves used at outlet to control the flow rate.

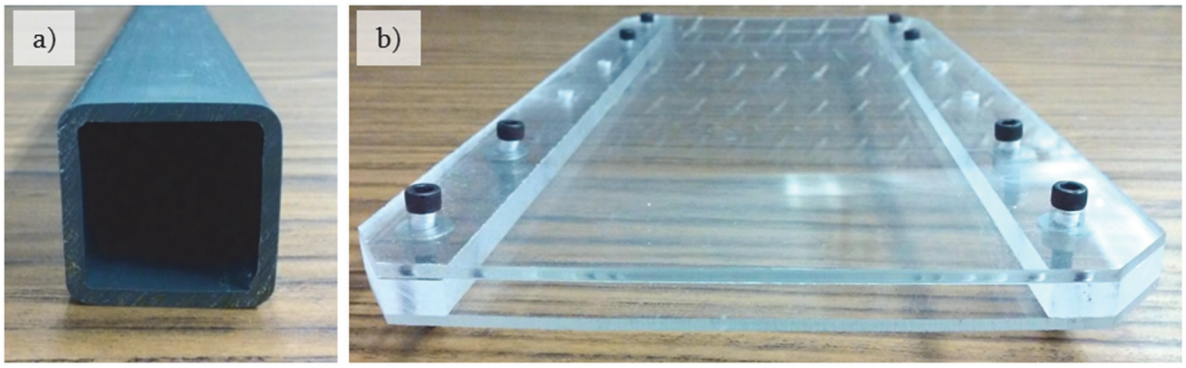

Figure A.3 Cross sections of capstone channel prototypes: a) 1"x1" PVC tubing used for the square channel and b) 1/4"x4" channel used for High Aspect Ratio Channel (HARC).

Channel Desalination Results

Table A.1 Effluent salt reduction from square channel, maximum of near 5% decrease.

Channel	Voltage (*V*)	Flow Rate (*gpm*)	Inlet Salinity (*g/L*)	% Salinity Change at Outlet		
				Sample 1	Sample 2	Sample 3
Square	1.2	< 0.1	21.02	-4.96	-4.17	0.49
			21.24	-2.65	-4.38	-4.00
			20.82	-0.86	-0.89	-1.15

Table A.2 Effluent salt reduction from High Aspect Ratio Channel (HARC), maximum of near 14% decrease.

Channel	Voltage (*V*)	Flow Rate (*gpm*)	Inlet Salinity (*g/L*)	% Salinity Change at Outlet		
				Sample 1	Sample 2	Sample 3
HARC (0.25”x4”)	1.2	< 0.1	21.02	-11.96	-5.31	-2.38
			12.50	-12.16	-4.48	-0.80
			13.28	-14.01	-7.91	-4.82

Conductivity Meter Flow Verification

To verify the accuracy of measurements with the conductivity meter, the conductivity probe housing was modified to permit flow through it for continuous measurement. A test scenario consisting of an initial reservoir concentration near 5 or 23 ppt was manually diluted with DI water over a period of two minutes. The conductivity probe was set to take automated readings every 3 seconds and samples were manually collected every 20 seconds to be measured after the test, represented in Figure A.4.

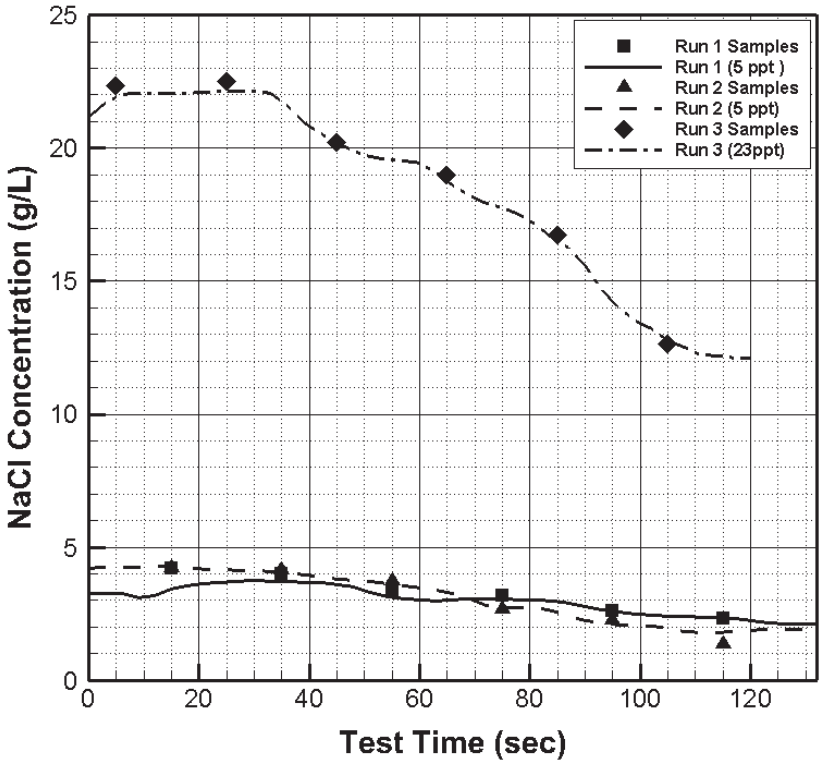

Figure A.4 Comparison plot of continuous conductivity readings and simultaneous sample extraction.

Conclusions

The overarching conclusion from this project was the confirmation of electrode surface area correlating with desalination performance, as well as a verification of the conductivity probe readings during continuous flow operation. The results from this study fueled the interest in using GUITAR and silica nanosprings to further enhance electrode surface area, which is presented in the main body of this thesis.